공학박사학위논문

음향방출 기반 구름 요소 베어링 진단을 위한 잡음 환경에서의 고장 정보 추출 연구

Investigation on Fault Information Extraction for Acoustic Emission based Rolling Element Bearing Diagnostics under Noisy Conditions

2022 년 8 월

서울대학교 대학원

기계항공공학부

김 수 지

음향방출 기반 구름 요소 베어링 진단을 위한 잡음 환경에서의 고장 정보 추출 연구

Investigation on Fault Information Extraction for Acoustic Emission based Rolling Element Bearing Diagnostics under Noisy Conditions

지도교수 윤 병 동

이 논문을 공학박사 학위논문으로 제출함

2022 년 4 월

서울대학교 대학원
기계항공공학부
김 수 지

김수지의 공학박사 학위논문을 인준함

2022 년 6 월

위 원 장 : 김 윤 영 (인)

부위원장 : 윤 병 동 (인)

위 원 : 안 성 훈 (인)

위 원 : 김 도 년 (인)

위 원 : 김 태 진 (인)

Abstract

Investigation on Fault Information Extraction for Acoustic Emission based Rolling Element Bearing Diagnostics under Noisy Conditions

Su Ji Kim
Department of Mechanical and Aerospace Engineering
The Graduate School
Seoul National University

In modern industry, the bearing is one of the most commonly used mechanical components for general rotor systems. It supports the applied loads on the rotary machine and makes the shaft system stable during rotation. The unexpected bearing failures can cause a halt down of whole rotor systems, making a huge economic loss. To prevent unexpected losses, much research has been conducted regarding condition monitoring of bearing systems using transducers, such as velocimeters and accelerometers. Recently, by means of the development of data processing technology, acoustic emission (AE) sensor has been actively employed for sensitive bearing diagnosis. The high sensitivity of AE sensors enables an early fault detection and defect monitoring of high stiffness systems, which is rather difficult for the vibrational approach. The raw measured AE signals include much information about the bearing's health states. However, it is hard to figure out the health index directly. Because the measured AE signals generally consist of multi-components, including noise. The bearing fault signal is almost buried under other components due to the weak energy. In addition, AE signal handling involves high sampling rate measuring, which can cause the applicability issue of traditional vibration-based signal processing techniques in a practical manner. For this reason, extracting target fault information in raw AE data practically needs several advanced signal processing techniques: it includes detecting the hidden fault signals and eliminating the unrelated components to bearing defects.

Therefore, this doctoral dissertation focuses on developing signal processing techniques for AE-based bearing diagnosis under noisy conditions. The dissertation investigates two thrusts: 1) research into a frequency band searching for bearing fault reasoning and 2) study of de-noising the irrelevant components to bearing defect.

The first research thrust suggests an effective band-selection method for AE sensor data under severe noise conditions. To increase the method's practicality in real applications, the proposed method defines a new indicator that is calculated from the time-domain features of the measured signal, without additional spectrum analysis. The suggested indicator employs the correlation coefficient and kurtosis of specially segmented signals to prevent disturbances from impulsive and non-Gaussian periodic noise components. The other research thrust proposes a de-noising technique for electrical components, especially electromagnetic interference (EMI), which easily corrupts AE measurements with highly non-stationarity. To this end, this study employs multi-sensor approach with an additional current sensor. In addition, an empirical mode decomposition (EMD) and probability-based dynamic filter are designed to adaptively sort out EMI components. A multi-sensor approach using EMD delivers algorithmic robustness even under the ever-changing nature of EMI, and a probabilistic approach enables effective filtering, while minimizing the risk of interrupting the bearing’s defect signal. Finally, the proposed dynamic filter effectively removes EMI components from the AE envelope spectrum for bearing diagnosis.

Keywords: Rolling element bearing (REB)
Fault diagnostics
Acoustic emission (AE)
Frequency band selection
Electrical noise elimination

Student Number: 2015-20718

Table of Contents

List of Tables

List of Figures

Nomenclature

AC	alternating current
ACF	auto-correlation function
AE	acoustic emission
BCF	bearing characteristic frequency
BPFI	ball pass frequency inner race
BPFO	ball pass frequency outer race
BSF	ball spin frequency
CDF	cumulative distribution function
DC	direct current
EMD	empirical mode decomposition
EMI	electromagnetic interference
FK	fast kurtogram
FTF	fundamental train frequency
HFRT	high-frequency resonance technique
IMF	intrinsic mode function
MAD	median absolute deviation
MED	minimum entropy deconvolution
PHM	prognostics and health management
PR	peak ratio
PWM	pulse width modulation
RCDF	reverse cumulative distribution function
REB	rolling element bearing
RPM	revolutions per minute
RPS	revolutions per second
SK	spectral kurtosis

SNR	signal to noise ratio
STFT	short-time Fourier transform
VFD	variable frequency drives
VFM	variable frequency motor
WPD	wavelet packet decomposition
D	number of defect impulses in each segment
D_b	defect signal from the bearing
E_{AE}	electromagnetic interference components in AE signal
E_C	electromagnetic interference components in current signal
F_k^{lv}	k-th decomposed spectrum in the lv level
$F_X(x)$	cumulative distribution function for random variable X
IMF_k	k-th intrinsic mode function of EMD process
K_A	autogram estimator
K_s	kurtosis for sampled data
K_X	spectral kurtosis estimator
L	lower boundary of target frequency band
M	defect measure
N	measured noise signal from sensor
O_r	operating signal related to the rotation of the shaft
P_p	number of pole pairs of the electric motor
PS	signal related to the main power supply
R_{AE}	system resonance measured from AE sensor
R_{xx}	correlation coefficient
$R(\cdot,\cdot)$	Pearson correlation coefficient
S	stride for moving window filter
U	upper boundary of target frequency band

X_{AE}	signal from an AE sensor
X_C	signal from an current sensor
X_w	complex envelope
X_k^{lv}	k-th decomposed signal in the lv level
f_e	electrical frequency of motor
f_m	mechanical frequency of motor
f_s	sampling frequency
lv	level of decomposition for frequency meshing
n_d	number of defect impulses
n_s	number of divided segment signals
n_{seg}	size of segment signal
p_j	j-th probability distribution function from the candidates
r_k	k-th residual signal of empirical mode decomposition process
w	weight for window function
Φ^{-1}	inverse Fourier transform
μ	sample mean
$\boldsymbol{\theta}_j$	parameters of probability distribution $p_j(\cdot)$

Chapter 1

Introduction

1.1 Motivation

Monitoring the health conditions of mechanical components is necessary for better availability and productivity in industrial field. To obtain the system's safety and prevent the failure, many engineers have researched fault diagnosis techniques for various kinds of machine elements [1]–[5]. Among the various mechanical components, the rolling element bearing (REB) is one of the most widely utilized mechanical components.

Rolling element bearings are essential components in many mechanical systems and components with various type, size, and speeds, as shown in Figure 1-1; thus, they have become a popular study target. Since the failure of a bearing affects the operation of a rotary system, it is important to diagnose and predict the state of a bearing in real-time. For this purpose, much research has been conducted regarding the estimation of bearing states, and many methods have been developed [6].

Traditionally, vibration analysis through an accelerometer is commonly performed because of its ease of use. Although the vibration signal contains many defect features, it has difficulty detecting a fault in its early stages or a high-stiffness system. Thus, recently, research using more sensitive sensors (e.g., AE sensors) has been explored. When AE sensors are used for diagnosis, applying existing vibration analysis methods becomes inadequate due to the features of the AE sensor. The huge sampling rate of AE sensors requires even more computing power, and a wideband operating frequency range rather becomes a burden to engineers for finding fault-related frequency bands. In addition, their high sensitivity makes the analysis vulnerable to noise, especially in the case of random impact and non-Gaussian periodic noise like electrical noise. The problem becomes even more challenging when impulsive defect energy from other cyclic components is measured simultaneously, or in a multi-defect condition with non-target bearings containing a different carrier frequency.

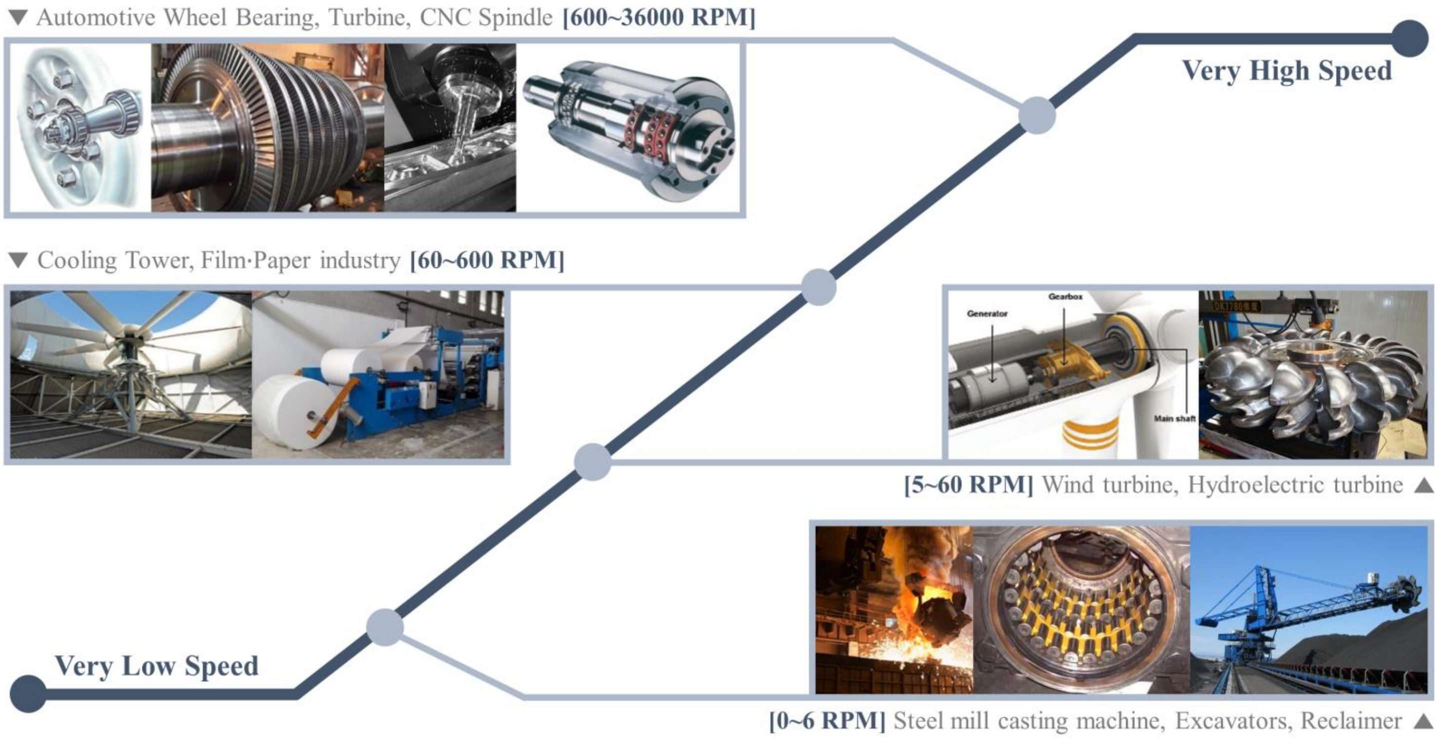

Figure 1-1 The usage of industrial rolling element bearings.

1.2 Research Scope and Overview

The ultimate goal of this doctoral dissertation is to extract fault information of rolling element bearing from AE signal that is measured under noisy conditions. To achieve this goal, two technical processes are needed: discovering the hidden fault-related information among the multi-components AE signals and removing the irrelevant components to target faults. To this end, this dissertation contains two research thrusts. First, a frequency band searching method for AE signals is developed. The other is de-noising techniques for electrical components. The specific research thrusts are as follows.

Research Thrust 1: Noise-robust frequency band selection for optimally extracting the fault-related information using segment-based efficient searching

Research thrust 1 proposes a noise-robust and efficient frequency band selection architecture for AE signals to searching the optimum frequency band. When diagnosing a rolling element bearing (REB), it is important to select the frequency band that has the most defect information. Many band-selection methods have been developed in recent years. Most existing methods target the vibration signal; hence, these methods are often unsuitable for use with acoustic emission (AE) sensors. With existing methods, the large sampling rate and high sensitivity of AE sensors causes huge computing costs and susceptibility to noise. To realize sensitive diagnosis with AE sensors, it is necessary to develop a proper band selection algorithm that operates under noisy conditions and with low computing cost. Thus, this paper proposes a correlation- and kurtosis- based band selection method for AE sensor data. The proposed method is validated by applying it to both simulated and experimental data. The test data contains random impulsive and non-Gaussian noises to represent the signal from other components and electrical noise from the motor system, respectively. With traditional methods, these noises either interrupt the proper band selection or increase the computing cost; however, the proposed method handles these noises and provides proper band selection with moderate computing efficiency.

Research Thrust 2: Multi-sensor based filter design using motor current signals for de-noising the electromagnetic interference

Research thrust 2 designs a multi-sensor based filter and develops a de-noising scheme for removing electrical components. The high sensitivity of AE sensors enables engineers to detect tiny fault signals of a bearing in advance of failure. However, this process is also easily corrupted by noise, due to the sensitivity of the sensors. Interference signals can mask the desired defect signal by dropping the signal-to-noise ratio. Among possible noise sources, electromagnetic interference (EMI) generated by variable frequency drives (VFD) is one of the most difficult noises to address because of its highly nonstationary characteristics. This disturbs the envelope spectrum, which is the conventional method of bearing diagnosis. Thus, in this research, a method is proposed to adaptively remove EMI from the AE signal for more accurate bearing diagnosis. The proposed method eliminates EMI peaks in the enveloped frequency spectrum, using a motor current signal. To this end, the proposed method employs empirical mode decomposition (EMD) and probabilistic filtering techniques to adaptively extract the EMI components from the current signals and filter out the EMI-related components in AE signals. The proposed method is verified by examining bearing testbed data and effectively eliminates the unwanted peaks of the EMI for AE signals.

1.3 Dissertation Layout

The rest of this doctoral dissertation is organized as follows. Chapter 2 provides technical background and literature review of rolling element bearing diagnosis using AE sensors. Chapter 3 describes the two kinds of experimental resources in this dissertation. Chapter 4 proposes a novel optimum frequency band selection method to figure out bearing-related frequency information from AE signals, and it is demonstrated by simulated and experimental validation. Chapter 5 develops a motor-current-based EMI filter for electrical noise elimination on envelope spectrum domain, and it is also verified using experimental validation. Finally, Chapter 6 summarizes the contributions and significance of this doctoral dissertation and suggests future research.

Chapter 2

Technical Background and Literature Review

2.1 Framework of PHM for mechanical systems

Monitoring the health states of mechanical components and predicting their failure is necessary for diminishing economic loss and securing human safety in industrial fields. For this purpose, many researchers have endeavored to develop prognostics and health management (PHM) for various systems, with the goal of optimal decision making [7]–[11].

Figure 2-1 shows the general procedure of PHM. It contains four steps for optimal decision-making. First, the sensing step gathers health information of target systems through various types of transducers. Gathered analog data is converted to digital form by the data acquisition modules and receiver. Synthetically designed software stores the measured digital information into analyzable data files. Second, the pre-processing step performs data manipulation to extract the hidden health information better. In this process, the raw signals are refined with de-noising and filtering to help further steps. Then the feature extraction step figures out the clues for hidden health information and estimate it in quantifying manner. Finally, the health reasoning step diagnoses the health conditions and prognoses the remaining useful life or quality degradation path. Among them, this dissertation mainly focuses on the front three steps: sensing, pre-processing, and feature extraction.

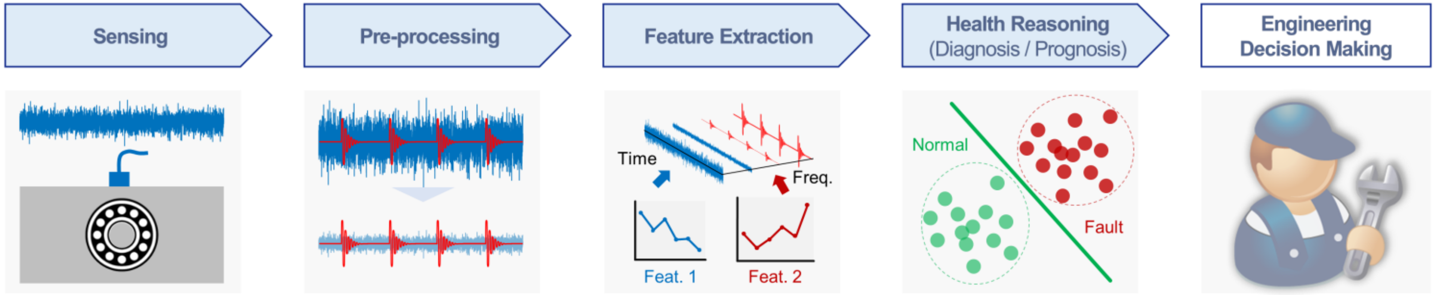

Figure 2-1 General procedure of PHM.

2.2 Acoustic Emission Techniques for Bearing System Monitoring

Since the failure of a bearing module can result in severe damage to a rotary system, it is desirable to accurately monitor and diagnose the health condition of REBs. To estimate the current status of a bearing, various transducers have been used, including distance, proximity, laser, optic, velocimeter, accelerometer, and ultrasonic sensor [12]. As the demand for precise diagnostic solutions has increased with the advances in sensing technology, acoustic emission (AE) sensors have emerged for bearing health diagnosis in many applications, such as turbines [13], [14], fan systems [15], slewing systems [16], railway axles [17] and dynamometer [18]. AE sensors have been used in both low- and high-speed conditions. Jamaludin and Mba focused on their studies on use in extremely slow machinery, less than 2 rpm [19]. Caesarendra et al. presented a review of AE-based condition monitoring in low-speed bearings [20]. Since low-speed bearings in heavy machines have a weak fault signal, a typical transducer cannot detect it. In other work, Saravanan et al. applied this type of sensor to spindle bearings to monitor the tool's condition to avoid the degradation of manufacturing quality and for early detection of a fault that may lead to a tool's failure [21]. Furthermore, Hasan et al. present a spectral imaging technique using AE data under variable speed conditions [22].

AE sensors have two advantages in bearing diagnosis: a high sampling rate and excellent sensitivity. When a bearing's component gets a microscopic defect on the surface of a material, high-frequency elastic waves are generated due to atomic cracking and the interaction between components. An elastic wave is propagated along the material, and the AE sensor catches the propagated energy through the resonance character of the element inside the sensor. This allows engineers to extract health features as the precursor to failure. To detect a transient abnormality of a bearing, many researchers have monitored typical time-domain features for AE signals, including: RMS, kurtosis, event, peak, count, rising time, and crest factor, etc. [12], [15], [23], [24]. However, these features have the purpose of being used for abnormality detection and trend analysis. Recently, a high-frequency resonance technique using envelope analysis has been generally adopted to diagnose a bearing’s fault mode, through the use of a raw AE signal [17], [25]–[29].

2.3 Overview of Rolling Element Bearing Systems Diagnosis

2.3.1 Fundamentals of Bearing Health Monitoring

A rolling element bearing consists of the rolling elements (e.g., ball, roller, pin), cage, lubricant, and the inner and outer raceways [30]. A bearing fault means any failure of any of these components. Various factors can cause a failure, such as surface asperity, brinelling, indentation from particles, lubricant film thickness, temperature condition, misalignment, electrical erosion, and improper mounting [31]. As bearing could be broken for a variety of reasons, it has various failure modes and mechanisms. Among the many failure modes, the primary bearing failure mode is material surface fatigue in the proper environment for operation and non-contaminated conditions [32]. The fatigue failure originated from subsurface cracks, and it is propagated according to continuous operation, as shown in Figure 2-2.

When there is a local defect in one of the bearing components, periodic impact signals are generated, due to the repeated collision between the defect and the neighboring components. The instantaneous local impact excites the overall frequency domain, such as modal test using an impact hammer. Then, diverse system characteristics appear in the frequency domain, including system and sensor resonance. To detect and diagnose the bearing defects, many researchers have relied on the frequency domain information generated by the cyclical impacts. To this end, engineers transform the time-domain signal into a frequency domain signal and go through feature analysis to extract meaningful information of frequency components related to target systems. Figure 2-3 illustrates this.

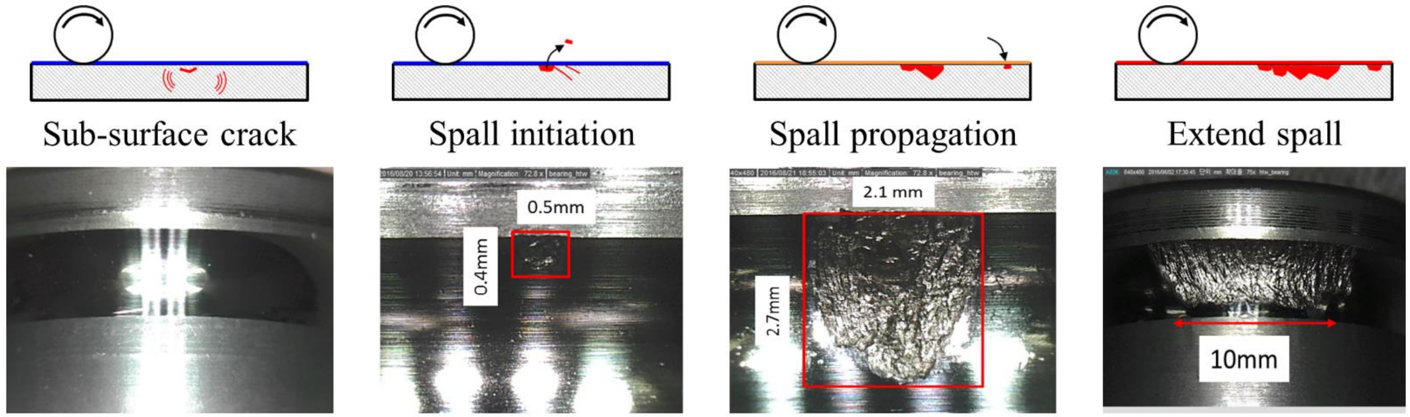

Figure 2-2 Health degradation process of REB by rolling contact fatigue failure.

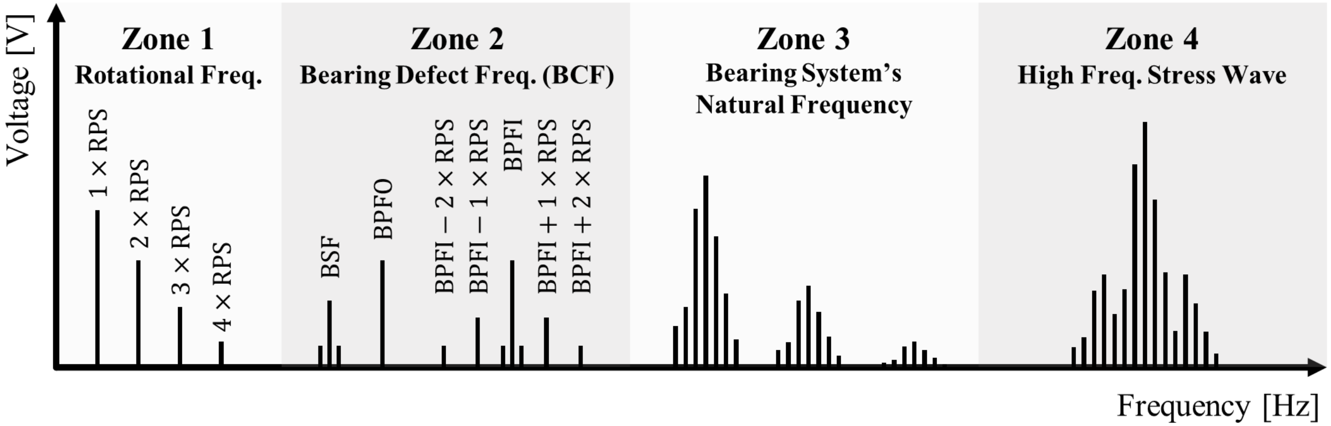

Figure 2-3 Frequency spectrum of a fault bearing signal.

In the figure, the spectrum of a fault signal is divided into four zones, each with different features. The main peaks in zone 1 indicate shaft frequency, revolutions per second (RPS), and harmonics. When there is misalignment or unbalance in the shaft system, these revolution-related peaks can increase. Problems with the driving transmission components, such as a coupling, also could be a source of these peaks. Additionally, direct current (DC) components lie at zero hertz. Although some features of the rotating system appear in this zone, the bearing's defect signal is hardly observed in zone 1.

In zone 2, the characteristic frequencies of a bearing are observed. Each bearing component has an individual frequency. Bearing characteristic frequencies (BCFs) are a direct key to bearing diagnosis. The BCF changes according to a defect's position. Thanks to bearing dynamics, BCF can be calculated when the driving condition and bearing geometry are specifically given [6], [33]. The ball pass frequency inner race (BPFI), ball pass frequency outer race (BPFO), ball spin frequency (BSF), and fundamental train frequency (FTF) are examples of such BCFs. When a defect is located on the rotating component of the bearing, the impulse train is modulated by the shaft rotation and load distribution [34]. This leads to sidebands around the BCF, as shown in Figure 2-3.

Zone 3 represents the resonance frequency of the bearing system. When the bearing's defect creates an internal impact, it excites the system resonance frequency. The frequency is an inherent characteristic of the system, the peaks in zone 3 depend on the system condition. A change in the defect condition may alter the appearance of the peaks. The status of the bearing is inferred by tracking the change of these peaks.

Finally, zone 4 contains information about the high-frequency stress wave generated by the interaction between bearing elements. This zone contains diverse information, such as the collision of elements, metal-to-metal contact noise, and frictional energy, which propagates along the metal in the system. Many engineers employ an AE sensor to capture this energy through the sensor resonance character.

Although clues to the bearing's status are presented all over the frequency domain, the actual implementation of bearing fault detection is not easy. Because the bearing is usually a part of a bigger system, the bearing signal is overlapped with and covered by the system's signal. For example, even though zone 2 contains definite peaks reflecting a defect in the bearing components, in practice, this frequency area is considered inadequate for fault detection due to the noise from the system. Unless the bearing failure is severe and its signal becomes dominant, it is common for BCFs in zone 2 to be buried by other low-frequency signals. Hence, one of the issues in applying bearing diagnosis in the real world is to separate the defect signal from the raw data.

2.3.2 Analysis of Sensor Signal for Rolling Element Bearing

Unlike zone 2, zones 3 and 4 are less affected by the low-frequency signal from the system. However, the defect signal is not as intuitive in zones 3 and 4 as it is in zone 2. While bearing diagnosis with zone 2 is directly possible by checking BCFs, zone 3 and zone 4 need additional analysis to extract the defect frequency. Figure 2-4 shows a conceptual defect signal with the resonance frequency. Each impulse generates a repeated phenomenon of resonance and attenuation during the defect period. This looks like the amplitude modulation of the resonance signal by the impulse period. The envelope technique, using an analytic signal with Hilbert transform, has been widely adopted for demodulation analysis. The resulting demodulated signal, called an envelope, is obtained from this analysis. This envelope signal is positioned in zone 2 of the spectrum, representing the BCF. That is, the processed signal contains the bearing defect information like the one originally located in zone 2, but without the system's low-frequency signal, because that comes from zone 3 and 4.

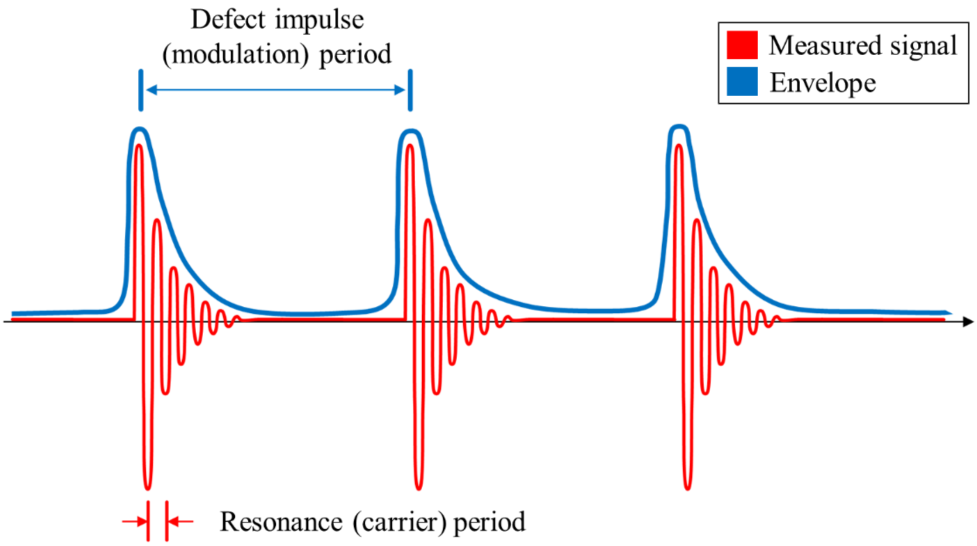

Figure 2-4 Demodulation process through envelope analysis.

However, if there is insufficient energy to resonate the system, due to low RPM or small defect size, the necessary information may not be captured in zone 3. Such low energy requires a highly sensitive sensor for detection. The AE sensor is one that can capture the weak resonance signal in zone 4. However, because of its high sensitivity, an AE sensor also measures the other ambient noises in the high-frequency region; this disturbs the fault diagnosis. Thus, a suitable method to remove the noise is required.

The high-frequency resonance technique (HFRT) is one representative methodology for bearing diagnosis using aforementioned high frequency information. This method is popular for extracting mechanical defect features from a raw signal [35]. The technique catches the resonance frequency generated by impulses of a bearing defect. Then, it converts high-frequency fault information to the bearing characteristic defect frequency through envelope analysis. The Key process of HFRT is frequency filtering and fault feature extraction from envelope spectrum. The frequency filtering excludes the components irrelevant to bearing defects, which is related to thrust 1 of this dissertation. Moreover, fault feature extraction under noise conditions is also an important procedure for diagnosis, which is related to thrust 2 of this dissertation. The detail of the literature review is covered in following Sections 2.4 and 2.5.

Figure 2-5 represents the conceptual procedure of high frequency resonance techniques (HFRT), which is traditional methodology for bearing fault diagnosis. It employs the four technical steps of signal processing. First, raw signal is measured from sensor on system housing, and the frequency filter is adopted for de-noising and defect information extraction. Then the envelope analysis capture the signal's overall envelope path to capture the modulation of high-frequency resonation from defect. Finally, spectrum analysis on envelope signal visualize the specific defect information on frequency domain.

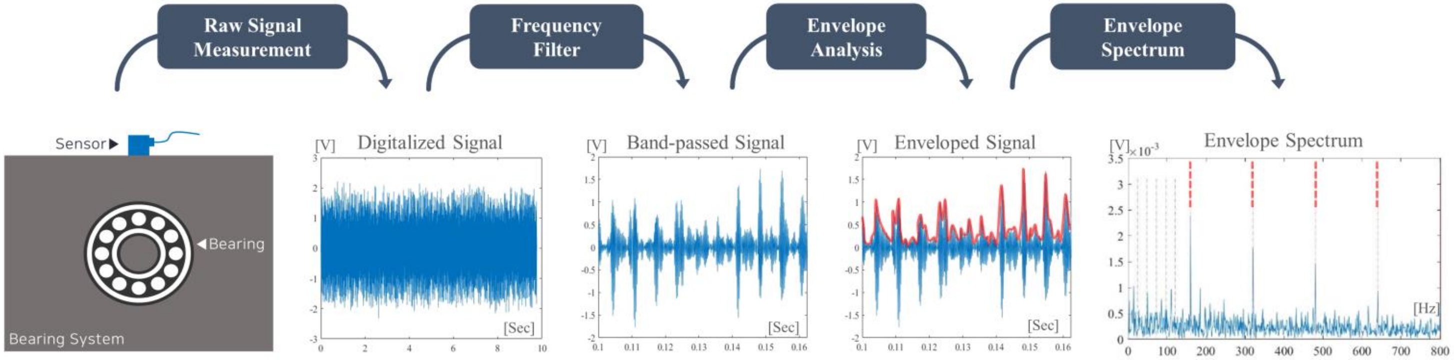

Figure 2-5 Conceptual procedure of high-frequency resonance technique (HFRT).

2.4 Optimum Frequency Band Selection

For successful information extraction of bearing defect-related signals, the optimal frequency band of the resonance signal that carries the most defect information must be found. Two approaches have been proposed for selecting the optimal frequency band. The first approach is to use optimization-based techniques, such as particle swarm optimization (PSO), genetic algorithm (GA), and harmonic search (HS) [36]. In the optimization approach, two parameters defining the frequency band filter (i.e., bandwidth and frequency center) are optimized, while the objective function is set to be the measure of the bearing defect features. Although these methods can define the optimal band, they require high computing cost.

To reduce the computing cost, an alternative approach called sub-optimal band selection, which allows fast searching with low computing cost, has emerged. Researchers utilize the characteristics of the bearing fault for efficient band searching and selection. Impulsiveness and periodicity in the bearing fault signal are two major characteristics used for band selection [37]. Dyer and Stewart reveal that the impulsive signal that arises from a bearing defect distorts the Gaussian distribution of the normal bearing signal at a particular frequency band [38]. Therefore, by observing the degree of distortion, the frequency band that contains the fault information can be selected. These researchers also suggested the use of the kurtosis as a measure for the distortion of the distribution. Their observation inspired the following researchers to develop various objective metrics based on the kurtosis. Dwyer suggested frequency domain kurtosis (FDK) to consider localized transient or hidden non-stationary components [39]. Pagna and Ottonello developed modified FDK through short-time Fourier transform (STFT) [40]. Antoni et al. proposed spectral kurtosis (SK) using Wold-Cramer decomposition [41]; further research was conducted to define the Kurtogram [42] and Fast Kurtogram (FK) [43]. FK has become a popular method to interpret a frequency domain, due to its fast computing. Barszcz and JabŁoński developed Protrugram using iterative narrow band-passing and kurtosis of the envelope spectrum to effectively search the central frequency of the defect band [44].

Other researchers have focused on the periodic characteristics for band selection. Borghesani et al. and Smith et al. proposed spectrum features for cyclic defect monitoring, which they called the ratio of cyclic contents (RCC) and the indicator of 2nd order cyclostationarity (ICS2) [45], [46]. They found specific frequency components related to the bearing's defect and quantified the amount of fault information through demodulation and spectrum analysis. Smith et al. suggested a log-cycligram that upgrades the pre-proposed features using the log-envelope spectrum [37]. Mauricio proposed a noise-robust algorithm, improved from RCC by employing spectral coherence. Antoni and Borghesani suggested a distcsgram using a statistical test for condition indicators to consider non-Gaussianity and cyclostationarity [47].

Although considering impulsive and periodic characteristics has many advantages, it still has limitations. Kurtosis-based methods are simple and effective in finding hidden impulsive features; however, they are vulnerable to external impulsive noise. Spectrum-based methods guarantee better detection of a fault signal by using the known defect frequency, but additional signal processing related to the demodulation, spectral analysis, and objective function design is needed. To avoid these limitations, band-selection methods have been developed to consider both impulsive and periodic characteristics without spectral analysis. Zhang et al. presented correlated kurtosis to quantify the periodic impulsiveness of time-series data [48]. McDonald and Zhao proposed multipoint kurtosis-based deconvolution methods for optimally extracting defect symptoms [49]. Antoni proposed Infogram, which uses time and spectral domain indicators that represent impulsiveness and periodicity, respectively [50]. Moshrefzadeh presented Autogram, which uses wavelet decomposition and autocorrelation to handle the vulnerability of Infogram to noise [51].

The aforementioned methods have been mostly developed for vibration analysis. Although the vibration signal contains many defect features, it has difficulty detecting a fault with low energy, or a fault in a high-stiffness system. For example, a bearing fault in a low-speed rotating machine or a bearing fault in its early stage that is releasing a low energy signal is difficult to detect with vibration sensors and related analysis. Thus, recently, research using acoustic emission (AE) sensors has been explored for sensitive bearing diagnosis. AE techniques were originally proposed for nondestructive testing decades ago [52]. The ability of AEs to measure with high-frequency and great sensitivity is useful in many applications [53], especially for low-speed and high-stiffness bearing systems [16], [20], [54]. In the beginning, transient AE features such as count, event, peak, and amplitude were utilized for precise and early fault detection of a bearing [12], [24]. During the last two decades, waveform-based raw AE data analysis has been spotlighted [23], [28]. In the waveform-based approach, continuously measured raw signals enable engineers to interpret AE signals using traditional signal processing features based on rotary dynamics. However, because AE's broadband information requires significant computational resources, frequency band selection is necessary for efficient application of the AE techniques.

There has been much research about frequency band selection of AE signals for bearing fault diagnosis. Eftekharnejad applied the spectral kurtosis approach to optimize the frequency band of AE data [27]. Nguyen et al. implemented empirical mode decomposition and discrete wavelet packet transform for frequency reasoning [28]. Spectral kernel-based optimum band searching research has also been conducted in other recent work [55], [56]. These researchers developed a sub-band selection measure using a Gaussian distribution and a mixture model. However, AE's high sensitivity makes this analysis approach vulnerable to noise, especially in the case of random impact and non-Gaussian periodic noise, such as electrical noise [37], [57], [58]. In addition, existing noise-robust vibration methods cannot be directly applied as is; instead, they need modification to deal with the characteristics of AE data, specifically, data heaviness and wide frequency information. The huge sampling rate of AE sensors requires even more computing power for the de-noising process in practice, and the wide frequency range needs detailed examination in terms of frequency decomposition. For example, a high-cost algorithm, such as spectral coherence or Autogram, consumes a huge amount of time for an AE signal input, and wavelet-based decomposition methods can generate computational burden due to the dense frequency filtering. The computation burden for AE data is a concern in practice [59], and noise (e.g., EMI noise) – a problem even for a vibration signal – is considered even more critical for an AE signal [60], [61]. In addition, the problem becomes even more challenging when both impulsive and non-Gaussian periodic noise must be addressed simultaneously.

2.5 De-noise the Undesirable Components in Sensor Signal

While the high sensitivity of an AE sensor brings diagnostic advantages, it is subject to being affected by undesirable noise signals. When an AE sensor is used, the signal-to-noise ratio could easily get worse, depending on the data acquisition conditions. Among the various noise sources, electrical noise is one of the main problems that contaminate bearing data [62]. Electrical noise comes from the power supply and electric devices, such as the motor, servo-drive, signal converter, digitizer, etc. Electrical noise cannot be perfectly removed because it stems from the data acquisition or system operating module. Electromagnetic interference (EMI) is considered by many to be the most irritating electrical noise for condition monitoring. Skibinski et al. revealed the EMI generated from modern PWM AC drives and noted that it affects susceptible equipment like high-frequency sensors and measuring systems [63]. Sikorska and Mba presented that EMI is a challenge when using AE data for condition monitoring [60]. Smith et al. described the detailed effect of EMI on the bearing signal gathered from an accelerometer [64]. Sun explored an analytic study of a PWM, which is the source of EMI, and presented some frequency characteristics [65]. EMI creates high-frequency noise with harmonics up to the megahertz. Also, the noise is ever-changing, depending on the operating system and conditions. These broadband nonstationary factors critically affect bearing data gathered by AE sensors, which observe a wide bandwidth for fault detection. This issue not only degrades the signal-to-noise ratio but also can mislead efforts of defect identification.

Several research studies have attempted to remove this disturbance; however, most of them considered vibration data. Antony and Randall proposed unsupervised noise cancellation methods: self-adaptive noise cancellation (SANC) and discrete/random separation (DRS) [66], [67]. Both algorithms sift the interference using a filter designed by the given signal and a time-delayed signal of itself. Randall and Sawalhi designed a cepstral editing procedure to remove discrete components in the frequency domain [68]. Through their cepstrum approach, they successfully eliminated harmonic components in the frequency domain. Smith et al. proposed an optimized spectral kurtosis method to diminish the effect of EMI [64]. They optimized the filter by iteratively shifting the band parameter and considering each kurtosis value. Mauricio et al. proposed an automated filter selection method based on cyclic spectral coherence information [61]. Their method showed better performance in detecting bearing faults, as compared to existing methods. All of these previous studies focus on increasing the bearing's defect symptoms through proper filter design. However, those methods work successfully only when the bearing defect frequency and operating system information are known. Also, these presented methods demand high computing costs for use with AE data, considering the large sampling rate. Moreover, the AE data is more vulnerable to EMI, as compared to vibration data, due to the observing bandwidth.

Despite the weaknesses of using AE data, there has not been much research to date to deal with the EMI gathered by AE sensors for bearing diagnosis. Acuña and Vicuña developed a frequency filter for EMI on AE data as a way of preprocessing for bearing defect size estimation [57]. They constructed a filter based on the cyclostationary peak ratio distribution (CPRD) and compared it to traditional filters. However, this method also has a limitation in that it operates under insufficient information.

Chapter 3

Description of Experimental Resources

This section describes the experimental resources used to demonstrate the proposed methodologies in this dissertation. Two kinds of test rigs are constructed for different types of bearing: angular ball bearing and slewing bearing. The angular ball bearing test rig targets small-sized ball bearing with axial and thrust loads, which is used for low to high-speed operating conditions with approximately 10 to 3000 RPM of shaft rotation. The slewing bearing test rig is designed to experiment with low-speed bearing with heavy axial load, which targets very low to low-speed conditions, approximately 0.01 to 30 RPM. The detailed experimental setup and description are presented in the following sections. Section 3.1 describes the configuration of the angular ball bearing testbed, and Section 3.2 presents about slewing bearing testbed.

3.1 Configuration of Angular Ball Bearing Testbed

The angular ball bearing test-rig is shown in Figure 3-1(a). The main shaft is supported by three angular ball bearings. At one end, two angular bearings are assembled, and the other end is supported by the test bearing. The load is applied to the test bearing using two pneumatic cylinders in the axial and radial directions. The load cell measures the load in real-time. For realistic load on the bearing, the dynamic equivalent radial load is calculated through ISO 281. The servo motor delivers driving force to the main shaft, and the servo drive controls the rotational speed, gathering the encoder signal. A coupling transfers the driving force to the main shaft. The AE sensor is attached for data acquisition. A wideband resonance type AE sensor, WSa from Mistras Inc., is placed on the closest housing to the test bearing, as shown in Figure 3-1(b). A preamplifier, model 3/6/9c from Mistras Inc., amplifies the obtained data by 40dB. A digitizer model 9775 from National Instruments then converts the amplified analogue signal to digital data with 14-bit resolution.

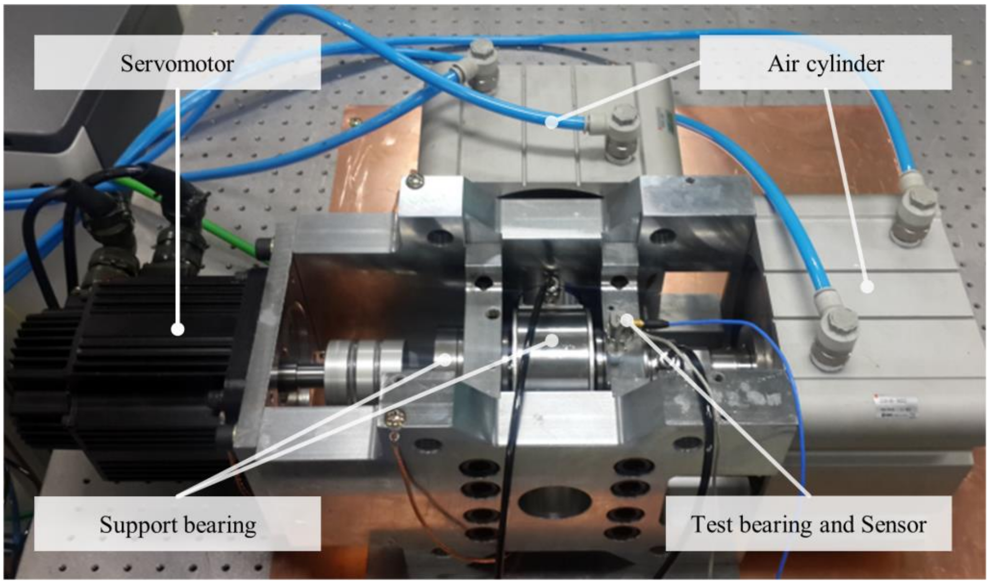

(a)

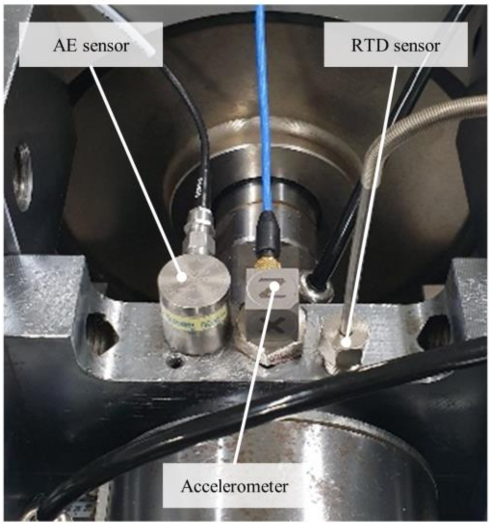

(b)

Figure 3-1 Configuration of the data acquisition system: (a) the bearing test rig, and (b) the AE sensor.

For the test bearing, an angular ball bearing, model 7202a from NSK Corporation, is used. This bearing supports both the axial and radial load of the shaft. The contact angle between the ball and raceway is 30 degrees. The sealing type is open, which facilitates disassembly of the bearing components. To emulate the defect of the bearing, a fault is artificially seeded on the inner raceway of the test bearing, as shown in Figure 3-2. The defect size is determined such that the defect signal is distinguishable from the noise. The examination of a severe defect helps to clearly show how effectively the proposed method filters out only the noise signal, by inspecting the removal or attenuation of the defect signal.

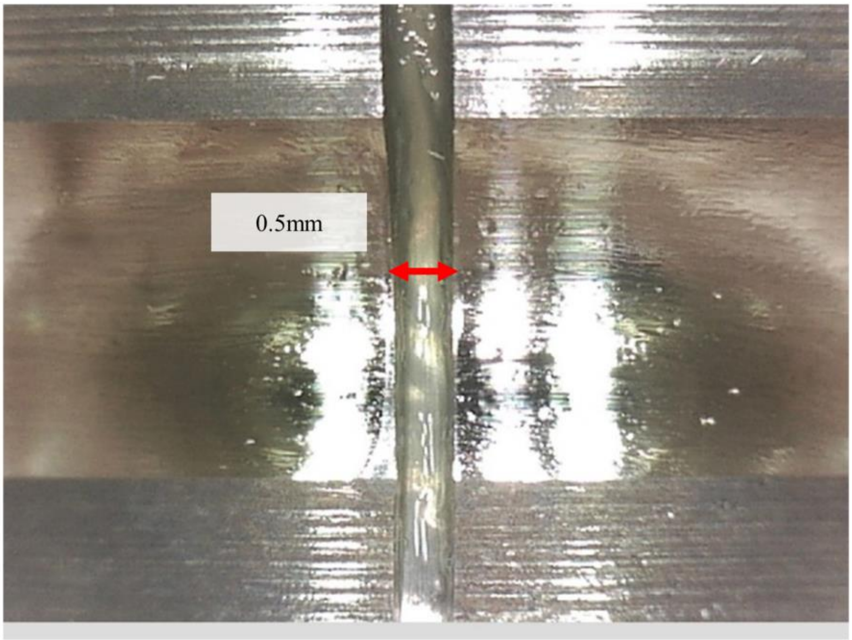

Figure 3-2 Artificial local defect on the inner raceway of angular ball bearing.

3.2 Configuration of Slewing Bearing Testbed

Figure 3-3(a) shows the overall configuration of the slewing bearing test rig. The electric motor and driver are located on the upper side of the bearing system and the shaft rotates vertically. The rotation speed of the motor is reduced to 1/60 through a gearbox. The bearing specimen is located on the end of the shaft and the axial force is applied by a hydraulic cylinder from the bottom of the bearing. The load cell between the specimen and the hydraulic cylinder measures the applied load on the specimen. As shown in Figure 3-3(b), the AE signal is measured through an acoustic emission sensor clamped by a magnetic holder on the housing of the outer raceway. The sensor, WSa from Mistras Inc., is a wideband resonance type with 55dB peak sensitivity, as with angular ball bearing data acquisition system in Section 3.1.

Figure 3-4(a) shows the test specimen. The inner and outer diameters of the test slewing bearing are 200mm and 360mm, respectively, and the weight of each specimen is 26kg. The artificial defect is made on the middle surface of the outer raceway, as shown in Figure 3-4(b). The artificial defect is intentionally generated to make the defect signal noticeable, despite stress wave attenuation that arises due to the distance gap between the sensor and the defect spot. In this experiment, the stress wave attenuation is inevitable because the sensor is installed away from the defect spot, in order to imitate the case of an unknown fault location.

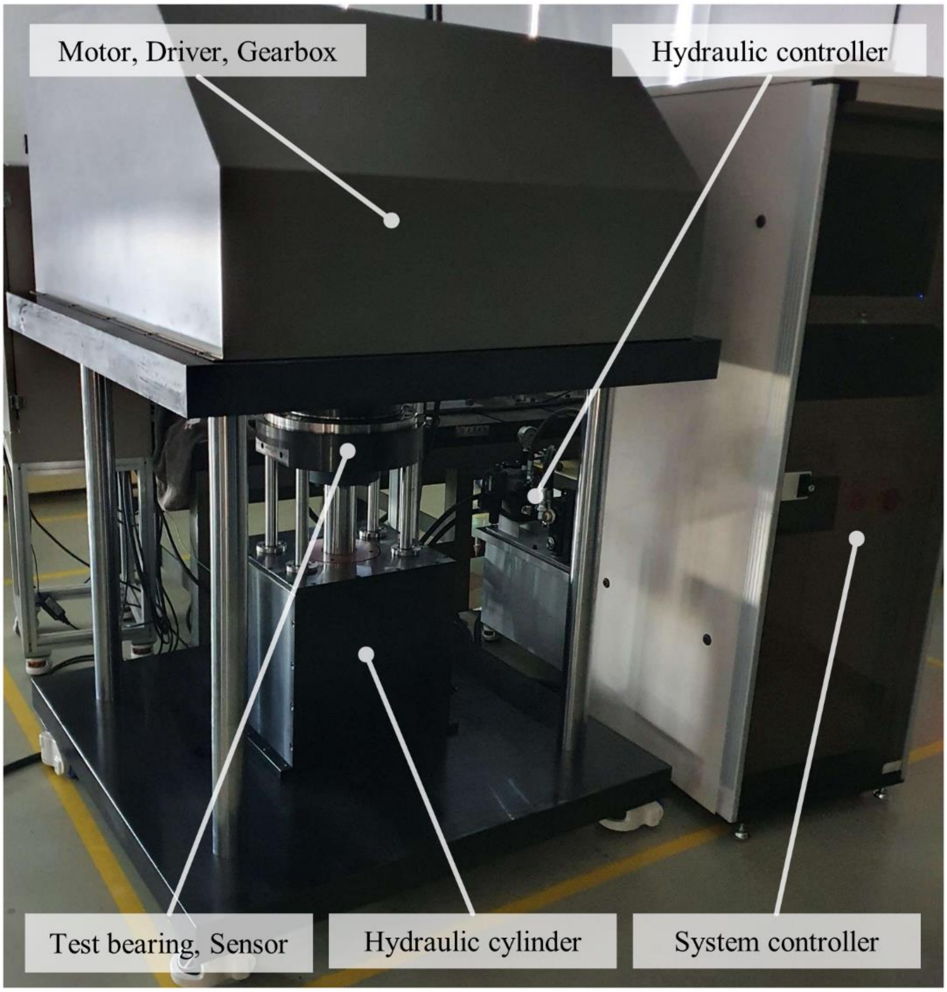
Motor, Driver, Gearbox
Hydraulic controller
Test bearing, Sensor
Hydraulic cylinder
System controller

(a)

Figure 3-3 Slewing bearing test rig: (a) overall configuration of the test rig, and (b) data gathering through the AE sensor.

(a)

(b)

Figure 3-4 Test specimen: (a) slewing bearing, and (b) artificial defect on the raceway.

Chapter 4

Noise-robust Frequency Band Selection with Segment based Efficient Searching

This chapter introduces the design of band selection process that is noise-robust and efficient for AE data. For successful bearing diagnosis, proper frequency band searching is inevitable. In addition, efficient and noise-robust band searching is necessary for the practical use of AE sensors in bearing diagnosis. The detailed sections of this chapter are organized as follows. Section 4.1 briefly explains the characteristics of a bearing's defect signal from the perspective of impulsiveness and periodicity, as an objective feature of band selection algorithm. Section 4.2 expresses the proposed optimized band-selection algorithm and the four steps of its procedure. Section 4.3 explains the generation of simulated signals to demonstrate the proposed band selection method, and the results are discussed. Section 4.4 describes the experimental data and the results of verifying the proposed band selection method. Finally, a summary and discussion of the research thrust are provided in Section 4.5.

4.1 Bearing Defect Characteristics for Optimum Band Selection

When any of the bearing's components have local defects (e.g., spalling or crack), the interaction between the defect and bearing elements results in periodic impacts during the operation. Nonetheless, detecting a bearing fault in a raw signal is almost impossible because the bearing signal is generally weak and buried by other dominant signals from the gearbox, motor, and shaft. To extract the bearing's defect signal from the noisy signal, the high-frequency part of the raw signal that contains transient resonances of the system that is generated by the defect impulse is used. However, extracting the target signal is challenging for several reasons. The resonance frequency differs across different systems and the spectral response is highly non-linear because the system is composed of many components. In addition, various kinds of high-frequency noise components could obscure the target signal. To effectively extract the proper frequency band, two characteristics of the bearing's defect signal – impulsiveness and periodicity – are used. The details of these two characteristics are explained in the following sections.

4.1.1 Signal Impulsiveness from Defect Impulses

A defect in a bearing generates locally large-amplitude signals, as compared to the normal state signal. Using this fact, an abnormality of a bearing can be detected. The statistical approach has been regarded as a simple and powerful methodology for this purpose. Many statistical moments have been considered for the measure of the abnormality; the fourth moment, the kurtosis, has been recognized as the most useful feature for detection of an abnormality. The kurtosis for sampled data, K_s, is defined as Equation (4.1).

$$K_s = \frac{\frac{1}{n}\sum_{i=1}^{n}(X_i - \mu)^4}{\left[\frac{1}{n}\sum_{i=1}^{n}(X_i - \mu)^2\right]^2} \tag{4.1}$$

In this equation, X_i is the i-th value from n sampled data and μ is the sample mean. A defect in a bearing generates an abnormal signal that is off the normal signal; it makes the tail of the distribution heavier, resulting in increased kurtosis [69]. Figure 4-1(a) shows the overlapped time domain plot of normal and fault signals, simulated by the MATLAB software. The Orange line represents fault data, and the blue line represents normal data. The fault signal has an additional periodic defect impulse, the amplitude of each instantaneous impulse pass over the amplitude level of normal states. Figure 4-1(b) shows histogram of each signals. Histogram of fault signal seems more widespread than normal case. Because multi-impulse make the signal distribution change as increase the thickness of the tail-end. This means more percentage of fault samples locates the edge side of the distribution.

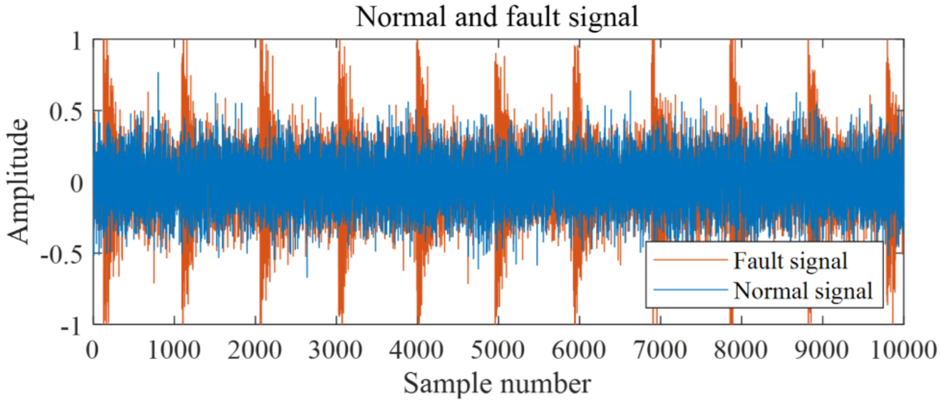

(a)

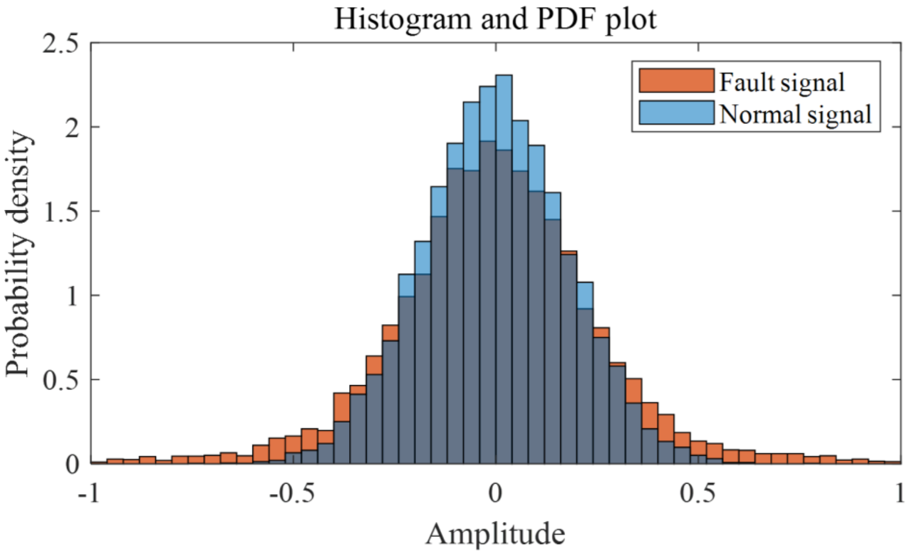

(b)

Figure 4-1 Simulated comparison between normal and fault signals (normal signal kurtosis≈3, fault signal kurtosis≈5): (a) time domain signal, (b) amplitude histogram for each signal.

On the other hands, Antoni extended the concept of time-domain kurtosis to the frequency domain, and proposed the formal definition of spectral kurtosis (SK) using Wold-Cramér decomposition of a conditionally non-stationary process [41]. Antoni also proposed the short-time Fourier transform (STFT) based SK estimator, which is shown in Equation (4.2).

$$K_X(f) = \frac{\langle |X_w(n,f)|^4 \rangle}{\langle |X_w(n,f)|^2 \rangle^2} - 2 \tag{4.2}$$

where Xw(n,f) is a complex envelope in terms of STFT for time-domain signal X(n), with narrow bandpass filtering around frequency f. <·> is the average operator and the 2nd order spectral moment in the denominator is the power spectral density in frequency f. The 4th and 2nd order spectral moments in Equation (4.2) deliver a kurtosis concept that is similar to that shown in Equation (4.1), which means the temporal energy dispersion of the envelope from a given signal around the target frequency. The visualization of SKs along the frequency bands is devised to show the SKs intuitively; this is called the Kurtogram. However, since the computation of SK for every frequency band is costly, Antoni developed the Fast Kurtogram (FK) [43] approach. FK uses a filter bank approach with a 1/3 binary tree and a simplified analytic filter to quickly compute the overall SK tendency. The strength of its rapid computing and good performance have resulted in FK becoming a powerful and widely used technique for mechanical fault diagnosis in industry.

The SK represents the kurtosis of an analytic signal that is filtered with target bands; its physical meaning is the energy significance in the squared envelope spectrum [46]. Although SK can extract the hidden impulsiveness and non-stationary information more effectively than simple time-domain kurtosis analysis, it still has intrinsic drawbacks related to the multi-component signals. The kurtosis value is easily activated by fault-irrelevant impulsiveness and disturbed by other components of the envelope spectrum. Those drawbacks are more critical for AE sensors because of their susceptibility to external disturbances, such as random impulsive noise from pressing, cutting processes, or the defects of other components.

4.1.2 Signal Periodicity from Defect Impulse Trains

A bearing's periodic defect impulses physically excite the resonance of the local bearing module. The amplitude of the resonance signal is modulated by the pulse of the defect frequency. These phenomena give clues for defect reasoning through high-frequency information and additional signal processing through demodulation and spectrum examination make accurate diagnosis possible. However, the additional signal processing requires further computing resources and in some cases (e.g., edge computing) it is not possible. Also, feature designs are needed in the spectrum inspection process to extract the engineer's intended information. The refinement of the features for noise robustness requires high-cost techniques, which can become an algorithmic burden.

The auto-correlation (AC) approach is a conceptually concise and powerful methodology for analyzing the periodicity of univariate time-series signals without additional spectral analysis. As a correlation-based method, AC quantifies the signal's self-dependency based on given time interval. The autocorrelation function (ACF) is widely used to analyze the self-dependency, along with the time intervals; further, it can determine the hidden periodicity of raw data as a function of time interval τ. The ACF is defined as shown in Equation (4.3).

$$R_{xx}(\tau) = E[X(t)X(t+\tau)] = \frac{1}{(n-\tau)} \sum_{i=1}^{n-\tau} [(X_i - \mu)(X_{i+\tau} - \mu)] \qquad (4.3)$$

μ, σ are the mean and standard deviation of n sampled signal X, respectively. $R_{xx}(\tau)$ represents the correlation coefficient between the raw signal and its lagged signal by τ. The large value of $R_{xx}(\tau)$ indicates that $X(t)$ has the tendency to repeat a similar pattern every τ period. In other words, $X(t)$ has a high chance of a defect signal with τ period. Figure 4-2 shows a schematic example of ACF derived using a simulated defect signal. Figure 4-2(a) is a simulated fault signal, where the defect impulse appears about every 1000 data points. As Figure 4-2(b) shows, the periodic defect impulse is observed in harmonic peaks, with the lag of the defect period.

The advantage of ACF in fault detection is its robustness against Gaussian and random noise. Due to this advantage, some researchers utilize ACF to preprocess for spectral analysis and band selection [29], [70]. The Autogram approach proposed by Moshrefzadeh and Fasana is a representative method that uses ACF for band searching [51]. Autogram can successfully detect the periodicity of a bearing's defect by wavelet preprocessing and ACF. Equation (4.4) shows the calculation of Autogram for optimum band searching.

$$K_A(X) = \frac{\sum_{i=1}^{N/2}\left[\hat{R}_{XX}(i) - \min\left(\hat{R}_{XX}(\tau)\right)\right]^4}{\left[\sum_{i=1}^{\frac{N}{2}}\left[\hat{R}_{XX}(i) - \min\left(\hat{R}_{XX}(\tau)\right)\right]^2\right]^2} \tag{4.4}$$

where $\hat{R}_{XX}$ is the auto-correlation where the input signal is a squared envelope of a decomposed signal from the wavelet packet.

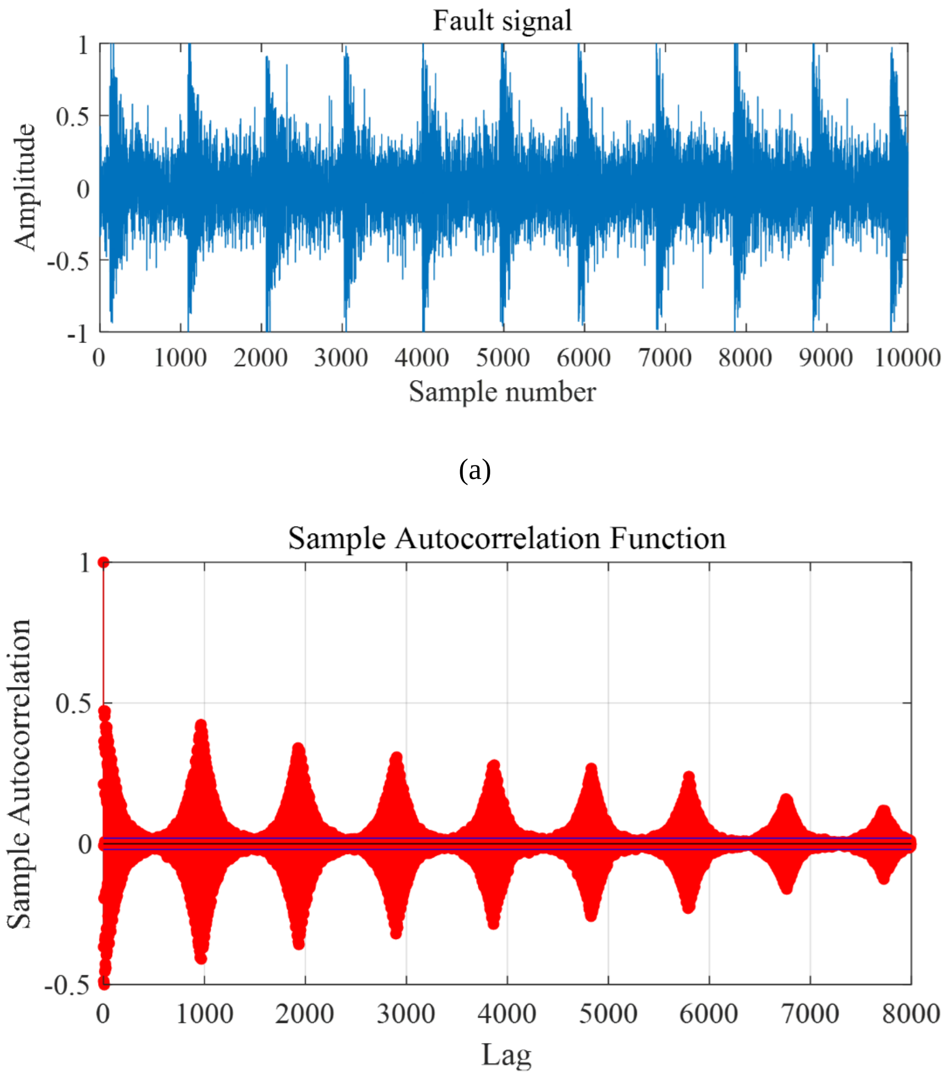

(a)

(b)

Figure 4-2 Simulated result of autocorrelation for a fault signal: (a) simulated fault signal, (b) autocorrelation function plot.

The ACF requires iterative calculation; thus, it is unsuitable for data with large sample sizes, such as AE data. In addition, since the correlation coefficient easily fluctuates due to other periodic sources, fault detection with ACF is often misled by cyclic non-Gaussian noise. Non-Gaussian periodic noises are prevalent in industry, and include such noises as motor, gearbox, transmission, transformer, and electrical devices (e.g., driver, inverter, switching system). These noise sources can easily corrupt AE signals by disturbing the defect-related information of the bearing in the signal.

4.2 Correlation and Kurtosis based Optimum Band Selection

Two approaches that have been proposed to capture defect-related information of a bearing – kurtosis- and autocorrelation-based methods – are introduced in the previous section. Kurtosis-based methods are good for identifying a periodic impulsive defect; however, they are vulnerable to other impulsive and non-Gaussian noise. In contrast, autocorrelation-based methods are robust for impulsive noise but are vulnerable to periodic noise. Because an AE sensor is easily corrupted by both impulsive and non-Gaussian noises, another method that can manage both types of noise is required. Several methods (e.g., spectral coherence) have been proposed to handle these various noises; however, they are numerically intense and are thus not suitable for an AE signal, which has a large sampling rate. Thus, a more effective band-selection algorithm is needed that is suitable for AE sensor data and robust to noise. To work to meet this need, this study proposes a new procedure for optimum band selection of AE sensor data. The proposed method aims to select the proper band under the conditions of various noises and massive sample sizes. To this end, correlation and kurtosis approaches are both adopted and combined to examine the characteristics of a bearing fault's impulsiveness and periodicity.

Figure 4-3 shows the overall procedure of the proposed method. It consists of four steps. In the first step, the raw AE data is decomposed to split the spectral information, using frequency windowing. Then, signal segmentation is applied to the decomposed signals as a preprocessing task before step 3. This preprocessing clarifies the defect signal through phase matching with selectable parameters. Next, step 3 quantifies the periodicity and impulsiveness of the defect signal using the proposed measure. Finally, the performance results of the candidate bands are compared, and the optimum band is selected. The selected band information can be subsequently utilized for bearing fault diagnosis. The details of each step are outlined in the next section.

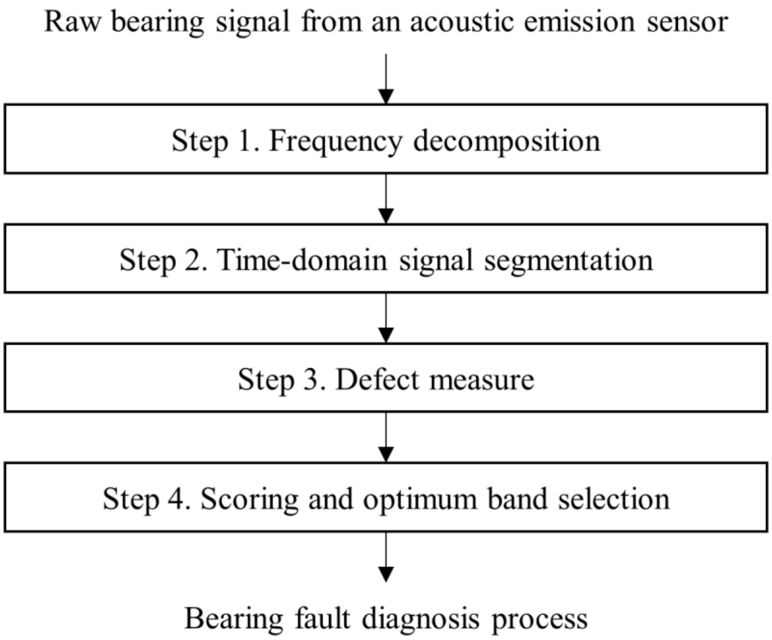

Figure 4-3 Flow chart of the correlation and kurtosis based optimum band selection.

4.2.1 Frequency Decomposition

The quality of band selection depends on the way the frequency range is decomposed. If the bandwidth of the decomposed bands is coarse, the band may have a high chance of containing defect-irrelevant information, as well as defect information. In contrast, if the bandwidth is too fine, the band may contain only partial information about the defect. There are several methods that may help systematic frequency decomposition, including bandpass-based meshing or the wavelet packet technique

[43]. These methods first divide the frequency range coarsely and then gradually increase the number of divisions along the level of the decomposition depth.

AE data requires a high level of decomposition for the sake of fine frequency meshing, due to its wide frequency range, which can be up to several mega-hertz. Further, each band carries a large number of sample points due to the high sampling rate. Both the wide frequency range and the high sampling rate of AE data bring about computational burden. To reduce the computational burden, it is necessary to carefully choose an adequate filter function to extract the frequency band. A simple shape filter has a short computation time; however, it is accompanied with significant distortion of the original signal during domain shifting. In contrast, a high-order filter induces little distortion, but is numerically costly. Furthermore, a narrowband filter usually demands a higher-order filter function, which causes the exquisite frequency investigation necessary for AE data to be impractical.

In this research, the Hanning window is adopted to consider the trade-off between signal distortion and computational cost. The Hanning window function for an M dimensional target vector is defined as follows [71].

$$w(m) = \begin{cases} 0.5\left(1 - \cos\left(2\pi \frac{m}{M}\right)\right), & 0 \le m \le M, \\ 0, & otherwise \end{cases} \tag{4.5}$$

where $w(m)$ is the window's weight value for the m-th index of the target vector. The Hanning window is the finite impulse response window function with a smooth tail and zero boundary values. Since the equation is formulated with a simple cosine function, fast computation is possible. Also, the Fourier transformed Hanning window locates around zero hertz; thus, the majority of the signal is less distorted by filtering [72].

The decomposition is conducted using frequency meshing with Hanning windows. Figure 4-4 shows the hierarchical frequency meshing and Hanning filter bank. The entire operating frequency range is divided into two types, based on decomposition level. The integer level splits the frequency range in a dyadic manner and the non-integer level divides the range into three from the previous decomposition level to prevent information loss on the borderline. The number of decomposed bands and bandwidths are 2^{lv} and $f_s/(2^{lv+1})$ at the integer level, and $2^{lv-1}\times 3$ and $f_s/(2^{lv+1}\times 3)$ at the non-integer level, where lv is the level of meshing and f_s is the sampling frequency.

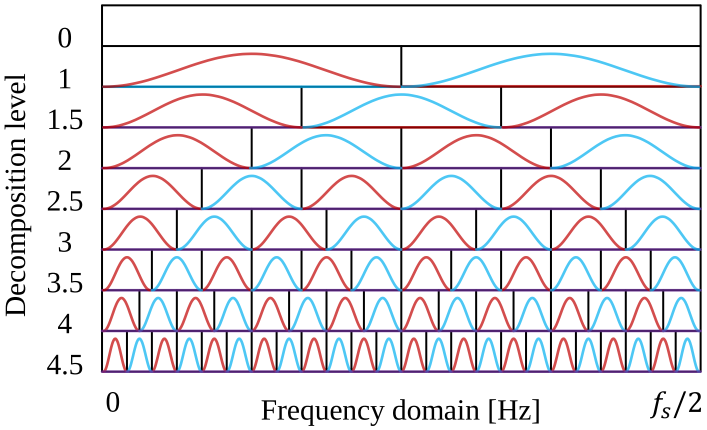

Figure 4-4 Hierarchical filter bank for signal decomposition in the frequency domain.

The *k*-th decomposed spectrum in the *lv* level is derived as shown Equation (4.6). In Equations (4.7) and (4.8), L and U are the lower and upper boundaries, respectively, of the *k*-th frequency band in the *lv* level.

$$F_k^{lv}(\omega) = F(\omega)w_k^{lv}(\omega) \tag{4.6}$$

$$L = \begin{cases} f_s(k-1)/2^{lv+1}, & lv \in \mathbb{Z}, \\ f_s(k-1)/(2^{lv} \times 3), & lv \notin \mathbb{Z} \end{cases} \tag{4.7}$$

$$U = \begin{cases} f_s k/2^{lv+1}, & lv \in \mathbb{Z}, \\ f_s k/(2^{lv} \times 3), & lv \notin \mathbb{Z} \end{cases} \tag{4.8}$$

Each decomposed spectrum includes different spectral information through the filter bank and becomes a candidate for the optimum defect band.

4.2.2 Time-domain Signal Segmentation

Each decomposed spectrum from step 1 has different spectral information (e.g., frequency center and bandwidth). Some may contain abundant defect information and some may not. To find out the amount of defect information a frequency band has, a proper measure is required. The defect measure will be introduced in the next section. In this section, as a preprocessing step, each decomposed spectrum is transformed into time-domain segmented signals to clarify the defect feature.

The process is as follows. The decomposed spectrums from Section 4.2.1, $F_k^{lv}(\omega)$, are transformed back to time-domain signals using the inverse Fourier transform, resulting in $X_k^{lv}(t) = \Phi^{-1}[F_k^{lv}(\omega)]$. The time-domain signal $X_k^{lv}(t)$ is then segmented with a length of defect period of $1/f_d$, so that each segment has *n* data points and equal phase of the defect frequency. The number of divided segments, n_s, is defined by Equations. (4.9) and (4.10), and the size of the segment vector, n_{seg}, is calculated by Equation (4.11).

$$n_s = \left\lfloor \left(\frac{n_d - D}{S} + 1 \right) \right\rfloor \tag{4.9}$$

$$n_d = \left\lfloor \left(\frac{n}{f_s \times f_d} \right) \right\rfloor \tag{4.10}$$

$$n_{seg} = \frac{f_d}{f_s} \times D \tag{4.11}$$

where $\lfloor \cdot \rfloor$ indicates round-down operations, and n_d is the number of defect impulses in a given n-length signal, which determines n_s by using selectable parameters D and S. D indicates the number of defect impulses in each segment, and S means stride for the moving window filter. A large S decreases the computational burden by diminishing n_s. Also, a large S could be helpful for considering the modulation of the defect signals. However, a large S can also cause phase dislocation of defect impulses between segments because of bearing slip effects or uncertainty in defect periods. On the other hand, an increase of parameter D can reduce n_s by containing more defect impulses in a segment. However, it also increases the segment length, which makes the segment include low-frequency noise that has large energy and disturbs the ability to find the defect impulse. In general, a large n_s tends to secure the robustness in detecting a defect under noisy conditions by avoiding the signal's local singularities; however, it also increases computational cost, and vice-versa.

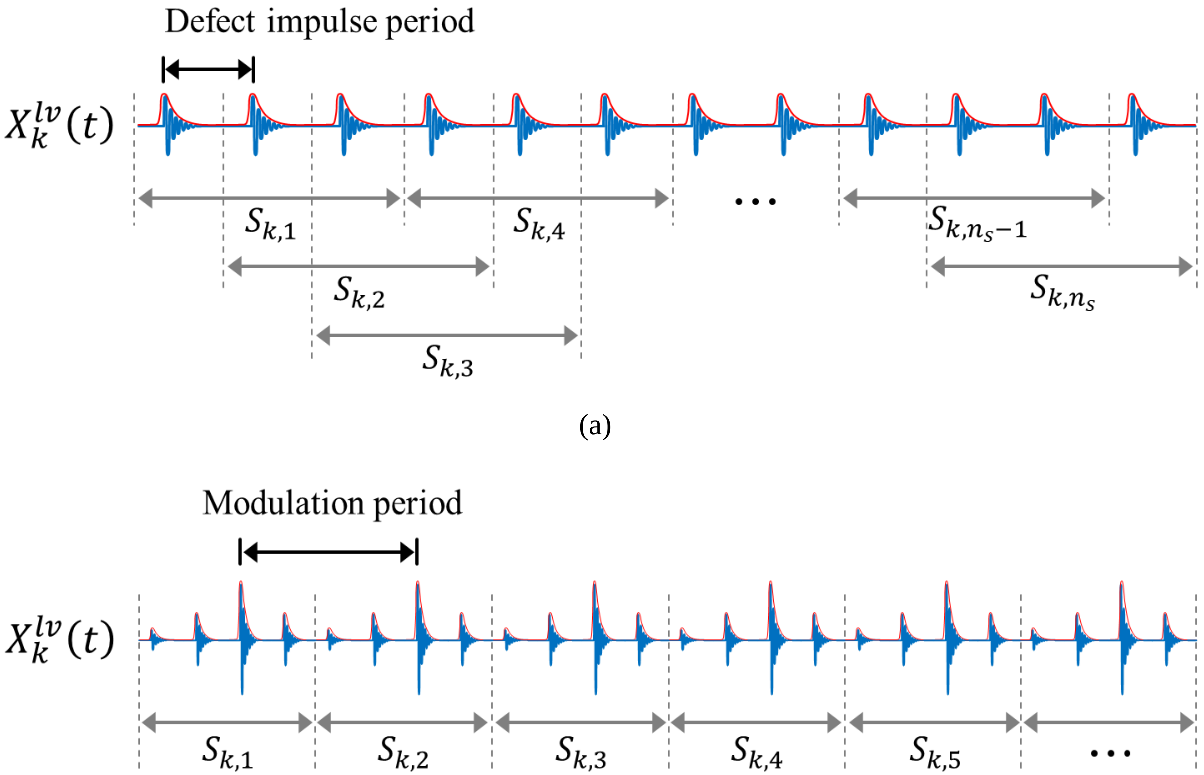

(a)

(b)

Figure 4-5 Signal segmentation of a modulated defect signal: (a) D=3 and S=1, and (b) D=4 and S=4.

Figure 4-5 illustrates the signal segmentation process for two different cases. The *l*th segmented signals are denoted by $S_{k,l}$, and all of the segments have the same phase of the defect. Figure 4-5(a) shows segmentation of the signal with constant amplitude defects. The segmentation parameters are set to be D=3 and S=1. Figure 4-5(b) targets the modulated defect signal. In this case, the modulating frequency is 4×defect periods. Since the bearing's main modulation is related to the geometry of the bearings, the modulating frequency can be easily inferred, even in real cases. As shown in Figure 4-5(b), proper adjustment of parameters allow the defect train to group even in the case of an inconstant amplitude defect by modulation.

Meanwhile, if the measured signal carries too many defect cycles, n_s needs to be limited to include fewer defect cycles. The authors suggest a maximum number of n_s with 30 segments, based on the statistical central limit theorem. In the later section of this research, the parameters are fixed with the value of one, and n_s is limited to 30.

4.2.3 Defect Measure

In this section, the amount of defect information in the *k*th decomposed signal, $X_k^{lv}(t)$, is measured to select the optimal band. The metric is defined as shown in Equation (4.12).

$$M = \frac{1}{n_s - 1} \sum_{k=1}^{n_s-1} R(S_{k,l}, S_{k,l+1}) \times \frac{1}{n_s} \sum_{l=1}^{n_s} K_s(S_{k,l}) \tag{4.12}$$

$$R(X,Y) = \frac{1}{n}\sum_{i=1}^{n}\frac{(X_i - \bar{X})(Y_i - \bar{Y})}{\sigma_X \sigma_Y} \tag{4.13}$$

where $S_{k,l}(t)$ denotes the lth segmented signal of $X_k^{lv}(t)$ at step 2, $R(\cdot,\cdot)$ is the Pearson correlation coefficient defined as Equation (4.13), and $K_s(\cdot)$ is the kurtosis of the target signals. The multiplication is used in this study to combine kurtosis and correlation factors, the method used to combine the two measures can be improved by considering the nonlinear form in future research.

The measure is composed of two parts. The first part is the average of the Pearson correlation coefficient between adjacent segmented signals. The Pearson correlation coefficient quantifies similarity between signals in a bounded manner. It helps to capture the periodic defect impulses with numerically stability. If the kth decomposed signal, $X_k^{lv}(t)$, has defect impulses and is segmented as described in step 2, the segments have similar shapes, leading to a high Pearson correlation coefficient. On the other hand, if the decomposed signal has no defect impulses, the segments have low repeatability, resulting in a low Pearson correlation coefficient.

The latter part of Equation (4.12) contains the kurtosis and it quantifies the impulsiveness of the bearing defect. Unlike the traditional kurtosis-based approach, which calculates the kurtosis of the whole signal as $K_s(X_k^{lv}(t))$, here the kurtosis is calculated for each segment, as $K_s(S_{k,l}(t))$, and the values are averaged. Through this approach, the impulsive noise is averaged out. As a result, the proposed method can concentrate on defect impulses instead of various potential noises that bias the kurtosis of the measured signals.

In summary, the proposed method simultaneously considers local periodicity and global impulsiveness through Equation (4.12). Local signal correlation of adjacent segments enables the algorithm to avoid long-term effects in the time domain, such as slip, signal lagging, and inevitable modulated noise with massive energy. On the other hand, the global kurtosis from the segmented signal makes the algorithm observe the overall impulsiveness from the bearing defect. These two features complement each other, allowing the objective function to be robust for both types of noise at the same time: random impulsive and periodic non-Gaussian.

4.2.4 Scoring and Optimum Band Selection

The calculated defect measures for overall frequency meshing from Section 4.2.1 are compared to select the optimum bands. Each frequency band is scored by the defect measure found in Section 4.2.3, and the frequency band with the highest score is selected. In addition, the result of the defect measures can be mapped in a two-dimension hierarchical plot, as done in the visualization of traditional –gram techniques.

Figure 4-6 shows an example of 2-dimensional visualization of scoring and searching results of the optimum frequency band. The X-axis represents the target frequency domain, and it is divided according to Y-axis, the decomposition level. Each rectangle block in the 2-dimension space represents the objective defect measure value on the corresponding frequency band. In the figure, the frequency band around 4500 Hz is highlighted, and it can be inferred that the bearing failure-related information is in the corresponding frequency band.

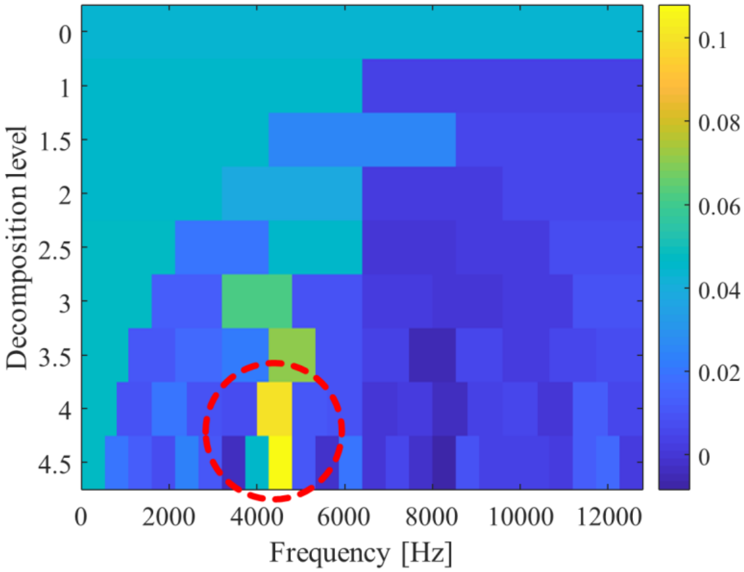

Figure 4-6 A 2-dimension hierarchical plot for optimum band searching using proposed defect measure.

4.3 Simulated Validation of the Proposed Method

This section demonstrates the proposed band selection method using simulated data. The simulated signal is a combination of various signals, including the bearing, gear, and noises, to represent a real-life situation. To verify the effectiveness of the proposed method under noisy conditions, two kinds of noise are added: impulsive and cyclic non-Gaussian noises. The impulsive noise reflects random impulses coming from the surrounding modules or the systemic impact. For cyclic non-Gaussian noise, electromagnetic interference (EMI) from a motor drive is considered; this is captured in the AE sensor and hinders the diagnosis of the bearing. The details of the synthetically generated data are reviewed in Section 4.3.1, and the results of the proposed method are described and analyzed in Section 4.3.2.

4.3.1 Simulation Data Design

The simulation signal, $x(t)$, includes the signals of six components, including the: shaft (x_s), gear (x_g), bearing defect (x_{bd}), impulsive noise (x_{in}), EMI (x_{EMI}), and white Gaussian noise (n), as shown in Equation (4.14). The coefficient a_i is the amplitude of each signal. In this simulation, the signal-to-noise ratio (SNR) of the Gaussian noise is set to 30dB.

$$x(t) = a_1 x_{sh} + a_2 x_g + a_3 x_{bd} + a_4 x_{in} + x_{EMI} + n \tag{4.14}$$

First, the shaft and gear signals are represented with simple sinusoidal functions with frequency f_{sh} and f_g, respectively.

$$x_{sh}(t) = \sin(2\pi t f_{sh}) \tag{4.15}$$

$$x_g(t) = \sin(2\pi t f_g) \tag{4.16}$$

The bearing defect signal, x_{bd}, is formulated as follows.

$$x_{bd}(t) = \left\{ [\sin(2\pi t f_r) * e^{-\alpha t}] \otimes \sum_{k=-\infty}^{\infty} \delta\left(t - k\frac{1}{f_d}\right) \right\} \tag{4.17}$$

The sine function represents the oscillation by defect impulses with resonance frequency (f_r). The exponential term indicates the damping effect of the signal with decaying parameter α. Then, the decaying impulse is convoluted to the Dirac comb function with an interval of the bearing defect periods ($1/f_d$) to make periodic defects. Figure 4-7 visualizes the formulating procedure.

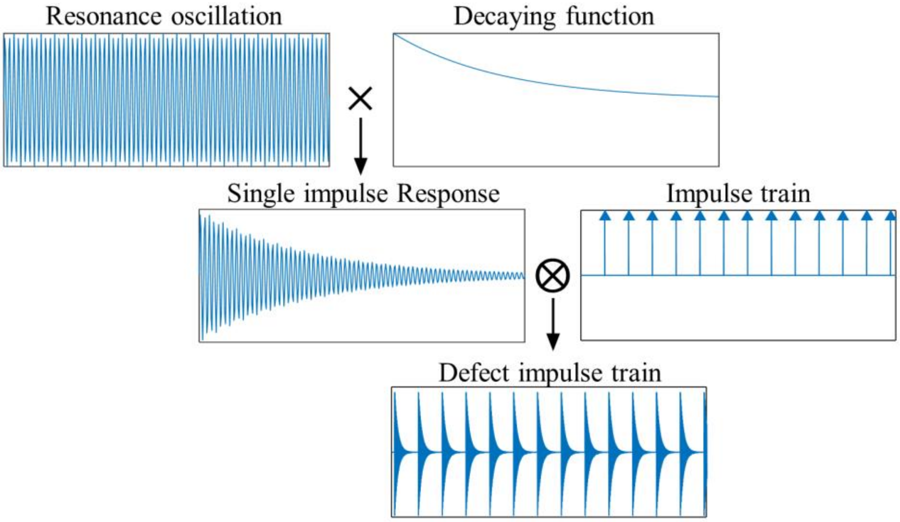

Figure 4-7 The process of generating the defect signal of a bearing.

External impulsive noise, x_{in}, has another resonance frequency that is unlike the target bearing defect. Equation (4.18) shows that it oscillates with the noise resonance frequency (f_n) and exponentially decays like the defect impulse. It is noted that x_{in} is non-cyclic and excited only once during the measurement.

$$x_{in}(t) = \sin(2\pi t f_n) * e^{-\alpha t} \tag{4.18}$$

Finally, x_{EMI} represents the electrical noise from the electric motor and drive systems. This noise is observed in the AE data and disturbs the frequency information [60]. Because the frequency response of EMI is highly complicated, depending on the operating conditions, analytic simulation of EMI is very intricate and difficult. Nevertheless, Kim et al. studied the spectral effect of EMI on an AE signal, and showed that the switching frequency from the inverter and electrical driving frequency from the motor drive is important [58]. Based on previous research, in this research, two dominant components are considered for simplicity: the inverter and the motor drive. The suggested simulated EMI is formulated in Equation (4.19).

$$x_{EMI}(t) = a_5 \sum_{k=1}^{\left\lfloor \frac{f_s}{2*f_{sf}} \right\rfloor} \left[\sin\left(2\pi t \times k f_{sf}\right)\right] + a_6 f_{PWM}\left(\sin(2\pi t \times f_{ef})\right) \tag{4.19}$$

The first term indicates the switching noise from inverters when converting DC to the desired AC motor input. It consists of multi-components with a sinusoidal function of the switching frequency, (f_{sf}), and its harmonics. The index k is an integer up to affordable harmonics of f_{sf} within the target signal's observing frequency. The second part of Equation (4.19) indicates pulse-width modulation (PWM) noise from the motor drive. It is one of the primary causes of EMI from electric devices for variable-frequency controls [65]. The sinusoidal function with electrical frequency, f_{ef}, is the desired continuous motor input for current operating speed. However, complicated rectification of the input signal is inevitable when converting and inverting the supplying voltage. The f_{PWM} represents the effect of the rectification process on the input signal. It reshapes the continuous electric frequency waveform in a discrete manner, with the resolution of the switching frequency.

The parameters of the simulated signal are given in Table 4-1. The total number of samples for the simulated signal is 1.28×10^6, equivalent to 10 seconds of measuring with 128k/sec of sampling frequency (f_s). The virtual rotation speed of the shaft (f_{sh}) is 1200 RPM, and the gear (f_g) operates five times faster. The bearing defect frequency (f_d) is calculated as 132.48 Hz by setting the unit defect frequency of the target bearing as 6.624 Hz. The resonance frequency (f_r) is 24 kHz, and the impulsive noise oscillates at 13 kHz. The switching frequency noise (f_n) from the virtual inverter system is set to 10 kHz, and the electrical frequency of the motor (f_{ef}) is set to 160 Hz considering the eight pole-pairs of the motor system.

Figure 4-8(a) shows each component in Equation (4.14) without additional Gaussian noise. The SNR of the bearing defect power to the others is about -40dB. It is a highly noisy condition with electric and dynamic components, where the AE sensor has difficulty diagnosing the system. Figure 4-8(b) represents the resulting time domain signal, the superposition of all of the components from Figure 4-8(a) with additional Gaussian noise. The overall shape of the signal follows the components with large energy, and the impact and bearing defect are unrecognizable. Figure 4-8(c) illustrates the spectrum of the simulated signal. The defect-related resonance frequency appears around 24kHz. Additionally, there are many spectral peaks throughout the frequency domain. The high-frequency noise from the impulsive components is barely visible in the spectrum around 13kHz because it is temporal excitation and has low energy. The vertical peaks at every harmonic of 10kHz are generated from the former part of Equation (4.19). The other peaks come from the PWM noise, which seems to be affected by the complex modulation effect of f_{sf} regarding f_{ef}.

Table 4-1 Frequency parameters of the simulation data.

Parameter	Physical meaning	Values [Hz]
f_s	Sampling frequency	128000
f_{sh}	Shaft rotating frequency	20
f_g	Gear rotating frequency	100
f_d	Bearing defect frequency	132.48
f_r	Bearing resonance frequency	24000
f_n	Impulsive high-frequency noise	13000
f_{sf}	Switching frequency of the inverter	10000
f_{ef}	Electrical frequency of the motor	160

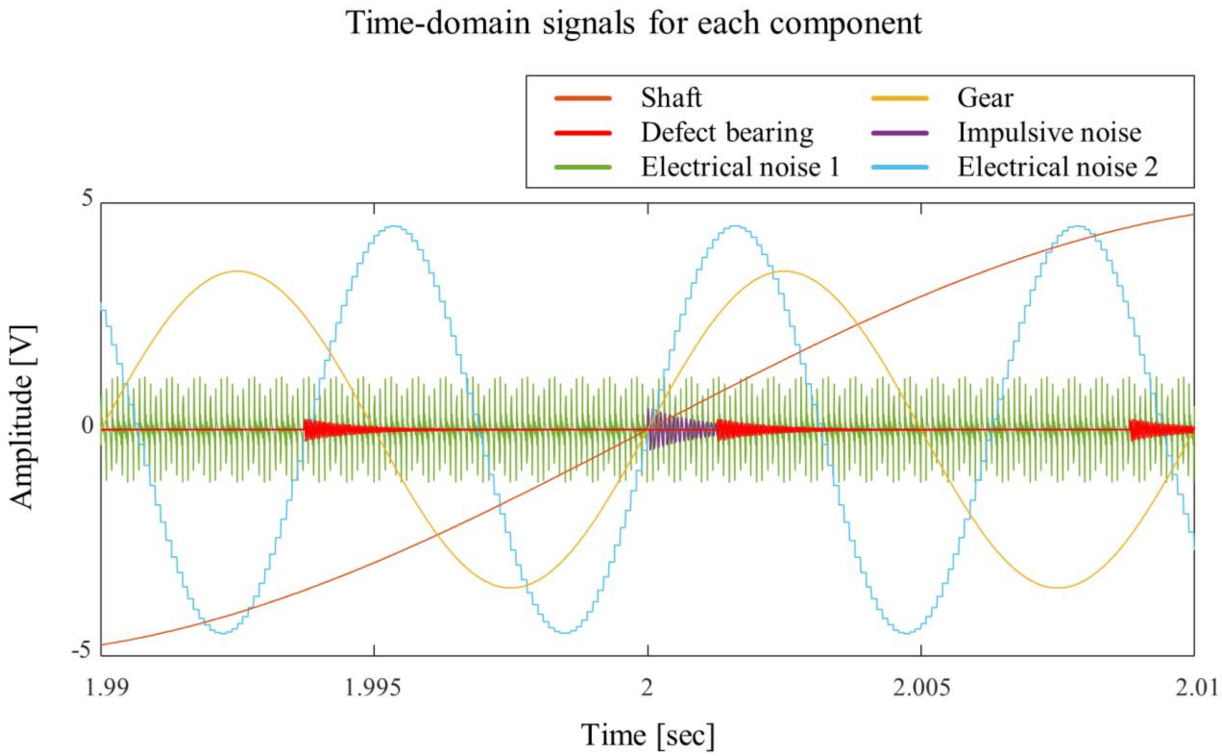
Time-domain signals for each component
Shaft
Gear
Defect bearing
Impulsive noise
Electrical noise 1
Electrical noise 2
5
0
-5
Amplitude [V]
1.99
1.995
2
2.005
2.01
Time [sec]

(a)

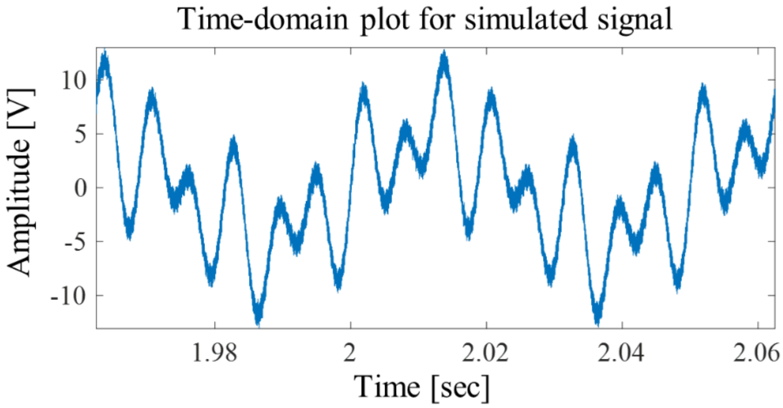

(b)

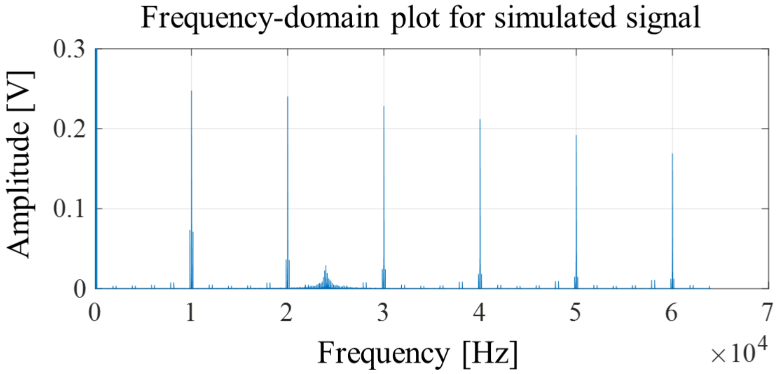

(c)

Figure 4-8 Illustrations for the simulated signal: (a) schematic plot for multi-components without the addition of Gaussian noise, (b) time-domain plot for the simulated signal, and (c) spectrum of the simulated signal.

4.3.2 The Results for Simulated Validation

The proposed method for band selection is applied to the simulated data. The performance of the proposed method is compared with the traditional Fast Kurtogram (FK) and Autogram approaches. Figure 4-9 illustrates the results of band selection for each method, and the detailed selected parameters are listed in Table 4-2.

Figure 4-9(a) shows that the Kurtogram method picks up 13kHz, which is related to the impulsive noise, rather than the defect frequency, 24kHz. Although there is weak evidence that the Kurtogram is interested in the defect frequency, it is strongly attracted to 13kHz. The reason that the Kurtogram picks the frequency for impulsive noise despite the low and temporal energy level of the impulse signal is the sensitiveness of spectral kurtosis to the impulsiveness of the signal. Unlike the Kurtogram, Figures 4-9 (b) and (c) show that Autogram approach and the proposed method deliver the correct band selection.

Table 4-2. The results of band-selection for the simulated data.

	Fast Kurtogram	Autogram	Proposed method
Level	6	5	4.5
Frequency center [Hz]	13500	23000	25333
Bandwidth [Hz]	1000	2000	2667

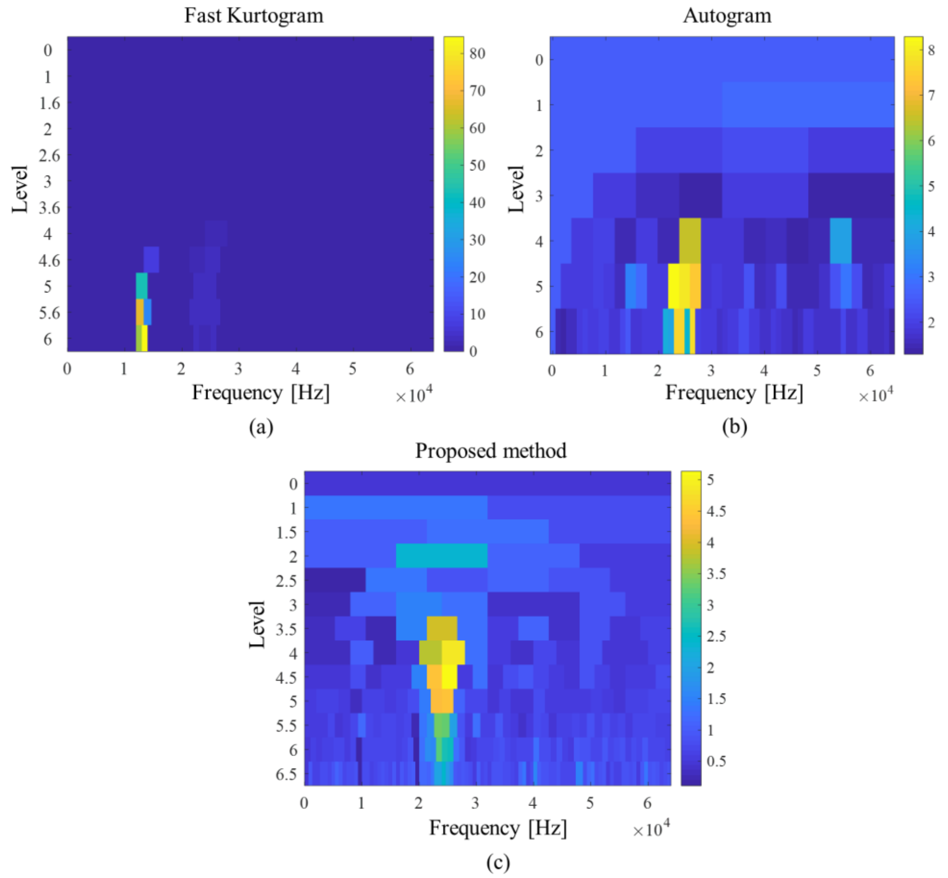

(a)

(b)

(c)

Figure 4-9 The results of each band selection algorithm for the simulated signal: (a) FK, (b) Autogram, and (c) proposed method.

Figure 4-10 shows the band-passed signals with the selected frequency band and their envelope spectrums. Figures 4-10 (a) and (b) are the results of Kurtogram. These figures show that the selected frequency band rarely captures the periodic defect signal. Leaking defect energy during band-pass filtering generates several peaks, according to the target defect frequency in the envelope spectrum, and the background noise level is relatively large. Figures 4-10 (c) to (f) are the results of Autogram and the proposed method. Both methods properly catch periodic defect patterns in the time-domain signals. The defect frequency at 132.48 Hz and its harmonics clearly appears in the envelope spectrum domain with little spectral noise.

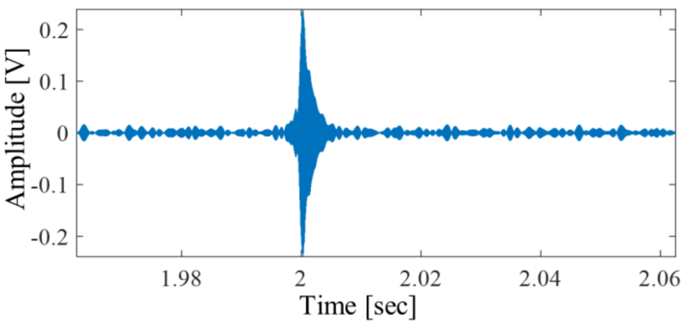
Amplitude [V]
0.2
0.1
0
-0.1
-0.2
1.98
2
2.02
2.04
2.06
Time [sec]

(a)

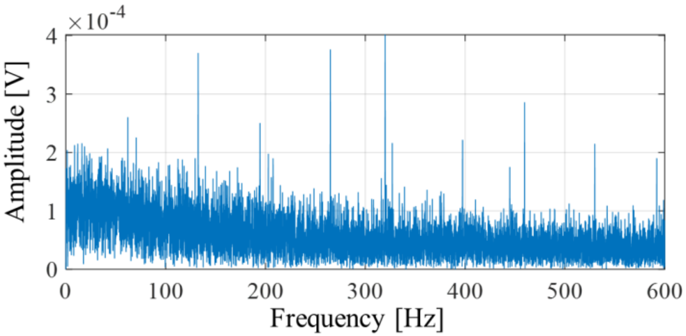
×10^-4
Amplitude [V]
4
3
2
1
0
0
100
200
300
400
500
600
Frequency [Hz]

(b)

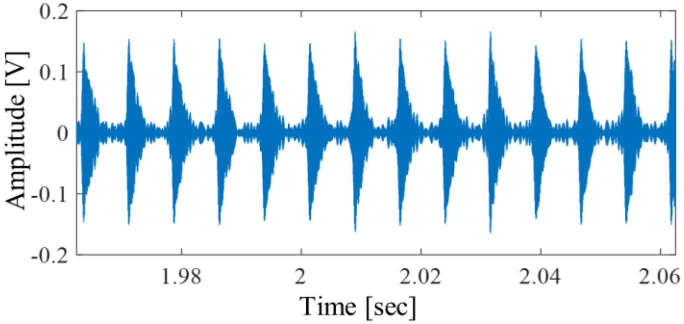
Amplitude [V]
0.2
0.1
0
-0.1
-0.2
1.98
2
2.02
2.04
2.06
Time [sec]

(c)

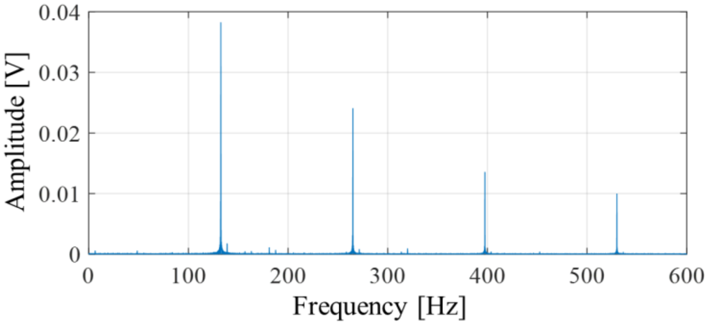
Amplitude [V]
0.04
0.03
0.02
0.01
0
0
100
200
300
400
500
600
Frequency [Hz]

(d)

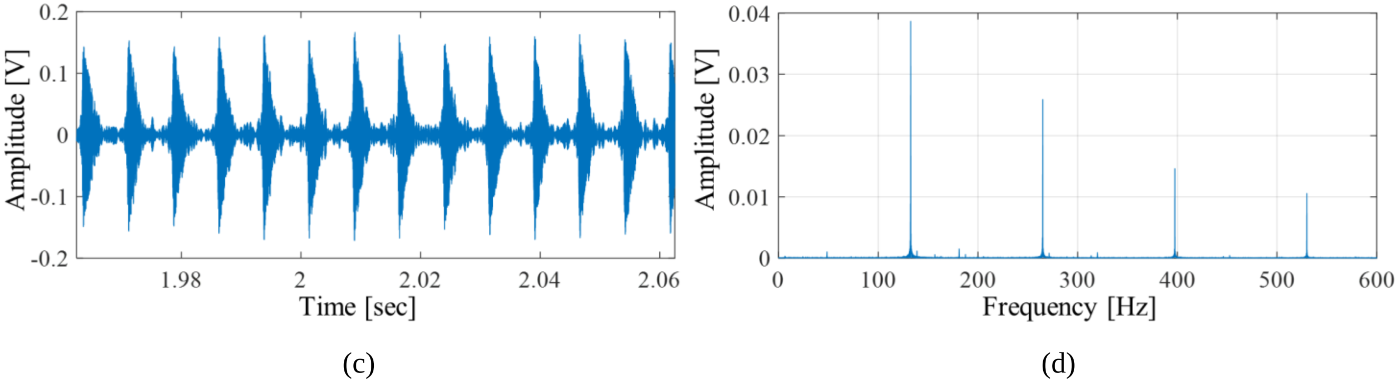

(c) (d)

Figure 4-10 Band-pass signals and envelope spectrums at the selected frequency band, as found by each band-selection method for the simulated signal: (a), (b) Fast Kurtogram, (c), (d) Autogram, (e), (f) the proposed method.

Figure 4-11 shows the detailed ACF analysis of Autogram's results for the simulation data. The graph represents the autocorrelation of the envelope signal filtered by wavelet at the selected band. As shown in the figure, the signal selected by Autogram has periodic patterns with an interval of about 967 data points. This interval corresponds to the defect periods of the bearing, which means that Autogram successfully extracts the fault-related frequency bands. The correlation values of the peaks are close to 0.95, representing that the defect components are dominant in the filtered signal.

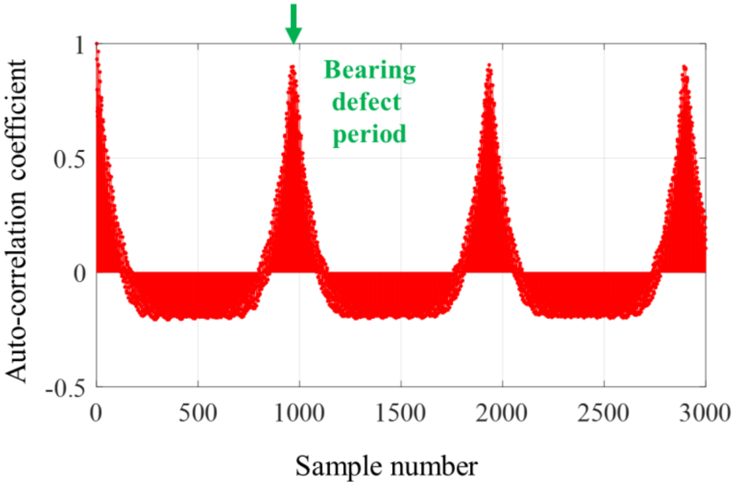

Figure 4-11 Autocorrelation function of the simulated signal filtered by the optimally selected band from Autogram.

Figure 4-12 illustrates a sequence of segment signals, $S_{k,l}$, for the selected frequency band of the proposed method. It is observed that the dominant pattern of each segment is similar. This means that all segments represent the periodic bearing's defect well through a set of single impacts with the same phase.

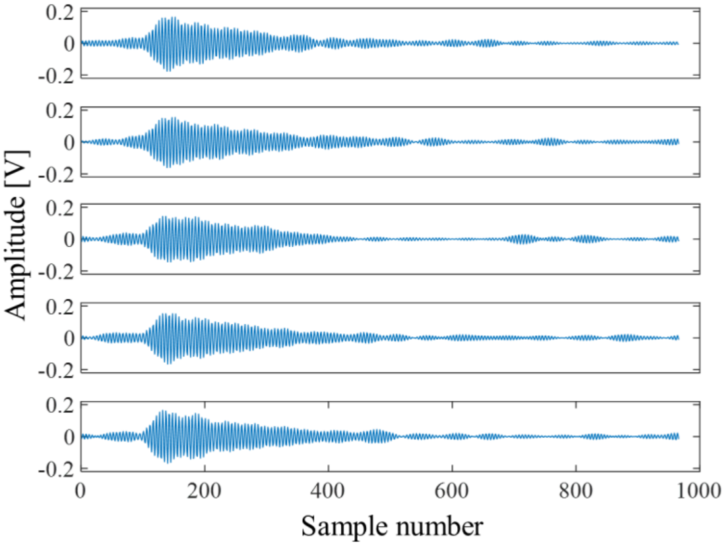

Figure 4-12 Sequence of segment signals ($S_{k,l}$) with index l=1~5 at the selected band for the simulated data.

Figure 4-13 shows the results of the comparison study for each method's computing time. The results are displayed through box plots; each box has 50 samples for the consuming time value. Every iteration is performed with an identical algorithm, without a random number generation process for Gaussian noise adding. The decomposition level is fixed at six for every method. Fast Kurtogram, as expected, has the best computing cost, regardless of diagnostic performance. Most of the samples are located between one and two seconds. Autogram shows the worst results from among the objective methods for over a minute, even though it does not carry out 1/3-binary tree decomposition. The proposed method has better performance; it is more than three times faster than Autogram, even with the additional 1/3-binary tree analysis. The detailed wavelet analysis in Autogram might cause additional time costs. However, the main reasons for the difference in calculation time seem to come from the algorithmic process. Autogram examines all the lag of given samples for auto-correlation analysis. However, the proposed methods examine the correlation analysis only for a limited number of preprocessed signals using the defect period, as mentioned in Section 4.2.2.

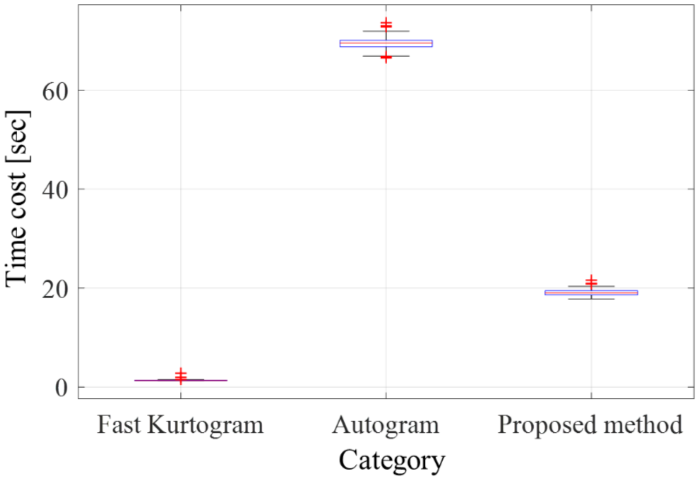

Figure 4-13 Comparison of calculation time for each method.

To investigate the noise robustness of the proposed method under the potential extremely harsh conditions of AE sensors, experimental analysis in a low-SNR case is carried out for simulated data. The SNR level is controlled by decreasing the energy of x_{bd} in Equation (4.14). The bearing defect power, in relation to the others, is set to about -55 dB, which means a harsher condition for fault detection than that of the case of Figure 4-9. Figure 4-14 displays the results of band selection for each method in the low-SNR case, and the detailed selected parameters are listed in Table 4-3. The FK has the same result as the previous case study with impulsive noise selection. The faintly visible defect bands in Figure 4-9 (a) no longer appear as a result of the low defect energy. Autogram approach and the proposed method have different results, unlike in Figure 4-9. Figure 4-14(b) shows that Autogram approach chooses the high-frequency band irrelevant to the bearing's defect; however, the proposed method correctly selects the band that carries the defect information. Compared with the high-SNR case in Figure 4-14(c), defect bands are not highlighted well throughout many levels, and the optimum bandwidth is enlarged because of the small energy of the defect.

Table 4-3. The results of band-selection for the simulated data with low SNR.

	Fast Kurtogram	Autogram	Proposed method
Level	6	4	3.5
Frequency center [Hz]	13500	54000	24000
Bandwidth [Hz]	1000	4000	5333

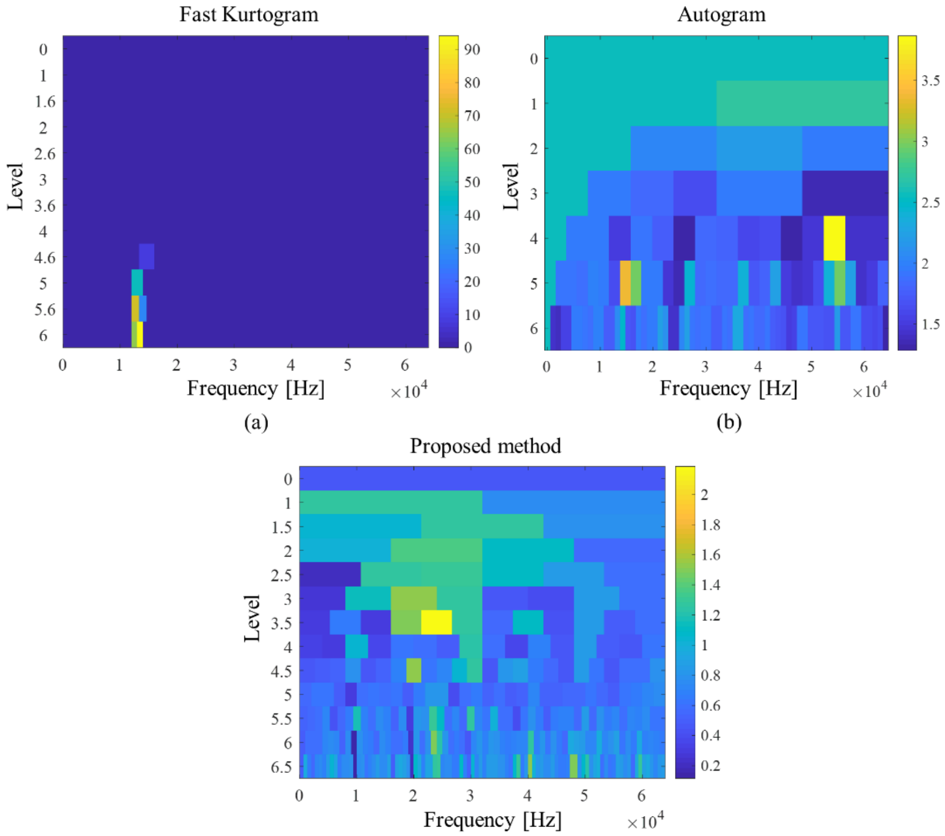

(a)

(b)

(c)

Figure 4-14 The results of each band selection algorithm for a simulated signal with low SNR: (a) Fast Kurtogram, (b) Autogram, and (c) the proposed method.

Figure 4-15 represents the band-pass signals and envelope spectrums of selected bands for the low-SNR cases. Kurtogram has a similar result to the high-SNR case, which focuses on impulsive noise components. Figure 4-15(b) shows a spectrum that gradually attenuates as it goes up to high frequency due to the impulsive noise. The leaking defect energy that was slightly visible in Figure 4-10(b) is no longer visible, and only the 320Hz component, which is the second harmonic of motor noise, appears. The time-domain results of Autogram incorrectly selected the band. Here, it seems that the signal does not have any particular pattern, like white Gaussian noise; however, Figure 4-15 (d) shows the spectral features that only have motor-related components prominently. The failure of Autogram seems to be caused by the intrinsic character of auto-correlation (AC). AC can easily filter out uncorrelated components, such as random impulses or non-periodic components. However, because it thoroughly examines all the time lags for given signals, other cyclic components occupying a large proportion of energy (i.e., gear, coupling, and electrical noise) could be easily triggering the decision parameter. In this study, the simulated signal is generated to suppose an electrically harsh condition, which might induce Autogram’s failure. On the other hand, the results of the proposed methods demonstrate that it can successfully find the optimum bands for the defect signal, despite the low-SNR condition Figures 4-15 (e) and (f) represent that the periodic defect patterns are clearly shown in the time domain, and the defect-related frequency components stand out in the envelope spectrum domain.

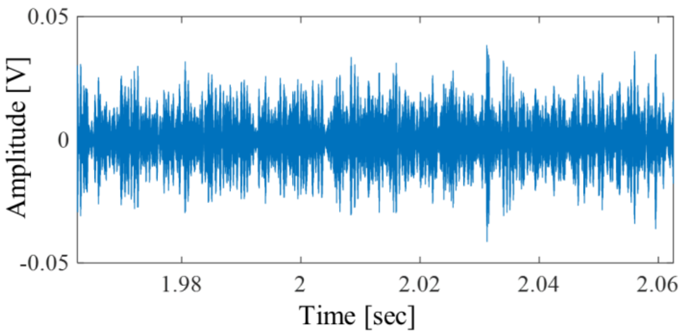
0.05
0
-0.05
Amplitude [V]
1.98
2
2.02
2.04
2.06
Time [sec]

(a)

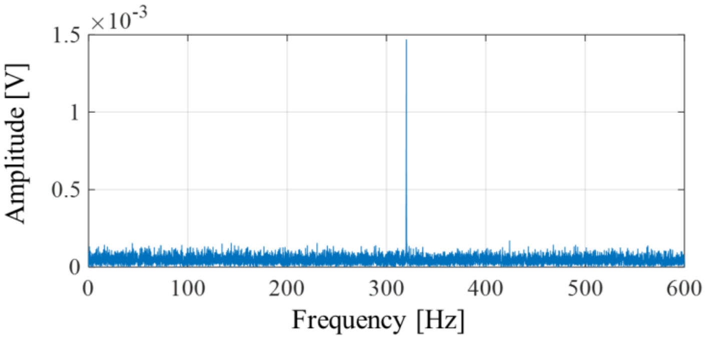
×10^-3
1.5
1
0.5
0
Amplitude [V]
0
100
200
300
400
500
600
Frequency [Hz]

(b)

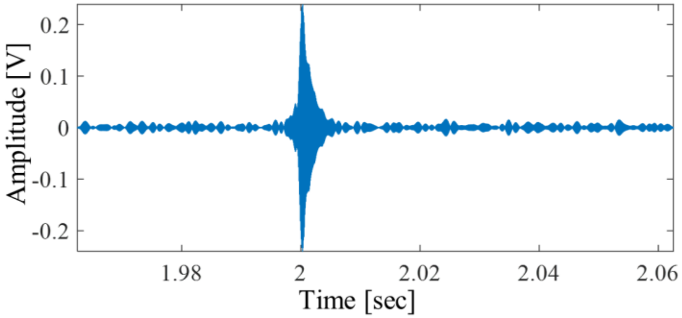
0.2
0.1
0
-0.1
-0.2
Amplitude [V]
1.98
2
2.02
2.04
2.06
Time [sec]

(c)

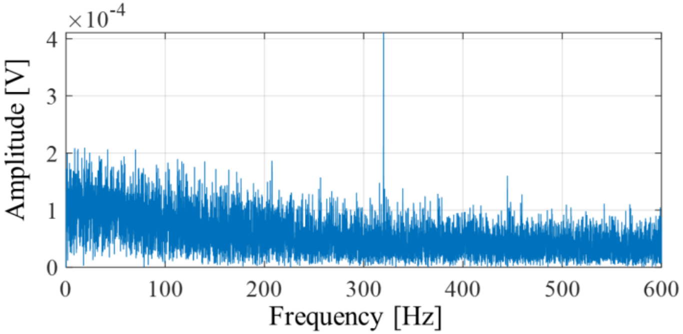
×10^-4
4
3
2
1
0
Amplitude [V]
0
100
200
300
400
500
600
Frequency [Hz]

(d)

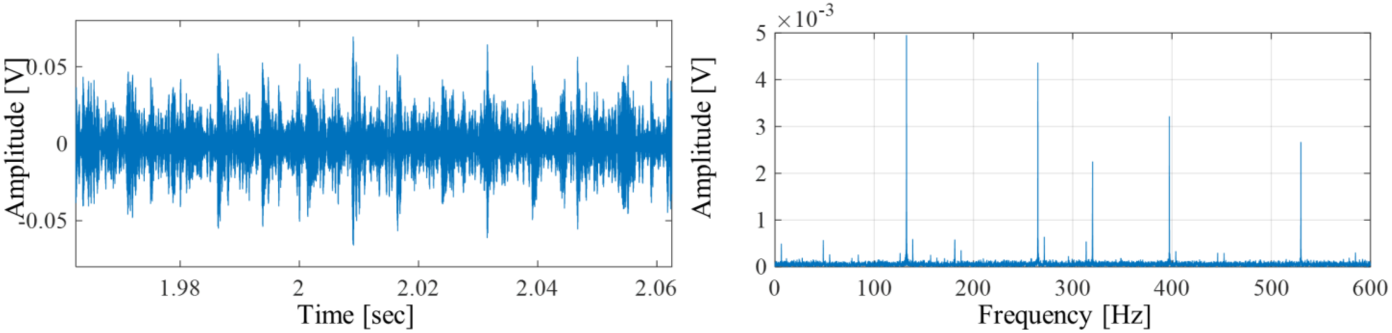

(c) (d)

Figure 4-15 Band-pass signals and envelope spectrums at the selected frequency band, as found by each band-selection method for the low-SNR simulated signal: (a), (b) Fast Kurtogram, (c), (d) Autogram, (e), (f) the proposed method.

Figure 4-16 shows the autocorrelation analysis of Autogram's results in the low-SNR simulated case. Unlike the good-SNR case shown in Figure 4-11, several different periodic components, unrelated to the bearing's fault, are observed in the lag domain. The main pattern seems to be repeated with an interval of about 400 data points, and it matches with the period of a 360 Hz component. Considering the input signal that has gone through the squared envelope analysis, Autogram method focuses on the motor-related noise, with 160Hz as the main component.

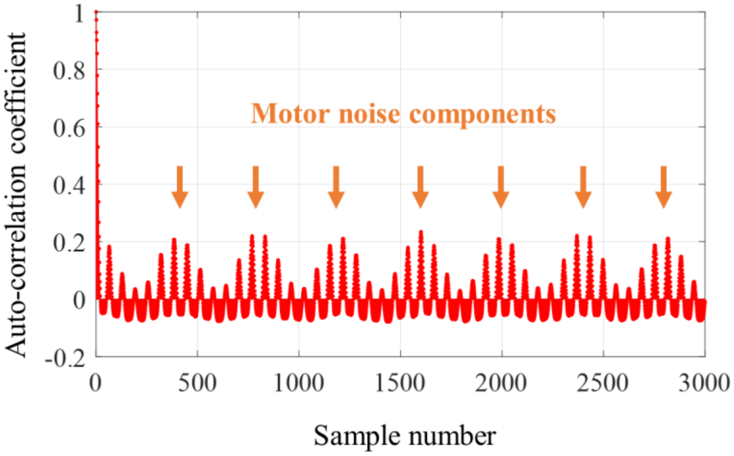

Figure 4-16 Autocorrelation function for the simulated signal filtered by the optimally selected band from Autogram, in the bad-SNR case.

Figure 4-17 illustrates a sequence of segment signals, $S_{k,l}$, for the frequency band selected by the proposed method in the low-SNR case. Although the overall segment signals have random fluctuations because of the low-SNR character, the periodic bearing's defect could be observed with the same phase. This indicates that the proposed method properly operates under noisy conditions.

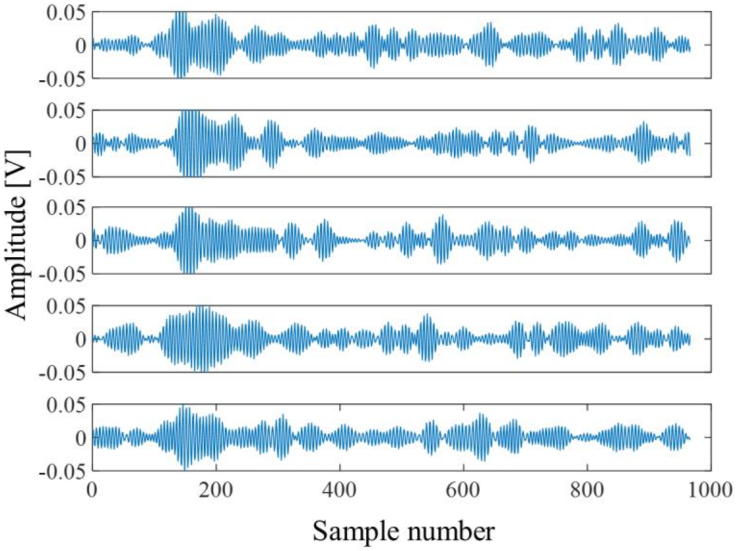

Figure 4-17 Sequence of segment signals ($S_{k,l}$) with index l=1~5 at the selected band for the simulated data in the low-SNR case.

Two additional simulation analyses have been conducted to demonstrate the behavior of both the traditional and proposed methods for the input signal's diverse circumstances. The additional studies differ in their noise conditions, considering the predominant components of impulsive and electrical noise, as shown in Equation (4.14). Two cases are considered: first, a case without electrical noise, x_{EMI}, and second, a case without impulsive noise, x_{in}. An identical process of signal processing and band selection is applied to both signals, as conducted for the previous simulated analysis. Figure 4-18 and Table 4-4 show the band selection results for the case without electrical noise components. The Fast Kurtogram approach failed to find the fault-related frequency band, as expected. On the other hand, Autogram and the proposed method worked successfully to find the bearing defect band around 24000 Hz. Figure 4-19 and Table 4-5 represent the results of the case without the impulsive noise component. In this case, Fast Kurtogram was barely able to find the proper band due to the high-frequency noise from the electrical components, as highlighted in decomposition level one. Autogram failed to find the proper band, as shown in Figure 4-14. Here, it seems that the absence of electrical noise allowed the successful searching of the Autogram approach. In other words, local periodicity of electrical components can disturb target defect searching. The proposed method works on both cases, which demonstrates its noise robustness for both noise components of impulsive and locally periodic noise.

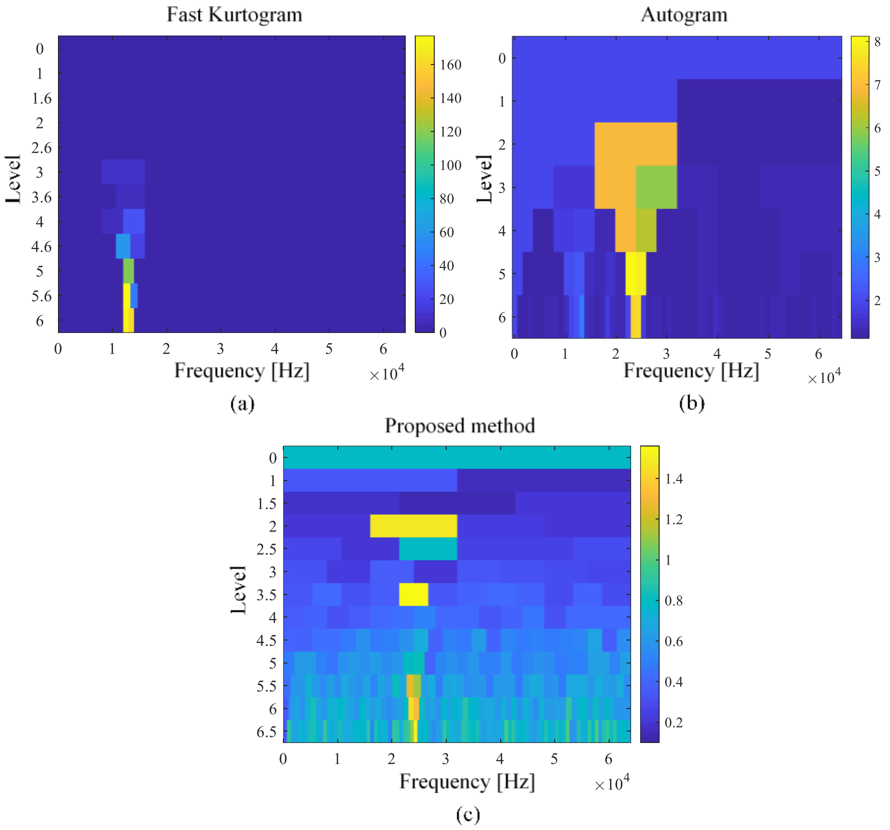

Figure 4-18 The results of each band selection algorithm for a simulated signal in a low-SNR situation without electrical noise components: (a) Fast Kurtogram, (b) Autogram, and (c) the proposed method.

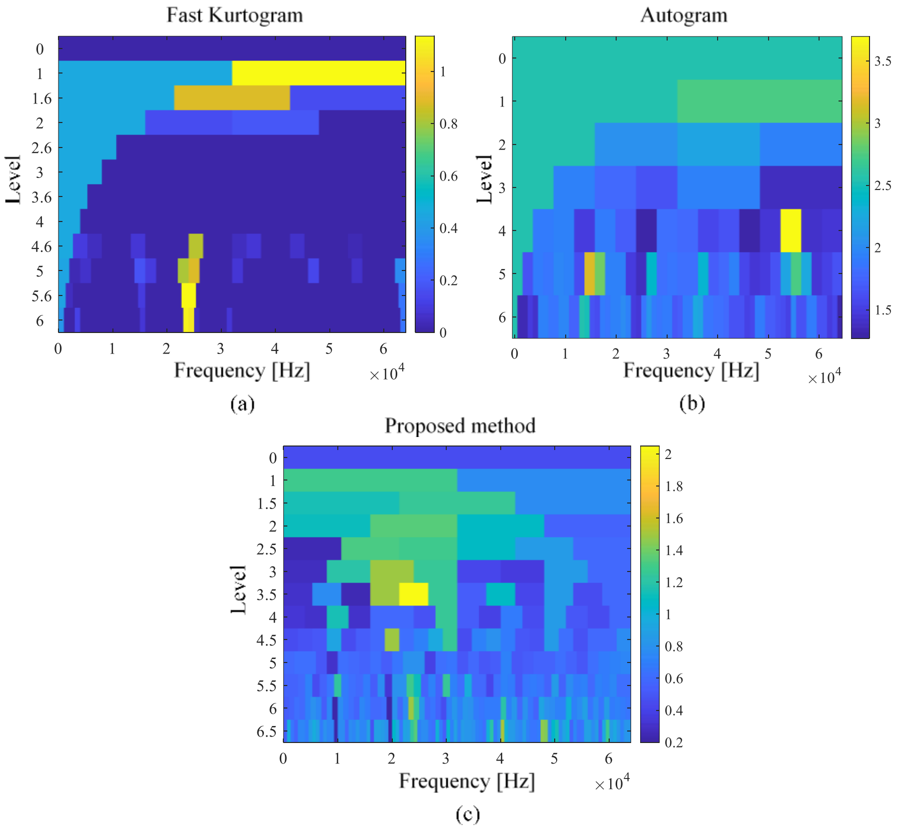

(a)

(b)

(c)

Figure 4-19 The results of each band selection algorithm for a simulated signal in a low-SNR case without an impulsive noise component: (a) Fast Kurtogram, (b) Autogram, and (c) the proposed method.

Table 4-4. The results of band-selection for simulated data in a low-SNR case without electrical noise components.

	Fast Kurtogram	Autogram	Proposed method
Level	5.5	5	3.5
Frequency center [Hz]	12667	23000	24000
Bandwidth [Hz]	1333	2000	5333

Table 4-5. The results of band-selection for simulated data in a low-SNR case without an impulsive noise component.

	Fast Kurtogram	Autogram	Proposed method
Level	5.5	4	3.5
Frequency center [Hz]	24667	54000	24000
Bandwidth [Hz]	1333	4000	5333

4.4 Experimental Validation of the Proposed Method

This section demonstrates the proposed band selection method using experimental data from a bearing test rig in the laboratory. The test rig is set up for health monitoring of a slewing bearing used for the yawing system in heavy machinery, as mentioned in Section 3.2. Heavy machinery's large stiffness and low operating speed create the need for an AE sensor to measure it over long-time-period observations to trace the periodicity sensitively. The long-time measuring easily exposes the AE signal to impulsive and periodic non-Gaussian noise. The experimental data acquisition and description through the test rig are presented in Section 4.4.1. The proposed method is applied to the measured data, and the results are compared with the traditional Fast Kurtogram, and Autogram approaches in Section 4.4.2.

4.4.1 Experimental Data Acquisition and Description

Slewing bearing test data set is measured through constructed testbed in Section 3.2. The detailed parameters of the data acquisition are listed in Table 4-6.

Table 4-6. Detailed parameters for slewing bearing data acquisition.

Parameter	Values
Sampling rate	100000 sample/s
Sample time	60 sec
Axial load	10 tf (10^4 kgf)
Rotating speed of the shaft	15 rpm

Figure 4-20 shows the time and frequency domain plot for the measured AE signal. Several local impulsive peaks are observed on the time-series data in Figure 4-20(a); these seem to be generated from the bearing's defect, but this is uncertain because of the noise. The spectrum of the raw signal in Figure 4-20(b) shows that the signal is highly smeared by the electrical noise. 60Hz and its harmonics are the main supplying current frequency in a single phase, and 30Hz and its harmonics are the electrical frequency of the motor at 15RPM with a 1/60 reduction gear ratio.

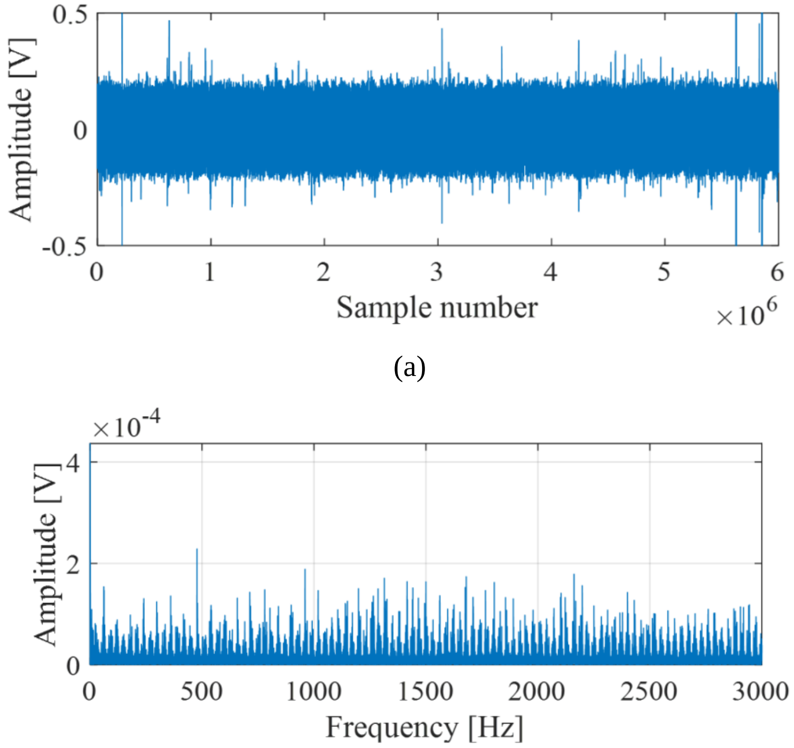

(a)

(b)

Figure 4-20 Measured AE signal: (a) time-domain signal, and (b) spectrum.

4.4.2 The Results for Experimental Validation

The proposed method for band selection is applied to the experimental data. The performance of the proposed method is compared with the traditional methods in the same manner as described in Section 4.3. Figure 4-21 illustrates the results of the Kurtogram method, Autogram, and the proposed method. The details of the selected band for each method are listed in Table 4-7. Algorithms other than the proposed method select a band around 19,000Hz, while the proposed method selects 6,250Hz.

Figure 4-22 shows the envelope spectrum of the selected band for each method. Figures 4-20 (a) and (b) show similar spectrum results with many harmonic peaks of 60Hz, which is the main electric power supplying frequency. In addition, between those harmonic components, several minor peaks appear with an interval of 30 Hz, which is the electrical frequency of the motor at 15RPM with a 1/60 reducer. Figure 4-22(c) also shows the peaks of the electrical components, however, they are less dominant. In contrast, Figure 4-22(c) shows a number of peaks in the low-frequency region under 100Hz. Those peaks are the harmonics of 4.79Hz, the characteristic defect frequency of the target slewing bearing, which can be calculated using the general equation for defect frequency calculation [35]. The detailed geometry parameters are as follows: there are 39 rolling ball elements, ball diameter is 20mm, pitch diameter is 280mm, and the approximate contact angle is 75 degrees. Judging from the results of the spectrum, the proposed method can extract objective defect signals, unlike the Fast Kurtogram and Autogram methods, which focus on the electrical components.

Table 4-7. The results of band-selection for the experimental data.

	Fast Kurtogram	Autogram	Proposed method
Level	6	5	3.5
Frequency center [Hz]	19141	19531	6250
Bandwidth [Hz]	781	1563	4167

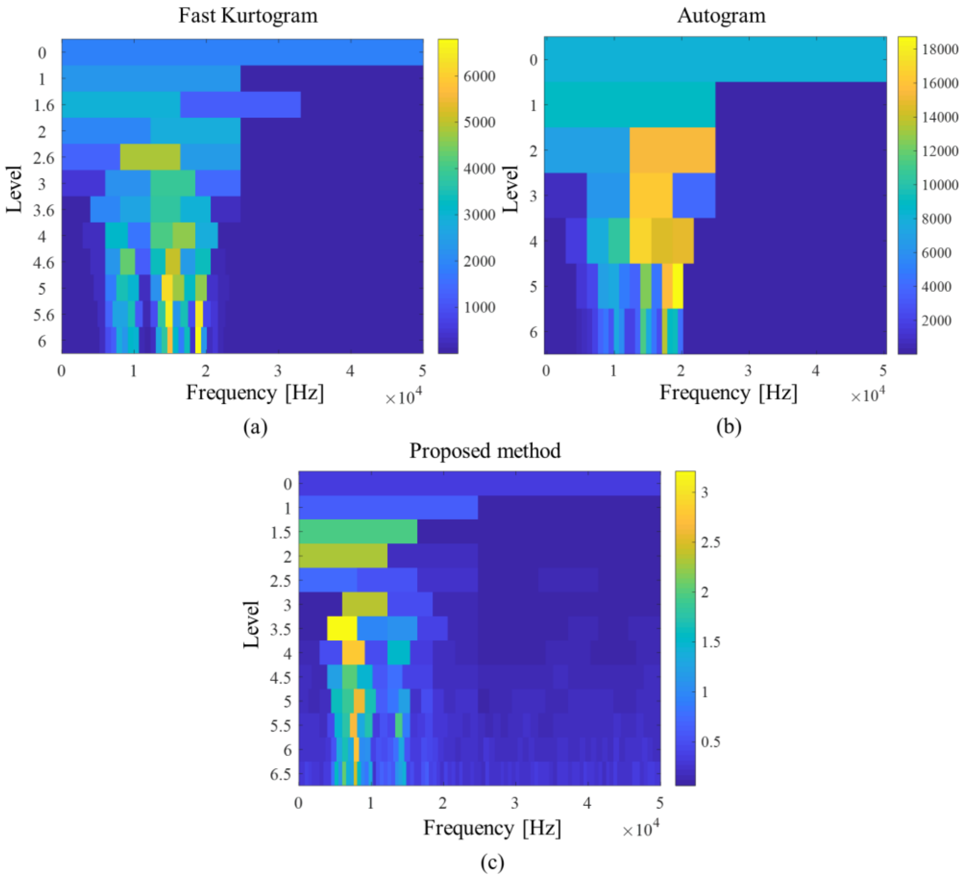

(a)

(b)

(c)

Figure 4-21 The results of each band selection algorithm for the experimental data: (a) Fast Kurtogram, (b) Autogram, and (c) the proposed method.

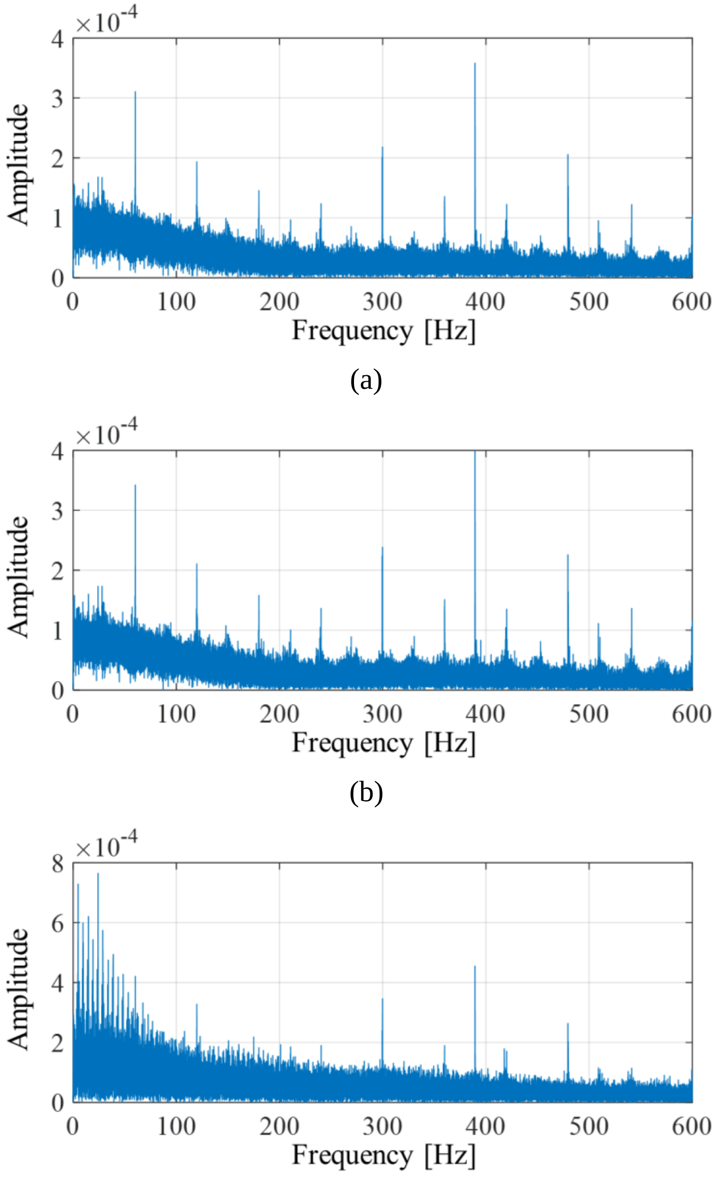

(a)

(b)

(c)

Figure 4-22 Envelope spectrums of the selected frequency band for each method: (a) Fast Kurtogram, (b) Autogram, and (c) the proposed method.

Figure 4-23 shows the autocorrelation analysis of Autogram's results for the slewing bearing data. Many peaks in the lag domain contain motor noise and target defect components. It seems that the motor noise, corresponding to 60, 30 Hz and their harmonics, is predominant, as compared to the defect. The periodic motor noises disturb the distribution of the ACF, which can increase Equation (4.4) by selecting a band irrelevant to the target defect. In addition, the low SNR of the measured signal results in low correlation of the defect components, which makes Autogram vulnerable to periodic noise.

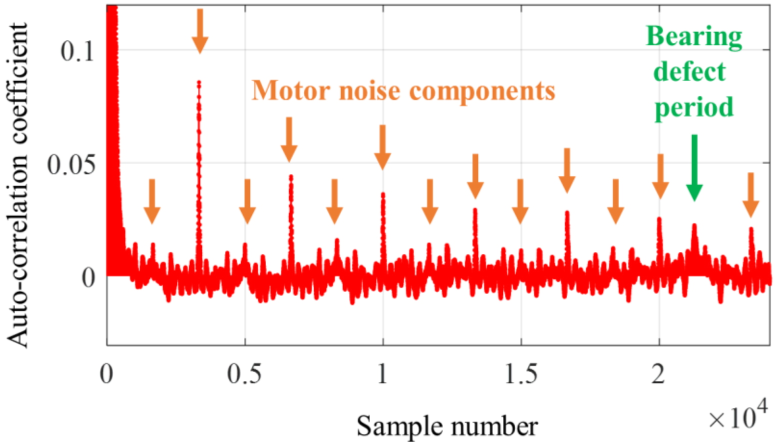

Figure 4-23 Autocorrelation function for the slewing bearing signal filtered by the optimally selected band from Autogram.

Figure 4-24 shows a sequence of segmented signals, $S_{k,l}$, at the selected frequency band of the proposed method. A similar impulsive pattern is observed in the latter part of every segment. Even though the nonlinearity of the bearing system might cause a slight phase discrepancy along the segments, the local phases match. Local phase matching increases the correlation score of the defect measure in Equation.

(4.12); this it means that the proposed band selection method successfully selects the band related to the target fault.

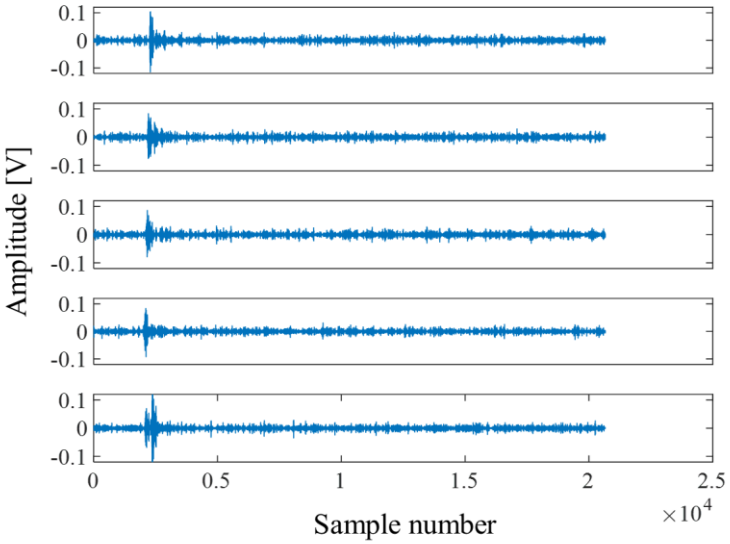

Figure 4-24 Sequence of segment signals ($S_{k,l}$) with index l=1~5 at the selected band for the experimental data.

Figure 4-25 compares the computing times for the experimental data, as described in Section 4.3.2. The experimental data has a large number of samples because of the long sampling time and slow periodicity. Although the relatively large samples increase the average computing times, the trend among methods is similar to the results of the simulation data; this is shown in Figure 4-25. Each box plot has 50 samples of cost times for the experimental data. Fast Kurtogram approach takes the shortest time, around 10 seconds, and Autogram method takes the longest time, around 450 seconds on average. Autogram's high computing cost comes from the wavelet packet decomposition step, which could take more time as the decomposition level increases. The proposed method is faster than Autogram by about 4.5 times.

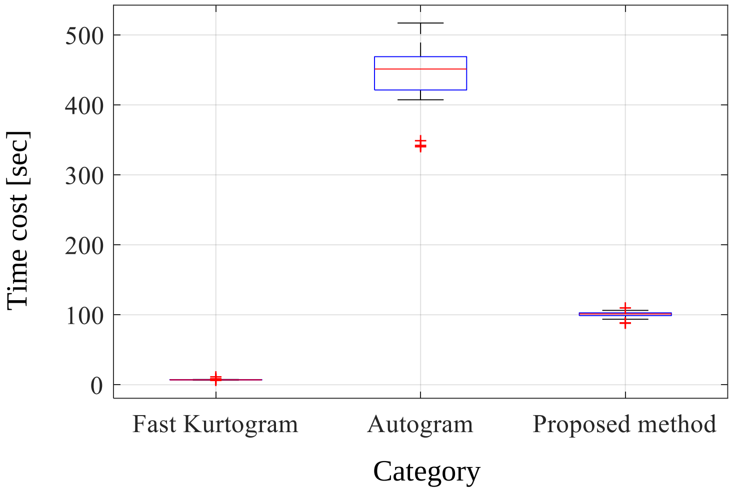

Figure 4-25 Comparison of calculation time for each method.

For further verification, an additional experiment has been carried out with different operating speed conditions. Figure 4-26 and Table 4-8 show the band selection results for each method with 10 RPM of shaft rotation. A decrease of rotating speed causes an energy drop in the defect signal, resulting in a low SNR of the measured data. As a result, Fast Kurtogram and Autogram approaches fail to find the detailed fault frequency band. Although Figures 4-26(a) and (b) show a faint highlight at around 8kHz in both methods, macroscopic noise of the raw signal is sufficient to distract the objective function of the traditional algorithm. The proposed method, meanwhile, selects a frequency band around 6.5kHz, a similar center frequency as that of the 15RPM case shown in Table 4-7. These experimental results and the simulated validation in Section 4.2 show the potential ability of the proposed algorithm, even in a low-SNR condition. These results show the superiority and high-sensitivity of the proposed method, as compared to the traditional methods. Furthermore, it demonstrates the effectiveness of the proposed segment-based defect measure in Equation (4.12), as a noise-robust factor that considers impulsive and non-Gaussian periodic noise.

Table 4-8. The results of band selection for the experimental data for the 10RPM condition.

	Fast Kurtogram	Autogram	Proposed method
Level	0	0	6.5
Frequency center [Hz]	25000	25000	6510
Bandwidth [Hz]	50000	50000	521

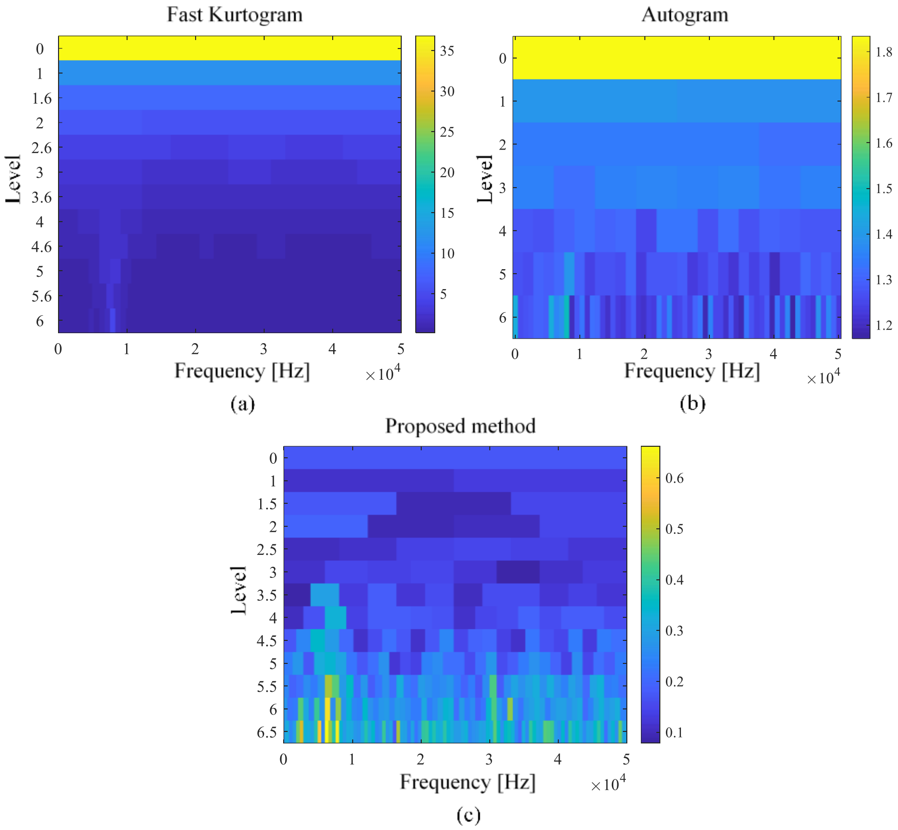

(a)

(b)

(c)

Figure 4-26 The results of each band-selection algorithm for the experimental data for the 10RPM condition: (a) Fast Kurtogram, (b) Autogram, and (c) the proposed method.

4.5 Summary and Discussion

This study proposes the design of a noise-robust and efficient band-selection method for AE sensor data. The proposed correlation- and kurtosis-based measure makes the selected band focus on the periodic and impulsive characteristics of the bearing defect. Its features prevent the proposed method from being deceived by external impulsive or periodic non-Gaussian noise. The proposed method is verified by applying it to both simulated and experimental data; the results are compared to traditional band-selection methods. The suggested method has several advantages. First, by using the target defect period, it can search for the optimum defect band quickly, despite a large amount of data in noisy conditions. Second, the suggested method can be applied not only to an AE sensor but also to other sensors with a high sampling rate, such as ultrasound and ultra-high frequency (UHF) sensors. Third, the proposed defect measure uses only time-domain signals without spectral reasoning, which reduces the computational burden and allows practical use in industry. Furthermore, the proposed method can also be applied to other rotary components that carry periodic defect signals.

Sections of this chapter have been published or submitted as the following journal articles:

1) **Su J. Kim**, Sungjong Kim, Seungyun Lee, Byeng D. Youn, and Taejin Kim, "Effective band-selection algorithm for rolling element bearing diagnosis using AE sensor data under noisy conditions," *Structural and Multidisciplinary Optimization*, Submitted.

Chapter 5

Motor-current-based Electromagnetic Interference De-noising

This chapter introduces the design of the de-noising filter eliminating the electrical components in AE signals. Among the electrical components, electromagnetic interference (EMI) becomes the main target of interrupting source, which is hard to separate from bearing signals because of the non-stationary and dynamic characters, despite optimum band selection. For successful extraction of bearing defect information, de-noising process that cancels out the defect-irrelevant components is required, as a preprocessing of diagnosis procedure. The detailed sections of this chapter are organized as follows. Section 5.1 briefly reviews the electromagnetic interference. Section 5.2 introduces the proposed de-noise filter algorithm for bearing fault detection. In section 5.3, the effectiveness of the proposed method is demonstrated using experimental data from a bearing test rig, and the experimental results are discussed. Finally, the last section provides a summary and discussion.

5.1 Electromagnetic Interference

This section explains the electromagnetic interference (EMI) to help understand the noise that the author focuses on in this dissertation. Electromagnetic interference (EMI) is the high-frequency signal that is generated by a variable frequency motor (VFM). For rotary machines, it is common to use a VFM to control the rotational speed [63]. The VFM controls the speed by adjusting the frequency of the supplied AC. Figure 5-1 shows a schematic diagram of speed control with a VFM, and the source of EMI.

The rectifier first converts the supplied AC to DC and then the inverter changes it back to AC, but with the desired frequency, f_e. However, when the inverter changes DC back to AC, the resulting AC is not a true AC signal, but rather the summation of discontinuous DCs. In other words, it only mimics AC with DC, using the method called pulse width modulation (PWM) [65]. In the PWM process, a carrier signal with a switching frequency slices the target AC signal and makes a particular on/off pattern in DC to simulate the target AC. This approximation accompanies complex modulation of the switching frequency that affects the current input of the motor, which is the major source of EMI. In detail, from a macroscopic view, the motor’s input is seen as continuous low-frequency waves. However, from a microscopic view, the input is a discrete signal based on the switching frequency of the inverter. This micro-discontinuity of the motor input results in the low-frequency modulation of the high-frequency switching components. Finally, electromagnetic force in the motor actualizes the EMI signal in the mechanical vibration on the system.

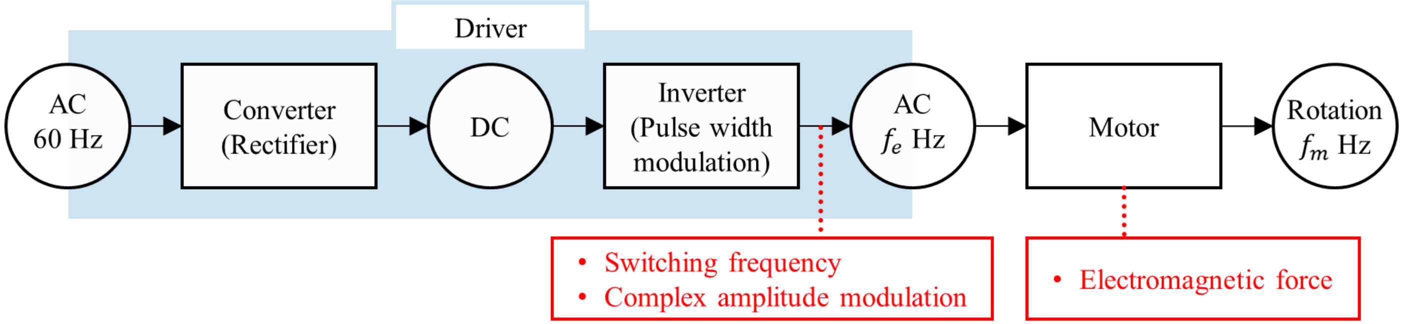

Figure 5-1 A schematic diagram of speed control with a VFM and the source of EMI.

There are several notable characteristics of EMI. First, EMI causes a lot of harmonics of the switching frequency. Inverter manufacturers usually set the switching frequency between 2 ~ 15 kHz [73]; however, the PWM output has harmonics up to the megahertz range. Another characteristic is the complicated modulation of PWM output involving the Bessel function [65]. The modulation signal creates sideband effects on the switching frequency with an interval of f_e. The electrical frequency f_e is related to the desired mechanical frequency f_m by Equation (5.1).

$$f_e[Hz] = \frac{P_p}{60} \times f_m[RPM] \tag{5.1}$$

where P_p is the number of pole pairs of the motor. This means that EMI is variable noise that depends on the shaft rotation speed and motor driver specifications. When the operating conditions change, EMI from the motor is also altered by spectral shifting.

Due to the previously mentioned characteristics, EMI disturbs the bearing diagnosis creating a large amount of noise in zone 4 of Figure 2-3, as well as in zone 2 when the signal is demodulated after envelope analysis. Since EMI comes from the operating motor, it is inevitable in a rotary system. When data is gathered from an AE sensor, the signal is even more affected by EMI because of its high sensitivity and broad operating frequency. As a result, the AE data has a low signal-to-noise ratio (SNR) due to the unwanted noise from the motor. It needs to distinguish bearing fault signals from EMI signals in the envelope spectral domain and remove unwanted ones. When there is enough information on the motor, driver, and bearing system, it is possible to distinguish the noise from the target signal. However, all the necessary information is not usually available. Further, even if it is available, it would still be arduous to filter out EMI that appears sporadically in the envelope spectrum. The proposed method, which is introduced in Section 5.2, assumes that the defect frequency is unknown; this is common in many cases because of unknown geometry or operating conditions. In this situation, many industrial solutions determine the abnormality of the bearing using physical and statistical measures of the envelope signal. The proposed method aids this problem by diminishing the EMI noise.

5.2 Multi-sensor-based EMI Filter Design

The fundamental concept proposed to eliminate the EMI from the AE sensor signal is explained in this section. Because EMI is generated in a high-frequency region, the proposed method is suitable for AE sensors that observe broadband information. The filter for the AE signal is designed using the current signal. To extract necessary information from different physical quantities, a series of signal processing methods are also introduced.

5.2.1 Framework of the Proposed Multi-sensor-based Filtering

The AE signal is readily corrupted by the EMI, resulting in unwanted peaks in the frequency domain that hinder the diagnosis of the bearing. This study aims to effectively eliminate these peaks in the frequency domain for better bearing diagnosis. The key idea of the proposed approach is to separate the defect signal from the electrical noise using two different sensors, as shown in Figure 5-2: first, an AE sensor is used, which contains both the bearing and the EMI signals, the second is the current sensor, which contains only the EMI signal.

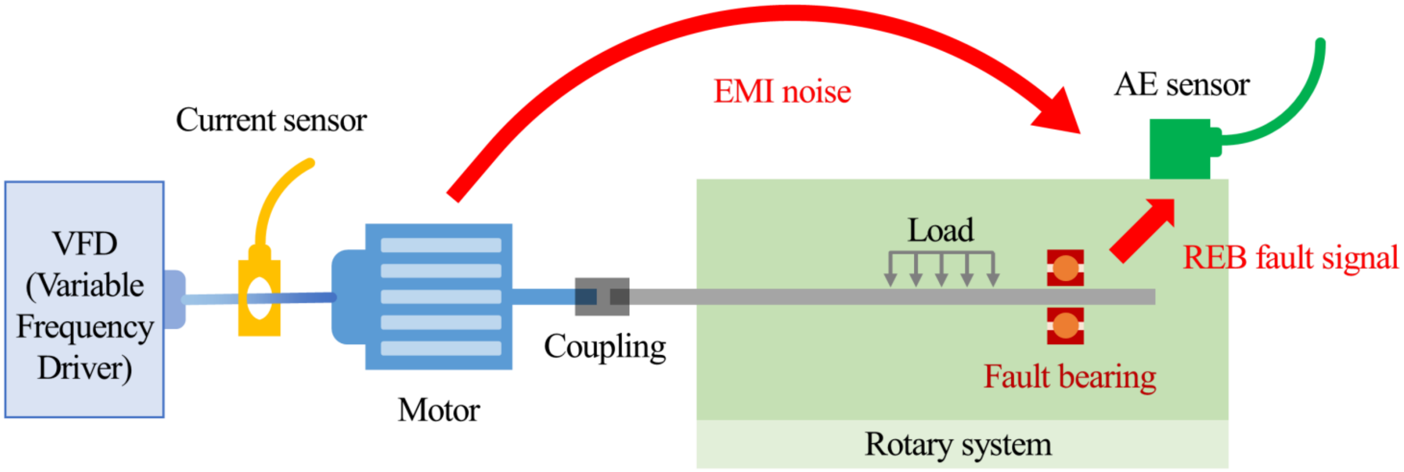

Figure 5-2 Key concept of the proposed multi-sensor approach.

Signals from the AE and current sensors can be expressed as follows.

$$X_{AE} = O_r + D_b + R_{AE} + E_{AE} + S_{AE} + N_{AE} \tag{5.2}$$

$$X_C = PS + E_C + S_C + N_C \tag{5.3}$$

where O_r is the operating signal related to the rotation of the shaft, D_b is the defect signal from the bearing, and R_{AE} is the system resonance from the AE sensor, which has relation to D_b with amplitude modulation, as shown in Figure 2-4. E and S represent the electromagnetic interference signals. S specifically means the switching frequency and harmonics. E is the modulation of S. The subscripts *AE* and *C* indicate that the signal is measured by the AE sensor and current sensor, respectively. PS is the signal related to the main power supply. Finally, N is the noise from the external components, unexpected signal disturbance, and intrinsic noise in the data acquisition system.

Although both E_{AE} and S_{AE} are electromagnetic interference terms, what particularly hinders bearing diagnosis is E_{AE}. When demodulating the defect signal (D_b) from the resonance signal (R_{AE}), E_{AE} is also demodulated from the switching frequency (S_{AE}) because all these signals are tangled together. As a result, E_{AE} generates a number of unwanted peaks in the envelope spectrum. To subtract the demodulated E_{AE} from the spectrum, the motor input current could be utilized because it is less correlated with bearing defects. Although E on both signals cannot be directly subtracted due to the physical difference, one can be inferred from the other using their correlation. To this end, this study suggests an adequate signal processing method for removing E_{AE}, including the empirical mode decomposition (EMD) and cumulative distribution function (CDF)-based filter design.

The overall process of the proposed method is shown in Figure 5-3. It begins with data acquisition through two sensors, an AE and a current sensor. The bearing signal from the AE sensor goes through typical preprocessing for bearing diagnosis, which is band-pass filtering. Band-pass filtering picks out the unintended frequency information N_{AE}, such as low-frequency noise and signals from other mechanical components. The current signal also goes through preprocessing, but the EMD method is used for robust extraction of E_C and S_C, instead of using the band-pass filter. Then, envelope spectrum analysis is adopted for both preprocessed signals to demodulate the high-frequency carrier signals R_{AE}, S_{AE}, and S_C. After that, an adequate filter is designed by using the envelope spectrum of E_C, using a probabilistic approach. Finally, EMI on the envelope spectrum of E_{AE} is filtered by the predesigned filter. The result of the process, the de-noised envelope spectrum can then be utilized for REB fault diagnosis.

Two steps are of primary importance in the suggested process. One is the use of EMD to separate the EMI from the current signal; the other is the design of the CDF filter to cancel out the correlated noise components between the different sensors. Details of these steps will be described in the following sections.

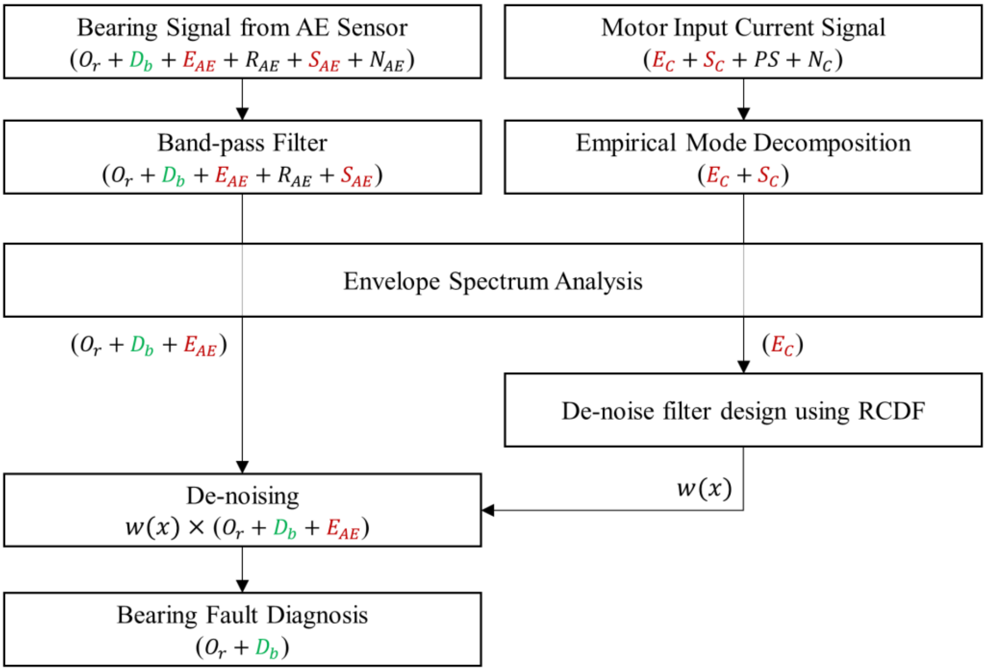

Figure 5-3 Flowchart of EMI filter design.

5.2.2 EMI Signal Extraction using Empirical Mode Decomposition

As described in the previous section, the motor input current signal is used to eliminate high-frequency EMI from the AE signal. For this purpose, the EMI-related signal is first extracted from the current data. This requires an adaptive algorithm for the following reasons. First, switching and electrical frequency information are not readily available in industry settings without the manufacturer's support or experimental reasoning. This lack of information makes it difficult to figure out the EMI. Second, even if all of the necessary information is available, it is cumbersome to manually adjust the parameters of the EMI extractor whenever the inverter specifications change. Third, the variable speed of the motor changes the modulation frequency, which leads to a change in the EMI peaks in the spectrum. Finally, a variable switching frequency technique was recently developed in motor control to reduce the switching loss, making an ever-changing EMI. Considering these points, empirical mode decomposition (EMD) is employed to adaptively extract the interference signal. This technique is developed to interpret nonlinear and non-stationary signals [74], [75]. The EMD method decomposes the raw signal into several other signals, like the Fourier series. One of the strengths of EMD is its adaptability in decomposing the original signal into periodic components. This method assumes that the original signal, $y(t)$, is a superposition of several periodic components, called the intrinsic mode function (IMF), expressed as

$$y(t) = \sum_{i=1}^{k} IMF_i(t) + r_k(t) \tag{5.4}$$

where the $r_k(t)$ is the residual signal of $IMF_k(t)$. The method iteratively decomposes the original signal into IMFs; each iteration is called 'sifting'. After the first sifting, the first main cyclic component, $IMF_1(t)$, is found and subtracted from the original signal, and the residual, $r_1(t)$, is designated as the target signal for the subsequent sifting.

During the sifting process, the average of the upper and lower envelope is iteratively subtracted from the given signal. The IMF is determined when the residual satisfies two criteria. First, the difference between the number of local extremes and the zero-crossing of the residual is zero or one. Second, the sum of the local maximum and minimum is zero. Satisfaction of these two criteria allows effective decomposition of an amplitude-modulated, non-stationary signal like EMI. In particular, the first property makes each IMF have different frequency characteristics. The earlier the IMF is extracted, the higher frequency the IMF contains. While power supply and sensor noise are commonly found in low-frequency regions, the EMI includes relatively high-frequency components. Based on the IMF's frequency characteristics, the lower order of the IMF signal is more likely to extract the EMI as it withdraws unwanted signals.

Note that although the frequency tends to decrease as the order of IMFs increases, it is not deterministic like frequency-based decomposition. IMFs are not globally orthogonal, they are locally orthogonal by frequency overlapping between neighboring IMFs. Despite this vagueness in decomposition, EMD has an advantage over frequency-based decomposition. EMD can sequentially extract the main periodic components from any given signal without knowing the characteristics of it. In the current signal, the switching frequency and its modulation lie in the high-frequency region; however, the specific region depends on the system and operating conditions. EMD can adaptively extract the high frequency of a given signal without prior knowledge of the system. Its flexible separation makes it easy for it to extract the high-frequency EMI.

5.2.3 De-noising Filter Design with a Cumulative Distribution Function

As mentioned in Section 5.2.1, in the envelope spectrum of the AE data, the demodulated EMI coexists with the bearing fault signal. To remove the EMI components selectively, a proper filter needs to be designed. There are some well-known traditional filters, such as zero-passing, band-pass, and notch filters. These filters, however, have the drawback of eliminating the multiple peaks from EMI. Although a zero-passing filter could directly remove unwanted energy in the frequency domain, it needs to adjust the filtering parameter manually. Band-pass and notch filters could eliminate narrowband information, but they bring spectral distortion around the target band. Repetitive filtering for multi-peak de-noising could disturb the bearing’s defect signal. Furthermore, the high sampling rate of AE data requires a high-order function for designing the filter. The filter's response shape needs to be extremely sharp because the frequency scope of the target noise is too small, as compared to the entire spectral domain. This is not only computationally burdensome; it also increases the time cost.

For this reason, we need an effective filter that removes only EMI components without touching the bearing fault. In this study, a probabilistic approach is adopted in the diagnosis space. The filter design procedure consists of four steps, as depicted in Figure 5-4.

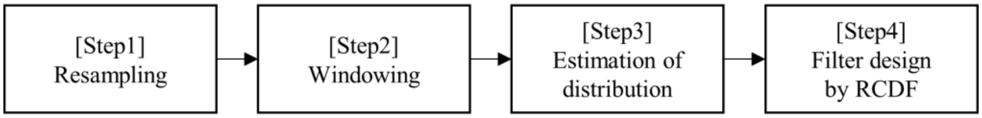

Figure 5-4 Procedure of de-noising filter design.

Step 1. Resampling. If two sensors' acquisition times are different, their frequency resolution in the positive real spectrum will not match each other. This causes grid discrepancy in the frequency plane during filtering. The longer the acquisition time, the higher the frequency resolution, regardless of the sampling rate. Thus, the two target signals with different frequency resolutions require a resampling process to adjust them. In order to prevent information loss, it is recommended to oversample, according to a relatively higher resolution signal.

Step 2. Windowing. Since the two signals have different sampling rates, the observed frequency ranges are also different. Therefore, each envelope spectrum should be truncated to match the end. In this operation, the window size is a control parameter. If the range is too broad, (e.g., DC up to 100 kHz), too many peaks might be gathered, including the remaining switching frequency. This makes it difficult for the filter to focus on the demodulated signal in zone 2. On the other hand, when the range is too narrow, some information in the demodulated signal could be lost. A proper window size needs to be selected, excluding the switching frequency and including the demodulated signal. The recommended window size is between 2k and 5k.

<u>Step 3. Estimation of distribution.</u> The processed AE data has peaks from both the bearing data and EMI; the processed current data has only EMI peaks. However, direct subtraction of these two signals cannot remove EMI from the AE data because of the scale difference. Hence, normalization is required. The problem is that the scale difference varies for each peak; thus, collective correction (e.g., multiplying the normalizing factor to a signal) will not work. Here a probabilistic filter will be designed to overcome this problem in step 4. As a preliminary step, probability distribution fitting for each signal is required. The amplitude of each of the grid points in the windowed current spectrum becomes a random variable of distribution. Various methods are available for distribution selection and parameter estimation. In the study, maximum log-likelihood estimation is used because of its simplicity. The equation is shown in Equation (5.5).

$$\underset{\boldsymbol{\theta}_j, j}{\arg\max} E(\boldsymbol{\theta}_j) = \prod_i p_j(x_i|\boldsymbol{\theta}_j) \tag{5.5}$$

where x_i is spectrum amplitude of the ith index, $p_j(\cdot)$ is the jth probability distribution function from the candidates, and $\boldsymbol{\theta}_j$ represents the parameters of probability distribution $p_j(\cdot)$. The probability distribution and its parameters are obtained by maximizing Equation (5.5).

<u>Step 4. Filter design by RCDF.</u> An EMI reduction filter is developed using the estimated probability distribution. The filter's response function is made by weighting, through the reverse cumulative distribution function (RCDF). It is represented as

$$w_i = 1 - F_X(x_i) \tag{5.6}$$

where $F_X(x)$ is the cumulative distribution function (CDF) from the group of amplitudes. The parameter of the distribution is estimated in step 3. Equation (5.6) substitutes the filter's response weight w for the amplitude of the ith frequency index. It applies to all grid samples in the truncated envelope spectrum. Demodulated EMI generates a multi-peak situation in the windowed envelope spectrum; these have a locally large amplitude. The $a(x)$ values corresponding to the multi-peak of EMI are computed as almost zero through RCDF. The zero weight results in an energy decline at those grid points during the filtering process. Employing this property, the array of weight becomes a filter's response function, which can remove the overall multi-peak situation at once. Finally, the designed filter is multiplied by the AE data that is preprocessed by step 2, as shown in Equation (5.7).

$$O_r + D_b = w \times (O_r + D_b + E_{AE}) \tag{5.7}$$

The filtering process is performed on the envelope spectrum domain with element-wise products. In the preprocessed AE signal, E_{AE} exists in the form of a demodulated multi-peak. Through the equation, it can be removed selectively.

5.3 Experimental Validation of the Proposed Method

This section demonstrates the proposed de-noise method using experimental data from a bearing test rig in the laboratory. The resource for experimental validation of this thrust is the angular ball bearing test rig, as aforementioned in Section 3.1. The test rig is set up for health monitoring of angular ball bearing used in precision machining such as spindle module in CNC machine. In a precision machining process, the abnormality of the bearing must be detected as soon as possible. Because precision machining generally has high-rotational speeds, tiny bearing defects can cause a critical effect on the machining process and human safety in a moment. In this process, high-speed operation entails a large amount of motor noise for speed control, and it disturbs AE signals on bearing diagnosis. The brief contents of this section are as follows. The experimental data acquisition through the test rig is presented in Section 5.3.1, and the data description and the detailed analysis of measured data are presented in 5.3.2. In Section 5.3.3, the proposed de-noising process is applied to the measured dataset, and the results are analyzed. Lastly, the additional experimental verifications are proceeded with containing comparison study with traditional methods and quantified result analysis, in Section 5.3.4.

5.3.1 Experimental Data Acquisition

Angular ball bearing test data set is measured through constructed testbed in Section 3.1. A current sensor is additionally used for proposed multi-sensor filtering. The current sensor from Tektronix is clamped on the line between the driver and motor to measure the motor input current, as shown in Figure 5-5. An A/D converter, model 9239 from National Instruments, converts the analog sensor signal to the digital form of current data. The module has a maximum sampling rate of 50kS/s per channel and offers 24-bit digital resolution. The experimental dataset is obtained under the conditions designated in Table 5-1.

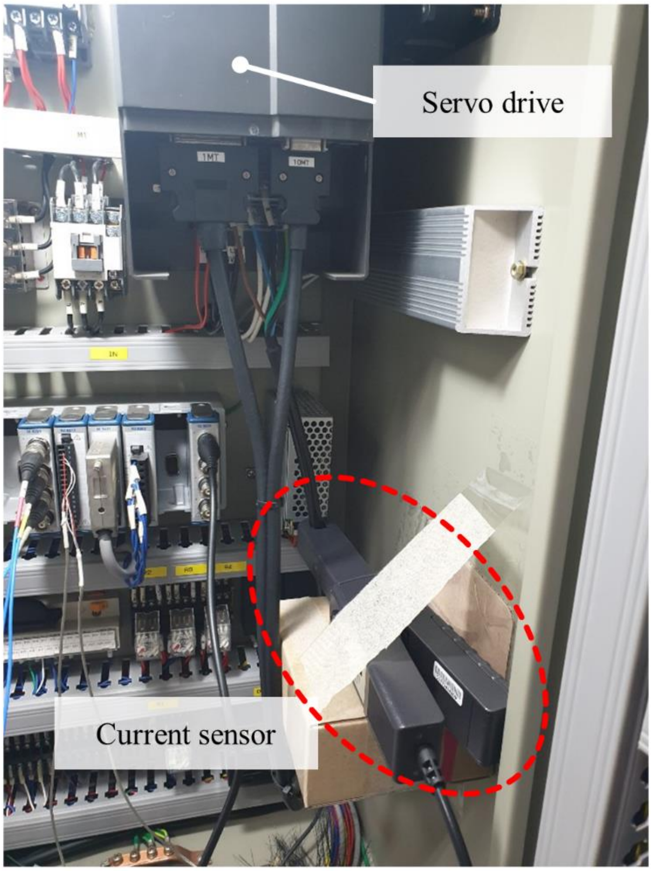

Figure 5-5 Configuration of the current signal acquisition.

Table 5-1. Data acquisition and experimental conditions.

Parameter	Values	
Basic load rating	8650 N	
Dynamic equivalent radial load	27 %	
Rotational speed	2100 RPM	
Number of motor poles	8	
Inverter switching frequency	10000 Hz	
Sensors	AE sensor	Current Sensor
Model (Maker)	WSa (Mistras)	A622 (Tektronix)
Sampling frequency	2 MHz	50 kHz
Sampling time	1 sec	1 sec

5.3.2 Description and Interpretation of Measured Data

The sampled raw signal from the AE sensor is shown in Figure 5-6(a). Some features of the bearing are observed from the raw data. Figure 5-6(b) expands the signal with the period of the BPFI and its multiples. The figure shows the impact signals, which are indicated by the red arrow. Some defect signals that have enough energy that they can be distinguished from the noise; however, some cannot. If the severity of the defect is insignificant or operating speed decreases, the entire impulse train will be buried in the background noise, making it impossible to diagnose the fault. This background noise could result from various sources. One of the main problems is the EMI, as mentioned in section 2.2. Figure 5-6(c) shows the expanded signal along the switching period and its multiples. This figure shows the repeated signal pattern of the EMI. The cyclic signal does not look like a simple sinusoidal signal; rather, it is a complicated signal superposed by the harmonics of the switching frequency and chaotic modulation. This EMI noise is measured along with the bearing signal, lowering the SNR.

Figure 5-7(a) shows the spectrum of the AE signal. The effect of EMI is observed in the form of vertical peaks. The pile of peaks consists of the harmonics of the switching frequency and the sideband generated by VFD. Figure 5-7(b) shows the expanded sideband around the 16th harmonic of the switching frequency, which has abundant spectral peaks. The spectrum shapes, the side bands around the harmonic in the figure, are repeated in almost every harmonic of the switching frequency involving an amplitude difference, according to the component energy. The green circle indicates S_{AE}, the harmonic of the switching frequency. There are multiple sideband which indicate E_{AE} in Equation (5.2). E_{AE} can be categorized into two

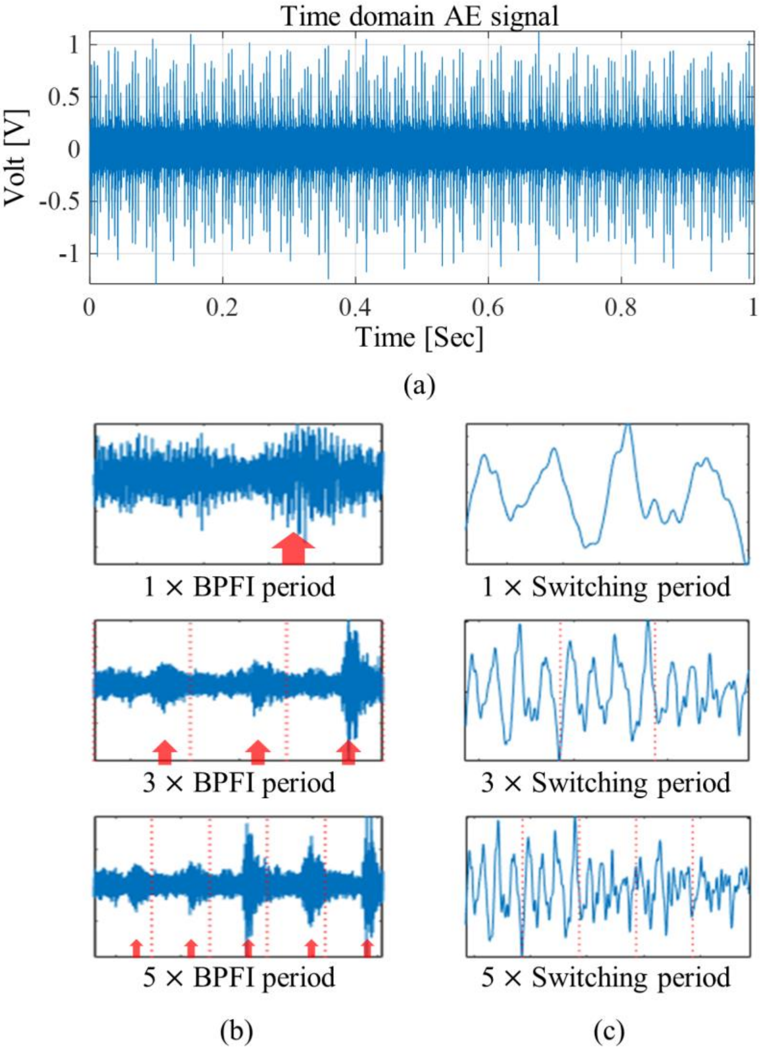

Figure 5-6 Time-domain signal of an AE sensor with a faulty bearing: (a) raw signal, (b) BPFI period signal, and (c) switching period signal.

groups, which are designated by the red triangles and blue diamonds in the figure. The first group, denoted by the red triangles, is related to the driving frequency of the motor. In this experiment, the driving frequency is set to 2100 RPM; however, the actual speed measured by the encoder is approximately 2081 RPM because of the open-loop speed control with frictional torque. The electrical frequency is approximately 138.7 Hz. It seems that the electrical frequency of the motor is the main component of modulation because it is prominent across the spectrum. The second group, denoted by the blue diamonds, is related to the power supply of the motor system. This group contains 360 Hz interval peaks around the switching frequency. Additionally, there are 60 Hz interval peaks around the switching and electrical frequencies. In Korea, 60 Hz is the fundamental AC frequency, and 360 Hz is the pulse frequency of a full-wave rectifier with three-phase power, based on 60 Hz AC. Thus, it seems that the electrical frequency and AC power are also in modulation because of the 60 Hz interval sideband found in the electrical frequency sideband component. These two groups’ sideband information will be transformed to the noise peaks in the envelope spectrum domain for bearing diagnosis.

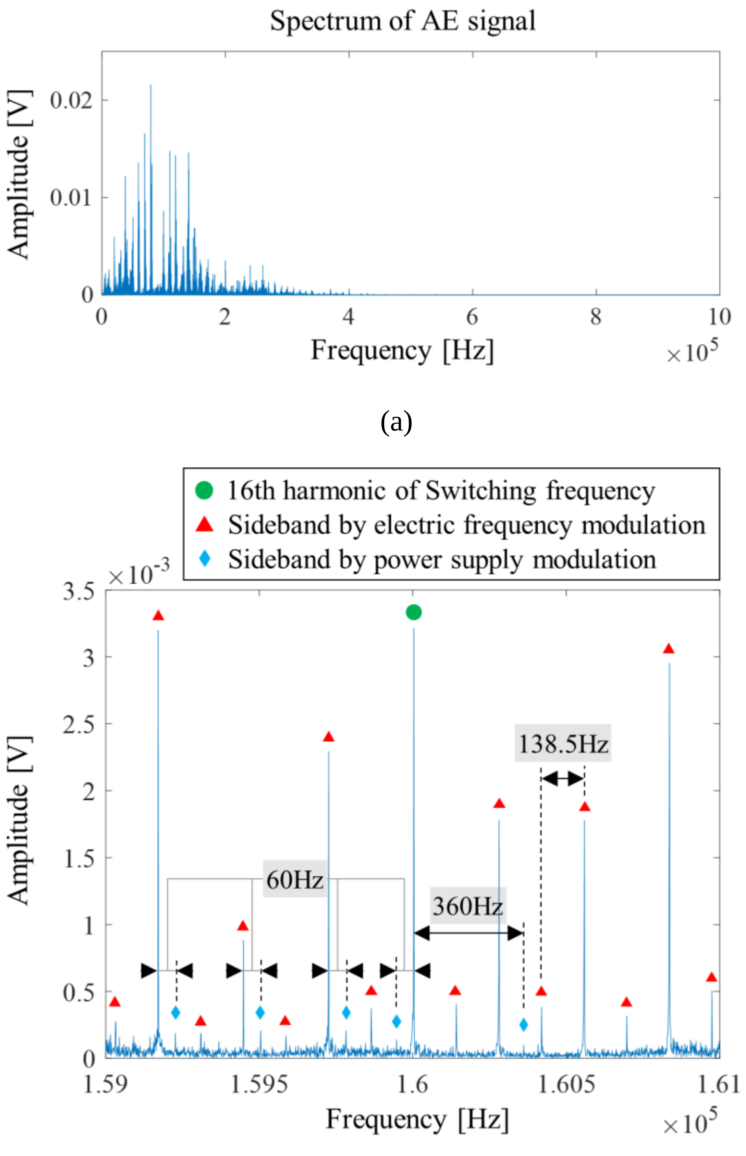

(a)

(b)

Figure 5-7 Spectrum of the AE signal with a faulty bearing: (a) total AE spectrum, (b) extended local AE spectrum of the 16th harmonics of the switching frequency.

The time-domain signal of the current data is shown in Figure 5-8(a). Figure 5-8(b) represents an enlarged time-domain signal with the electric driving period. The signal is repeated with the electric driving cycle; however, each cycle is different because of the superposition of the amplitude modulation signal from the PWM. Figure 5-8(c) is an expanded raw current signal along the inverter’s switching period and its multiples. Although it is not sinusoidal, the cyclic feature is clearly identified. The cyclic shape looks like a saw blade or train of the impulse signal; this is caused by the discrete operation of the inverting process. This means that the motor current input contains a PWM output, which justifies the direct extraction of EMI from the current signal.

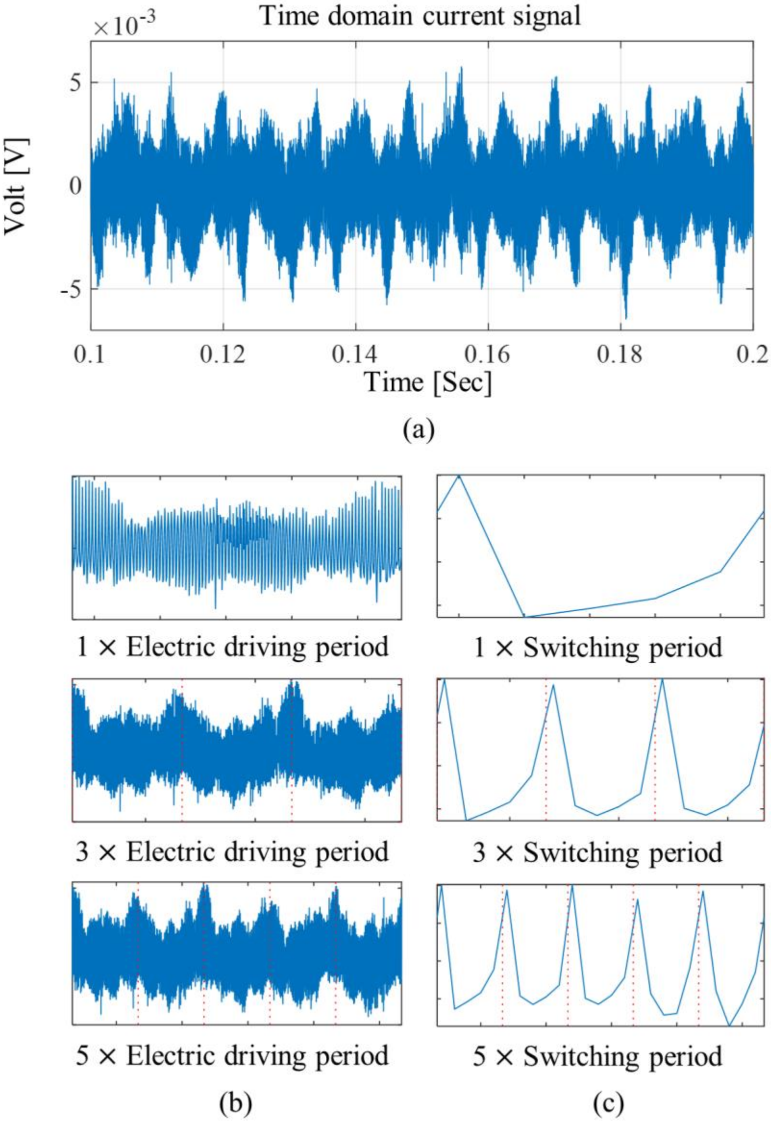

Figure 5-8 Time-domain signal of the current sensor: (a) raw signal, (b) electric driving period signal, and (c) switching period signal.

The spectrum of the current data is depicted in Figure 5-9. The total spectrum of the current data can be divided into three parts, as shown in Figure 5-9(a). Under the 2 kHz situation, the first part mainly has information about the power supply frequency, electric driving frequency, and other interference terms. The second part, around 1×10^4 Hz, has the switching frequency and sidebands that result from amplitude modulation. The last part, around 2×10^4 Hz, is the harmonic of the second part. The extended local spectrum of the second and third parts are similar. Figure 5-9(b) shows the extended spectrum of the second part. The green circle in the middle indicates S_C in Equation (5.3), and the other sideband peaks are E_C. Similar to the AE spectrum in Figure 5-7(b), the sideband peaks can be classified into two groups: electric driving and power supply, as marked by the red triangles and blue diamonds, respectively. It is important to note that additional peaks of the power supply with 120 Hz intervals appear. 120 Hz is the pulse frequency of a full-wave rectifier with single-phase power, based on 60 Hz AC. The three-phase power is a superposition of three single-phase sources with a phase shift of 120 degrees from each other. 120 Hz interval peaks are presumed to occur because the entire three-phase power cable is clamped by a current sensor when measuring data. Also, a 60 Hz sideband in the electric frequency is rarely found; this might be because the electric frequency signal is relatively weak, as compared to the AE case. The main difference with the AE spectrum is that the AE sensor mainly catches the electric driving frequency, while the current focuses on both groups.

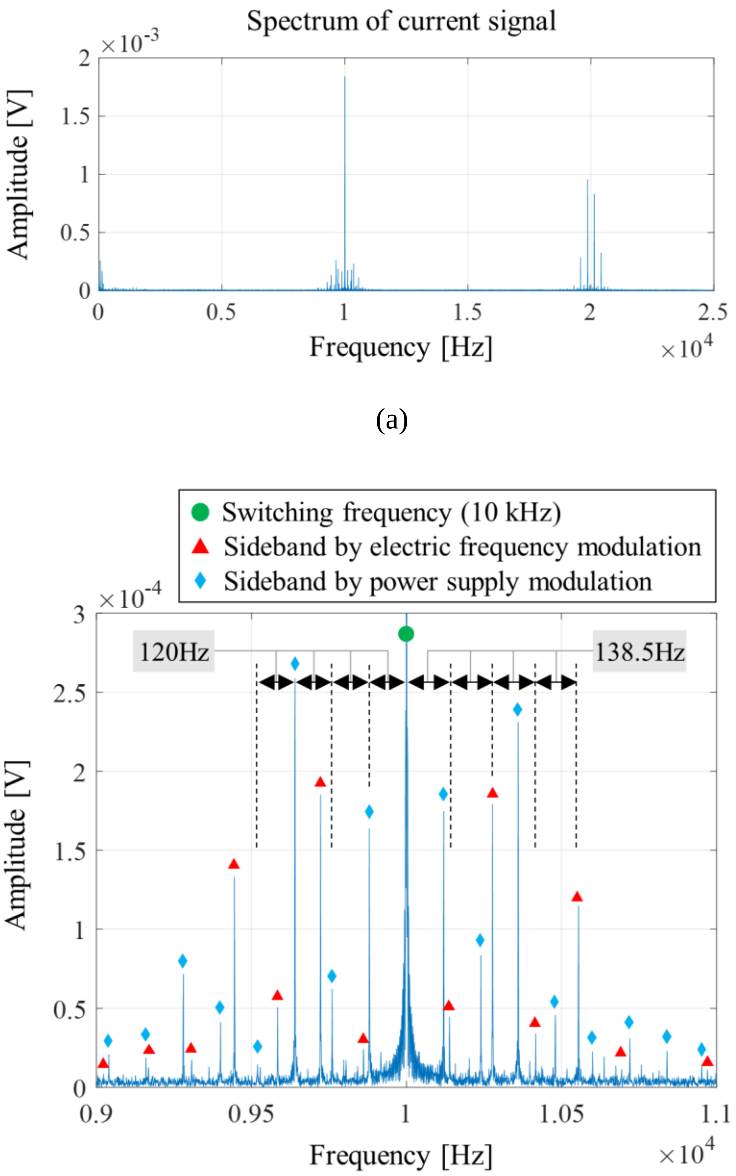

(a)

(b)

Figure 5-9 Spectrum of the current signal: (a) total spectrum, (b) extended local spectrum.

When comparing Figure 5-6(c) and Figure 5-8(c), the periodic signal looks different. The reason is the difference in sampling rate. Since the AE sensor has a sampling rate that is 40 times larger than the current sensor, high-frequency components are additionally fed into the signal, producing microscopic periodicity. However, as shown in Figure 5-7(b) and Figure 5-9(b), the sideband effect of the modulation signals appears similar in the spectrum of both sensors, despite the quantitative difference. From the perspective of bearing diagnosis, the signal to focus on is not the switching frequency but the modulation signal. This means that the signals obtained from two different sensors are affected by the same PWM; thus, it is reasonable to design a filter to eliminate EMI from the AE sensor using the current sensor.

5.3.3 EMI De-noising of the AE signal using Current Data

As the first step of the proposed method, a band-pass filter of 300 kHz to 500 kHz is applied to the AE data. This filter range is chosen to avoid the noises previously described in Section 3. The lower boundary is defined as 300 kHz for filtering undesired signals, such as low-frequency noise, signals from other mechanical components, metal-to-metal contact noise, and frictional elastic waves [29]. The upper bound is chosen because an impulse train above 500 kHz is easily attenuated during elastic wave propagation. Also, this upper bound is intended to reject high-frequency electrical noise close to the megahertz range to enhance the SNR of the bearing defect energy.

Envelope analysis is then applied to the band-passed signal to demodulate the bearing defect. Then, the envelope spectrum is gained using a fast Fourier transform approach. Figure 5-10 illustrates the envelope spectrum of the band-passed signal. The peaks related to the bearing defect and EMI are marked with green inverted triangles and red diamond marks, respectively. The BPFI defect frequency is 229.7 Hz, considering the rotating speed measured from an encoder. The peak at 460 Hz is the harmonic of the BPFI. Other peaks with a green inverted triangle are sidebands of BPFIs, with an interval of 35 Hz, the mechanical rotating frequency. Sidebands are generated by amplitude modulation of the impulse train from the load zone effect during rotation. Red diamond marks are the demodulated EMI, which is the target noise signal to be removed. The figure shows that the bearing defect signs and electrical noise are jumbled together in the zone 2 frequency space. The defect signs are scattered with multi-sidebands, and EMI noise peaks are spiked sparsely among them. Thus, the current signal is handled by the proposed procedure to eliminate the target spike without a manual process.

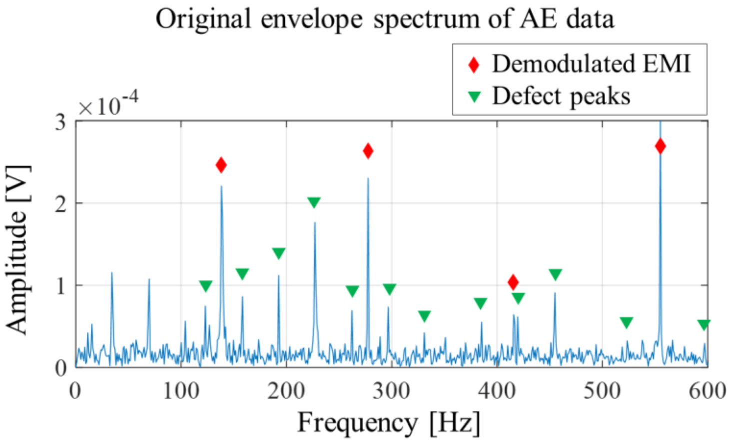

Figure 5-10 The envelope spectrum of the AE data.

The current signal is preprocessed with an EMD. As mentioned earlier, the purpose of the EMD is to adaptively extract information about the electrical noise of the high frequency without expert domain knowledge. Figure 5-11 illustrates several IMF signals and their spectrum. As the order of IMF increases, the frequency band gets lower. Also, the time-domain signal becomes smooth, getting close to DC. This shows that each IMF is not perfectly decomposed (like the band-pass filter) because of the locally orthogonal nature of the IMFs. There are some low-frequency peaks under 1 kHz for every IMF; these are considered to come from the main power supply because it is dominant throughout the whole sample and hard to decompose. The first IMF mainly contains the high-frequency information, including the switching frequency and sideband elements. The second IMF also contains the corresponding component; however, the EMI near 20 kHz is excluded from the observing window. Furthermore, this IMF catches minor electrical components between 4k and 9k that are out of our area of interest.

After decomposing the current signal with EMD, the first IMF signal is selected for the envelope analysis, as done for the AE data. The first IMF signal is selected because it contains a relatively large amount of information about the EMI, among the IMFs. Figure 5-12(a) shows the time domain plot of the first IMF; the orange lines are the upper and lower envelope. Figure 5-12(b) shows the spectrum of the envelope signal. The resulting spectrum reveals two primary signals: the electrical frequency and the power supply components. The electrical frequency is 138.7 Hz and the power supply components are 120 Hz. Both signals become a basis signal modulates the electrical frequency signal because there are minor peaks with a basis of about 19 Hz, which is the difference between the two primary basis frequencies.

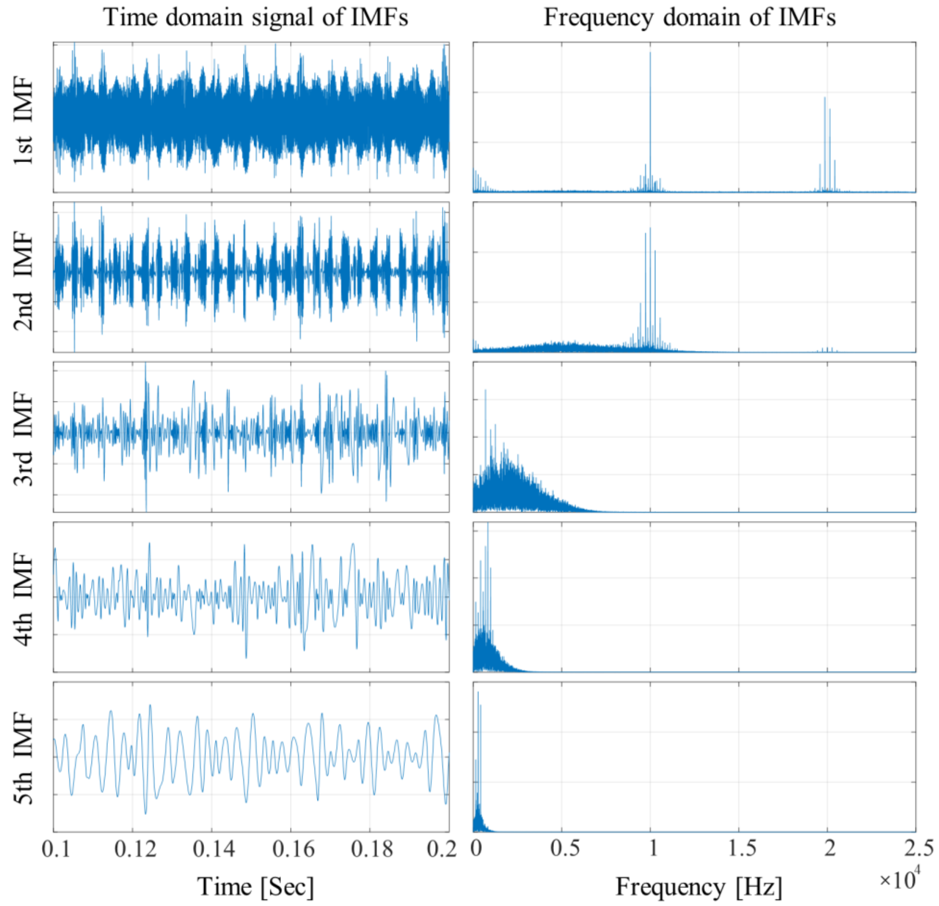

Figure 5-11 Time- and frequency-domain signals along the sequence of the IMF.

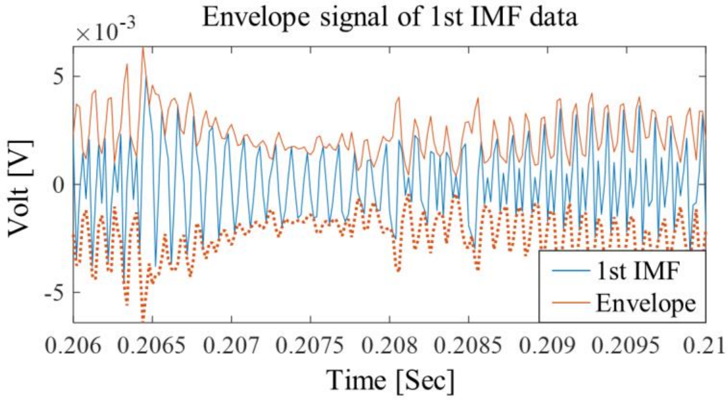

(a)

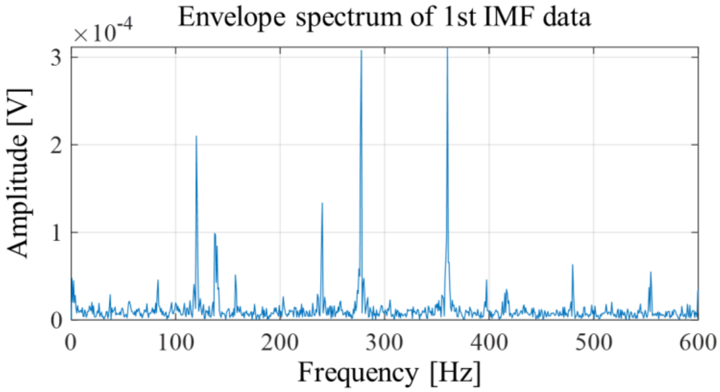

(b)

Figure 5-12 Results of envelope analysis of the 1st IMF data: (a) time-domain plot of current IMF with envelope, and (b) envelope spectrum of the IMF.

The envelope spectrum of the current signal is then utilized for designing the filter, following the steps from Section 3.3. The first step is resampling to meet the frequency resolution of AE and the current signal. In this experiment, the frequency resolution is equal for both sensors due to the same sampling time. Thus, there is no need to resample the spectrum. The window size is defined as ten times the BPFI, 2297Hz, to avoid the undesired high-frequency peaks. For the next step, the probabilistic distribution is found for the given signal. In this study, five distributions are considered to fit the data: normal, lognormal, exponential, extreme, and Weibull distribution. Each distribution's parameter is optimized by maximum likelihood estimation. Table 5-2 shows the fitting score, and the Weibull distribution is chosen. Figure 5-13 shows the histogram and fitting result. The blue rods represent the count in each bin, and the red line is the probability density function with the Weibull distribution. The y-axis of the histogram is normalized for convenience of comparison with the PDF. The data above about 0.5×10^4 volts mean the electrical noise peaks on the envelope spectrum of the current, which will be transformed to a CDF value close to one.

Table 5-2. Maximum log-likelihood comparison for five distributions.

Distribution	Maximum log-likelihood
Normal	50988.1
Lognormal	53906.2
Exponential	53636.5
Extreme	43933.7
Weibull	54055.4

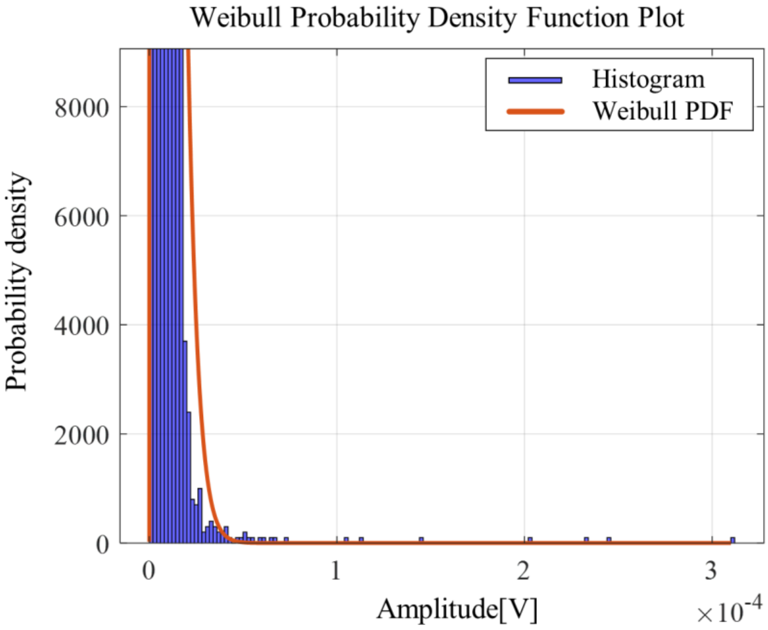

Figure 5-13 PDF fitting on a histogram from the envelope spectrum amplitude of the current IMF with a Weibull distribution.

Finally, Figure 5-14 shows the designed filter and the resulting signal after applying the proposed filtering method. The designed filter is normalized over the whole spectrum, and the lower frequency range is shown in Figure 5-14(a), in which the array of values is calculated by Equation (5.6) using the envelope spectrum of the 1st IMF. This represents a value of almost zero at the point corresponding to the EMI peaks. This makes the filter able to achieve selective removal of target noise. Figure 5-14(b) shows the envelope spectrum after the filtering process. Compared to Figure 5-10, it selectively rejects the local frequency energy at the red diamond marks. When using the proposed method, although some side peaks of a defect can be weakened and fault information can be lost after de-noising when the defect peaks are close to the EMI peaks, the overall EMI noise components of the AE data are de-noised well, without significant disturbance of the main bearing defects.

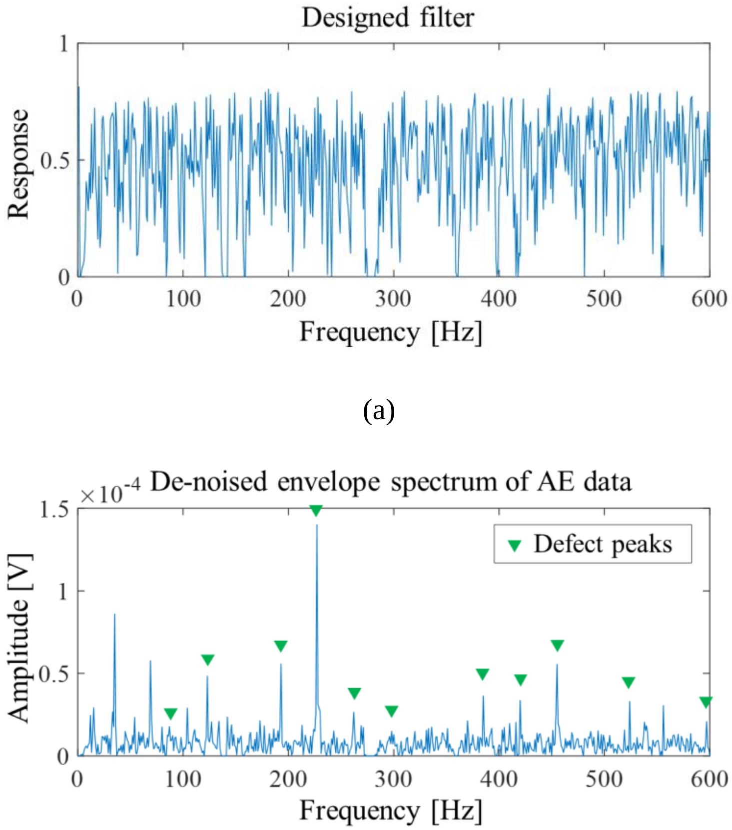

Figure 5-14 Results of de-noising the electrical noise: (a) a de-noising filter designed using the current signal, and (b) the de-noised envelope spectrum of the AE signal.

Additional studies are conducted to validate the proposed idea in Sections 5.2.2 and 5.2.3. Firstly, to check the effectiveness of the EMI signal extraction process for proper noise elimination, the proposed multi-sensor-based filtering process has proceeded without EMI components extraction. For designing a dynamic filter, the 5th IMF signal is hired, which rarely contains EMI components. Figure 5-15(a) shows the envelope spectrum of de-noising results without EMI components extraction. The filter response made by low-frequency components of current signals reduces AE signals' the overall envelope spectrum amplitude. The EMI noise components still remain except for the first harmonics of EMI noise component. In addition, some of bearing defect peaks seem to be distorted by non-EMI and background components. Secondly, to test the effectiveness of probability-based dynamic filter, the proposed de-noising framework has proceeded without dynamic filter designs. The filter's response function is designed with simple normalization of reverse current envelope spectrum in linear scale, which does not contain cumulative statistical techniques. Figure 5-15(b) shows de-noising results without probability-based dynamic filter designs. It shows the little signal distortion of bearing defect-related peaks. A few EMI-related peaks almost disappear. However the overall EMI components still remain with just a little amplitude shifting. This issue derives from the energy difference of target noise between AE and current sensors. These two additional tests validate that the proposed multi-sensor-based EMI filter design should contain proper EMI extraction and dynamic filter design as suggested in Sections 5.2.2 and 5.2.3.

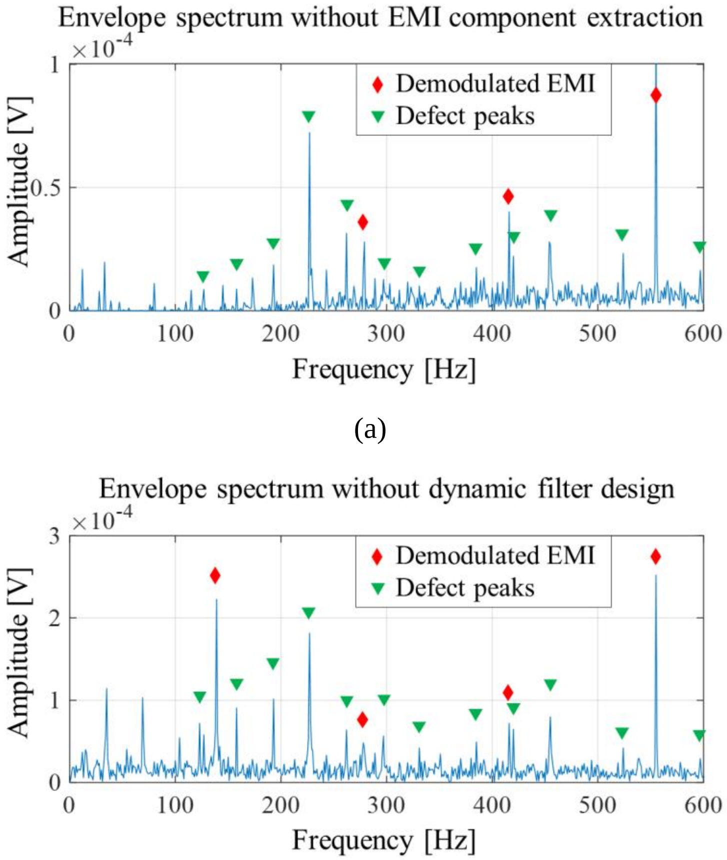

(a)

(b)

Figure 5-15 Envelope spectrum results of electrical noise elimination for additional comparative studies: (a) test without EMI component extraction, and (b) test without probability-based dynamic filter design.

5.3.4 Performance Verification of the Proposed Method

To verify the adaptability of the proposed method, an additional experiment is performed under different operating conditions. Figure 5-16 shows the results at 1800 RPM of rotational speed. Both the original envelope spectrum, which contains bearing defect peaks, and demodulated EMI components are observed, as in the case of the 2100 RPM study. Figure 5-16(b) shows that the proposed method adaptively removes electrical noise components, despite the speed variation and spectral change, such as sideband intervals, defect, and noise peaks.

For further verification of the proposed method, comparison studies have been carried out with traditional de-noising methods: wavelet packet decomposition (WPD) and minimum entropy deconvolution (MED). Both methods are widely used to de-noise the unnecessary signal and to find the impulsive fault signal [76]–[79]. For WPD, the Daubechies function – well known for its ability to detect an impulsive defect signal – is utilized as the mother wavelet function [27]. The MED filter is determined with a filter length of 380, through a parametric study with a 0.01 threshold for kurtosis variation and 100 max iterations. Figure 5-17(a) shows the envelope spectrum of a wavelet-filtered AE signal at 2100RPM. Wavelet filtering is implemented with the fourth packet node in the third-level decomposition, which has a target frequency band of 375 kHz to 500 kHz. The main defect peaks seem to have decreased somewhat; however, compared to Figure 5-10, some side peaks are generated around the main electrical noise. Figure 5-17(b) shows the results of MED. It can be seen that the ratio of defect energy to electrical component energy has increased more than before.

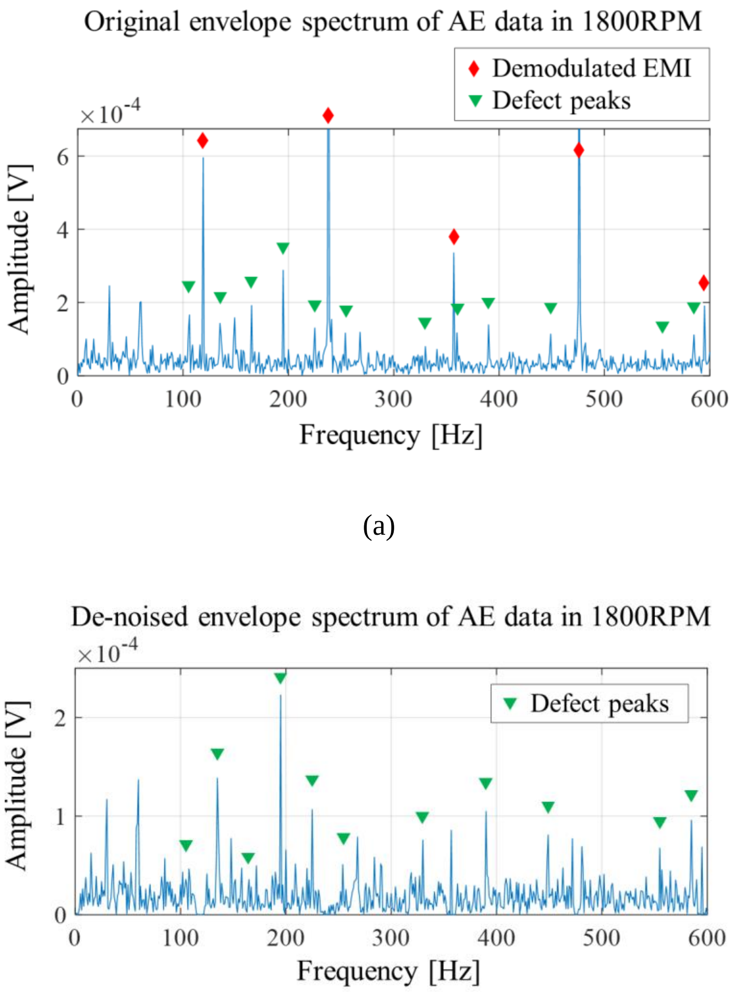
Original envelope spectrum of AE data in 1800RPM

(a)

De-noised envelope spectrum of AE data in 1800RPM

(b)

Figure 5-16 Results of de-noising the electrical noise in an operating condition of 1800 RPM: original envelope spectrum of the AE signal, and (b) de-noised envelope spectrum of the AE signal.

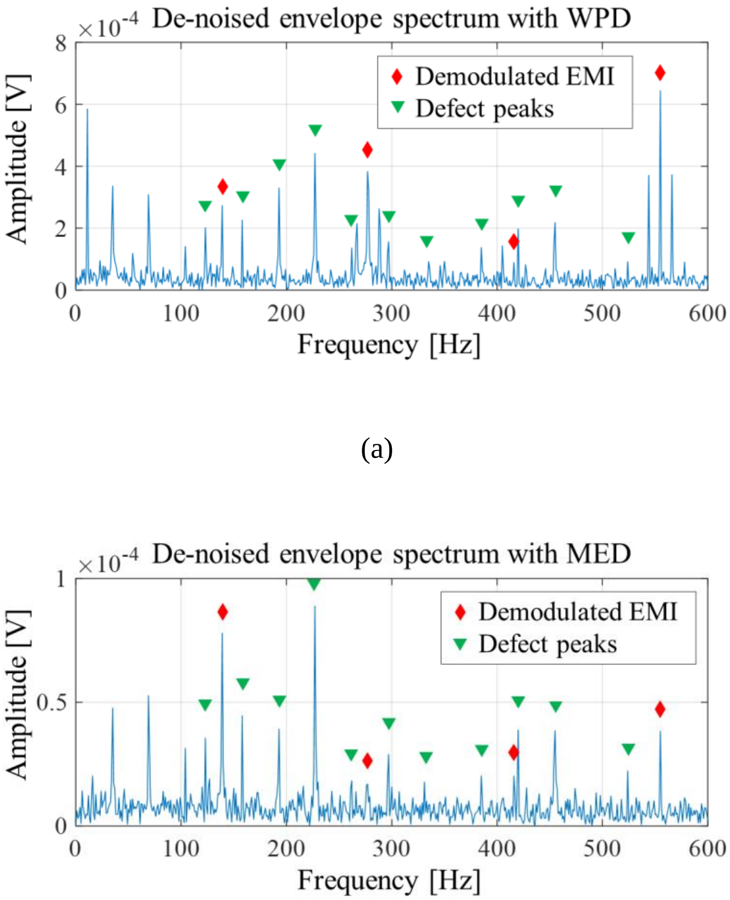

(a)

(b)

Figure 5-17 Envelope spectrum of the comparison study in a 2100RPM condition: (a) wavelet packet decomposition, and (b) minimum entropy deconvolution.

To compare different methods in a quantitative manner, the peak ratio (PR) metric is used [80] Because only the EMI and defect signal matter in this study, those peaks are extracted before applying the PR, using the median absolute deviation (MAD) threshold. MAD, proposed by Leys et al., is widely used for detecting statistically relevant peaks in spectrum analysis [81], [82]. Equations. (5.8) and (5.9) show the formula of the MAD and MAD threshold, where the function *M* stands for the median value of given data. Then the PR is formulated as shown in Equation (5.10), where b_j is the amplitude of the *j*th bearing main defect harmonics and f_n is the amplitude of the *n*th point of the spectrum. The superscript MAD indicates statistically relevant peaks, with MAD threshold as its lower bound. *N* is the number of points related to the upper bound of the target frequency. In this research, *N* is limited to include up to five harmonics of the defect frequency, to exclude meaningless spectral effects. Through the PR metric and MAD, the ratio of the main defect energy can be estimated from among relevant peaks in the spectrum. A higher value represents better detectability of a given spectrum.

$$MAD = 1.4826 \times M[|x - M(x)|] \tag{5.8}$$

$$MAD_{threshold} = [M(x) - 3 * MAD;\ M + 3 * MAD] \tag{5.9}$$

$$PR = \frac{\sum_{j=1}^{J}\left(b_j^{MAD}\right)^2}{\sum_{n=1}^{N}(f_n^{MAD})^2} \tag{5.10}$$

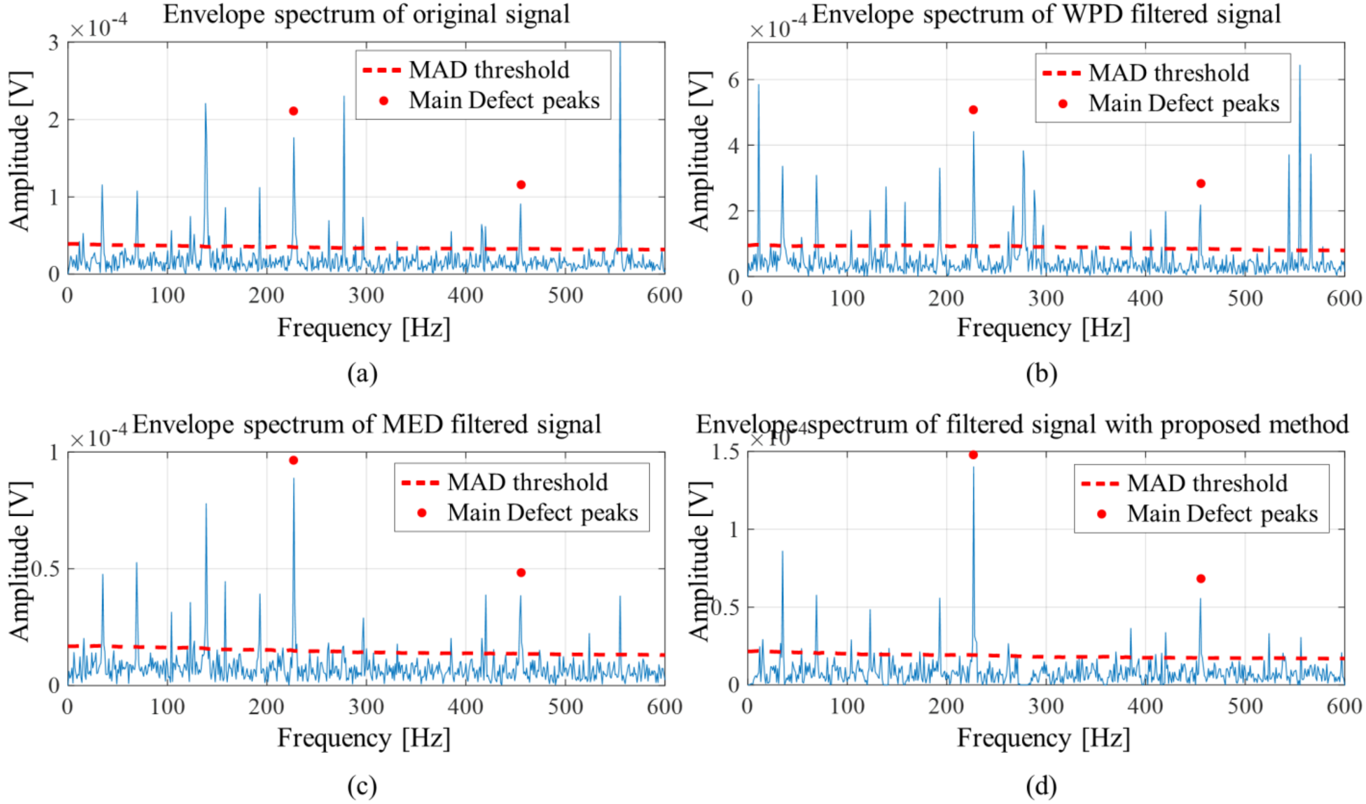

Figure 5-18 Envelope spectrum result with MAD threshold for the 2100RPM condition: (a) Original AE signal, (b) WPD filtered signal, (c) MED filtered signal, and (d) signal filtered by the proposed method.

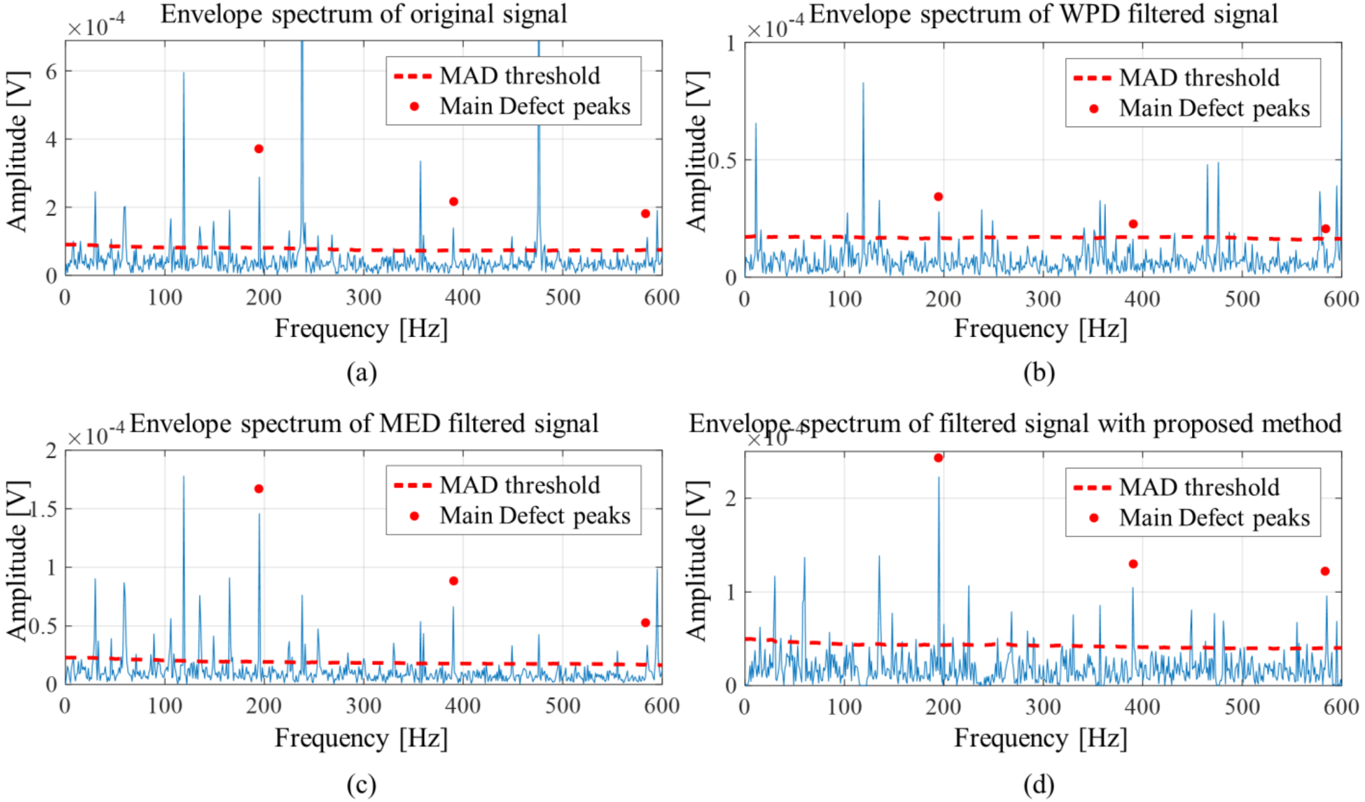
Envelope spectrum of original signal

Envelope spectrum of WPD filtered signal

Envelope spectrum of MED filtered signal

Envelope spectrum of filtered signal with proposed method

(a)

(b)

(c)

(d)

Figure 5-19 Envelope spectrum result with MAD threshold for the 1800RPM condition: (a) Original AE signal, (b) WPD filtered signal, (c) MED filtered signal, and (d) signal filtered by the proposed method.

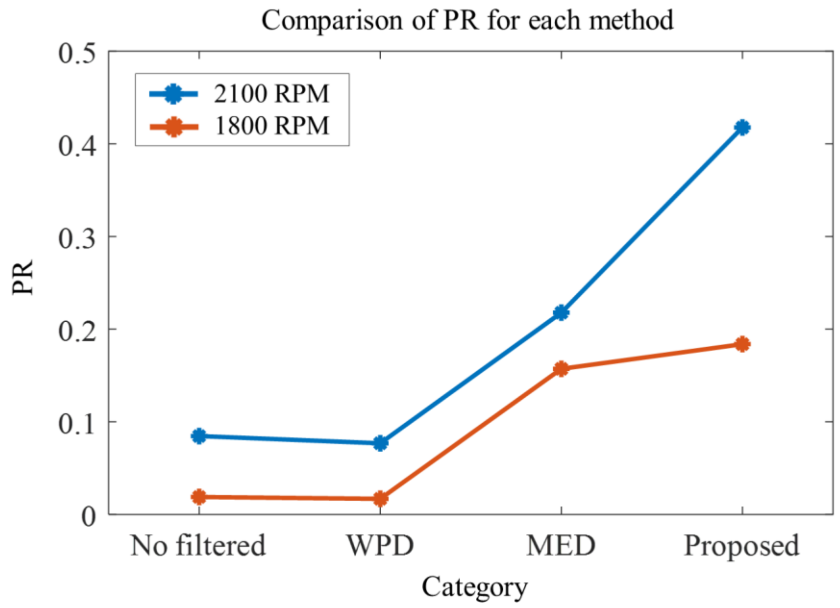

Figure 5-20 Comparison of PR results for two operating speed conditions: 2100 and 1800 RPM.

Figure 5-18 and Figure 5-19 show the envelope spectrum results with MAD thresholds for the 2100 and 1800 RPM speed conditions. The comparative methods' parameters for this analysis are selected in the same manner as in the previous investigation, the results of which are shown in Figure 5-17. The red dotted line represents the MAD thresholds and the red dots indicate the main BPFI peaks and harmonics. WPD filtering somewhat effectively suppresses EMI; however, it produces other sideband noise in both speed conditions. MED filtering effectively enhances the fault components, but fails to sufficiently control demodulated EMI. Figure 5-20 displays the quantified comparative results obtained through the PR. In all categories, the detectability of the 2100RPM condition is higher than that of the 1800RPM condition, due to the decrease of fault energy within the target band caused by the speed drop. The WPD filtered results have numerically worse detectability than the unfiltered results because of the effect of additional peaks around the demodulated EMI. The MED filtered result has better detectability than the unfiltered and WPD filtered cases. The proposed method shows the best detectability from among all methodologies considered, including a sufficient decrease of the electrical component energy.

5.4 Summary and Discussion

This study proposes the design of a filter that removes the electromagnetic interference in an AE signal to enable better fault detection of rolling element bearings. To this end, a current sensor is measured to obtain data containing the EMI features. Then, the measured data is processed using EMD and envelope analysis. Finally, a filter is designed to pick out the undesired peaks that arise from the EMI. The proposed analysis is verified by studying experimental data in two speed conditions, and the results of the proposed method are quantitatively compared with those obtained from other de-noising methods. The suggested method has the following advantages. First, by using the current data, active removal of the EMI from AE signals becomes possible. This multi-sensor approach can extend the use of AE signals in REB diagnosis, regardless of failure mode. Second, this method is easy to use and does not require expert knowledge of the system or physical interpretation of the spectrum. Thus, the proposed method could be valuable in situations where the component (i.e., bearing, motor) specifications are not clear. Third, the proposed algorithm does not need rotating speed info. This allows its use operate under variable-speed conditions, even in tacholess driving. Furthermore, the suggested method is expected to be applicable for use with different sensors, such as accelerometers, velocimeters, ultrasonic sensors, etc., whenever PWM noise disturbs the bearing defect frequency.

Sections of this chapter have been published or submitted as the following journal articles:

1) **Su J. Kim**, Keunsu Kim, Taewan Hwang, Jongmin Park, Hwayong Jeong, Taejin Kim, and Byeng D. Youn, “Motor-current-based electromagnetic interference de-noising method for rolling element bearing diagnosis using acoustic emission sensors,” *Measurement*, Vol. 193, pp. 110912, 2022.

Chapter 6

Conclusions

6.1 Contributions and Significance

This research investigates the extraction of bearing fault information from acoustic emission signals under noisy conditions. The dissertation contains two novel techniques as the research thrusts: 1) noise-robust and efficient frequency band selection for AE signals with fault-related defect measure; 2) multi-sensor-based de-noising filter design for electromagnetic interference. Those proposed research are expected to offer the following potential contributions and significance.

Contribution 1: Suggestion of advanced optimum band selection architecture considering bearing defect information

This dissertation suggests a novel band selection architecture for AE signals. The main idea of the proposed architecture is based on segment signals made by using the target defect period, which enables the fast searching for optimum frequency band despite a large sampling rate data. The suggested effective band searching architecture can be applied not only to an AE sensor but also to other sensors with a high sampling rate, such as ultrasound and ultra-high frequency (UHF) sensors.

Contribution 2: Suggestion of a novel defect measure based on kurtosis and correlation.

This dissertation defines a novel defect measure rooted in kurtosis and correlation of specially segmented signals. The segment signals are created using bearing defect information. However, the fundamentals of the proposed defect measure is figuring out the impulsive and periodic character of target signals. This means that the proposed method can also be applied to other rotary components that carry periodic and impulsive defect signals.

Contribution 3: Generation of the simulated EMI signals.

This dissertation generates the simulated EMI signals to validate the proposed methods. The analytic form of EMI is highly non-stationary and complex, including the superposition of a number of Bessel functions. Thus, the simulation of EMI components is not easy. This dissertation has significance in modeling the main components of EMI and simulating its effect on sensors for diagnostic purposes, even if those are not identical to the analytic form of EMI.

Contribution 4: Suggestion of multi-sensor based de-noise filter for electrical noise components

This dissertation suggests a novel filter that eliminates the effect of EMI noise on envelope spectrum domain. To design desire filter, the proposed method utilizes current signals for motor input and develops an active EMI extractor through EMD technique. The EMI components in both sensors are not the same, but they are definitely correlated. By using an adaptive EMI extractor and probabilistic filter design, the proposed method can eliminate target EMI components regardless of bearing failure modes and operating conditions. In addition, proposed filtering even operates in situations where the component (i.e., bearing, motor) specifications are unclear.

Contribution 5: Potential of expandability for the electrical components elimination

The main idea of the proposed filter design is to utilize the current input of motor, which is the output of motor driver controlling the operating condition of motor. This fact implies that the suggested filtering is expected to be applicable for use with different sensors, such as accelerometers, velocimeters, ultrasonic sensors, etc., whenever PWM noise disturbs the main target sensor signals.

Contribution 6: Solutions for the practical issues of acoustic emission techniques in the industrial fields

This dissertation aims at the practical issue of AE sensors in the industrial fields. In the real site, a comprehensive understanding of measured signal is almost impossible, and the computing capacity is sometimes poor, such as the edgy computing systems. For these reasons, fine-quality data gathering and proper diagnosis are almost impossible. The proposed idea in this dissertation focus on solving those practical issues. The proposed defect measure in the first thrust uses only time-domain signals without spectral reasoning, which reduces the computational burden and allows practical use in industry. In addition, the dynamic filter design of the second thrust does not require expert knowledge of the system or physical interpretation of the spectrum, which is expected to reduce the burden of field engineers and increase the practicality of diagnosis using AE sensors.

6.2 Suggestions for Future Research

This dissertation offers technical advances for rolling element bearing system diagnosis using AE sensor. Although the proposed methods clearly improve the overall performance, several limitations and future work still remain to be solved.

Suggestion 1: Improvement of noise information extractor to solve mode mixing problem

The proposed method has a limitation in the de-noising filter's optimal parameter selection, such as window size, distribution estimation, and target IMF, within the decomposed results from the EMD. In particular, the EMD algorithm decomposes the given signal empirically without physical meaning, which generates a mode mixing problem. Using the unsettled information from each of the IMFs, it does not guarantee that the first IMF always includes high-frequency EMI. Of course, the lower IMF has a large probability of including EMI; however, this still requires manual selection by a human being. Building on the initial success of the proposed method, these limitations will be addressed in future work. Future research will examine the use of advanced algorithms to optimize the design parameters and determine a proper quantitative indicator for robust EMI filter design.

Suggestion 2: Development of proposed methods for variable speed conditions from constant speed operations.

The proposed methods in this dissertation are demonstrated with constant operating speed conditions. These facts indicate that there is no guarantee for the performance of proposed methods in variable operating applications in many industrial systems. The variable speed conditions create much uncertainty and performance variations. Therefore, further research on variable speed conditions needs to be performed, and the robustness of the proposed idea must be checked.

Suggestion 3: Development of the selectable parameter optimizer for the better

performance of optimum band searching

The proposed band selection method has a limitation in its inability to optimize the selectable parameters. Although this paper verifies the effectiveness of the proposed idea with fixed parameters, optimized parameters could generate better performance. For this reason, parameter optimization is still open to discussion, with a trade-off relationship between algorithmic performance and time cost. The scope of this paper is to describe the newly proposed band-selection procedure and verify the algorithm; parameter optimization and related issues will be studied in future research.

References

[1] J. H. Jung, B. C. Jeon, B. D. Youn, M. Kim, D. Kim, and Y. Kim, "Omnidirectional regeneration (ODR) of proximity sensor signals for robust diagnosis of journal bearing systems," *Mech. Syst. Signal Process.*, 2017, doi: 10.1016/j.ymssp.2016.12.030.

[2] J. Park, M. Hamadache, J. M. Ha, Y. Kim, K. Na, and B. D. Youn, "A positive energy residual (PER) based planetary gear fault detection method under variable speed conditions," *Mech. Syst. Signal Process.*, 2019, doi: 10.1016/j.ymssp.2018.08.010.

[3] J. Lee, H. Oh, C. H. Park, B. D. Youn, and B. Han, "Test scheme and degradation model of Accumulated Electrostatic Discharge (ESD) damage for Insulated Gate Bipolar Transistor (IGBT) prognostics," *IEEE Trans. Device Mater. Reliab.*, 2019, doi: 10.1109/TDMR.2019.2898920.

[4] C. H. Park *et al.*, "Drive-tolerant current residual variance (DTCRV) for fault detection of a permanent magnet synchronous motor under operational speed and load torque conditions," *IEEE Access*, 2021, doi: 10.1109/ACCESS.2021.3068425.

[5] Y. Kim, J. M. Ha, K. Na, J. Park, and B. D. Youn, "Cepstrum-assisted empirical wavelet transform (CEWT)-based improved demodulation analysis for fault diagnostics of planetary gearboxes," *Meas. J. Int. Meas. Confed.*, 2021, doi: 10.1016/j.measurement.2021.109796.

[6] T. A. Harris and M. N. Kotzalas, *Essential concepts of bearing technology*. 2006.

[7] V. Atamuradov, K. Medjaher, P. Dersin, B. Lamoureux, and N. Zerhouni, "Prognostics and health management for maintenance practitioners - review, implementation and tools evaluation," *Int. J. Progn. Heal. Manag.*, 2017, doi: 10.36001/ijphm.2017.v8i3.2667.

[8] B. D. Youn, C. Hu, and P. Wang, "Resilience-driven system design of complex engineered systems," *J. Mech. Des. Trans. ASME*, 2011, doi: 10.1115/1.4004981.

[9] C. Hu, B. D. Youn, P. Wang, and J. Taek Yoon, "Ensemble of data-driven prognostic algorithms for robust prediction of remaining useful life," *Reliab. Eng. Syst. Saf.*, 2012, doi: 10.1016/j.ress.2012.03.008.

[10] P. Wang, B. D. Youn, and C. Hu, "A generic probabilistic framework for structural health prognostics and uncertainty management," *Mech. Syst. Signal Process.*, 2012, doi: 10.1016/j.ymssp.2011.10.019.

[11] T. Kim, G. Lee, and B. D. Youn, "PHM experimental design for effective state separation using Jensen–Shannon divergence," *Reliab. Eng. Syst. Saf.*, 2019, doi: 10.1016/j.ress.2019.106503.

[12] N. Tandon and A. Choudhury, "Review of vibration and acoustic measurement methods for the detection of defects in rolling element bearings," *Tribol. Int.*, 1999, doi: 10.1016/S0301-679X(99)00077-8.

[13] A. Sturm and D. I. S. Uhlemann, “Diagnosis of plain bearings by acoustic emission analysis,” *Measurement*, 1985, doi: 10.1016/0263-2241(85)90030-2.

[14] Z. Liu, X. Wang, and L. Zhang, “Fault Diagnosis of Industrial Wind Turbine Blade Bearing Using Acoustic Emission Analysis,” *IEEE Trans. Instrum. Meas.*, 2020, doi: 10.1109/TIM.2020.2969062.

[15] H. Oh, M. H. Azarian, and M. Pecht, “Estimation of fan bearing degradation using acoustic emission analysis and mahalanobis distance,” 2011.

[16] M. Žvokelj, S. Zupan, and I. Prebil, “EEMD-based multiscale ICA method for slewing bearing fault detection and diagnosis,” *J. Sound Vib.*, 2016, doi: 10.1016/j.jsv.2016.01.046.

[17] A. Amini, M. Entezami, and M. Papaelias, “Onboard detection of railway axle bearing defects using envelope analysis of high frequency acoustic emission signals,” *Case Stud. Nondestruct. Test. Eval.*, 2016, doi: 10.1016/j.csndt.2016.06.002.

[18] M. Motahari-Nezhad and S. M. Jafari, “ANFIS system for prognosis of dynamometer high-speed ball bearing based on frequency domain acoustic emission signals,” *Meas. J. Int. Meas. Confed.*, 2020, doi: 10.1016/j.measurement.2020.108154.

[19] N. Jamaludin and D. Mba, “Monitoring extremely slow rolling element bearings: Part I,” *NDT E Int.*, 2002, doi: 10.1016/S0963-8695(02)00005-1.

[20] W. Caesarendra, B. Kosasih, A. K. Tieu, H. Zhu, C. A. S. Moodie, and Q. Zhu, “Acoustic emission-based condition monitoring methods: Review and application for low speed slew bearing,” *Mech. Syst. Signal Process.*, 2016, doi: 10.1016/j.ymssp.2015.10.020.

[21] S. Saravanan, G. S. Yadava, and P. V. Rao, “Condition monitoring studies on spindle bearing of a lathe,” *Int. J. Adv. Manuf. Technol.*, 2006, doi: 10.1007/s00170-004-2449-0.

[22] M. J. Hasan, M. M. M. Islam, and J. M. Kim, “Acoustic spectral imaging and transfer learning for reliable bearing fault diagnosis under variable speed conditions,” *Meas. J. Int. Meas. Confed.*, 2019, doi: 10.1016/j.measurement.2019.02.075.

[23] A. M. Al-Ghamd and D. Mba, “A comparative experimental study on the use of acoustic emission and vibration analysis for bearing defect identification and estimation of defect size,” *Mech. Syst. Signal Process.*, 2006, doi: 10.1016/j.ymssp.2004.10.013.

[24] M. Elforjani and D. Mba, “Monitoring the onset and propagation of natural degradation process in a slow speed rolling element bearing with acoustic emission,” *J. Vib. Acoust. Trans. ASME*, 2008, doi: 10.1115/1.2948413.

[25] E. Y. Kim, A. C. C. Tan, J. Mathew, and B. S. Yang, “Condition monitoring of low speed bearings: A comparative study of the ultrasound technique versus vibration measurements,” 2008, doi: 10.1080/14484846.2008.11464546.

[26] A. Widodo *et al.*, “Fault diagnosis of low speed bearing based on relevance vector machine and support vector machine,” *Expert Syst. Appl.*, 2009, doi: 10.1016/j.eswa.2008.09.033.

[27] B. Eftekharnejad, M. R. Carrasco, B. Charnley, and D. Mba, “The application of spectral kurtosis on Acoustic Emission and vibrations from a defective bearing,” *Mech. Syst. Signal Process.*, 2011, doi: 10.1016/j.ymssp.2010.06.010.

[28] P. Nguyen, M. Kang, J. M. Kim, B. H. Ahn, J. M. Ha, and B. K. Choi, “Robust condition monitoring of rolling element bearings using de-noising and envelope analysis with signal decomposition techniques,” *Expert Syst. Appl.*, 2015, doi: 10.1016/j.eswa.2015.07.064.

[29] J. L. Ferrando Chacon, V. Kappatos, W. Balachandran, and T. H. Gan, “A novel approach for incipient defect detection in rolling bearings using acoustic emission technique,” *Appl. Acoust.*, 2015, doi: 10.1016/j.apacoust.2014.09.002.

[30] P. K. Gupta, “Advanced dynamics of rolling elements.,” 1984, doi: 10.1115/1.3171847.

[31] I. 15243, “Bearing Failure Mode Classification,” *Science (80-.).*, 2006.

[32] F. Sadeghi, B. Jalalahmadi, T. S. Slack, N. Raje, and N. K. Arakere, “A review of rolling contact fatigue,” *J. Tribol.*, 2009, doi: 10.1115/1.3209132.

[33] T. A. Harris and M. N. Kotzalas, *Advanced Concepts of Bearing Technology*.

2006.

[34] P. D. McFadden and J. D. Smith, “Model for the vibration produced by a single point defect in a rolling element bearing,” *J. Sound Vib.*, 1984, doi: 10.1016/0022-460X(84)90595-9.

[35] R. B. Randall and J. Antoni, “Rolling element bearing diagnostics-A tutorial,” *Mechanical Systems and Signal Processing*. 2011, doi: 10.1016/j.ymssp.2010.07.017.

[36] K. Yu, T. R. Lin, J. Tan, and H. Ma, “An adaptive sensitive frequency band selection method for empirical wavelet transform and its application in bearing fault diagnosis,” *Meas. J. Int. Meas. Confed.*, 2019, doi: 10.1016/j.measurement.2018.10.086.

[37] W. A. Smith, P. Borghesani, Q. Ni, K. Wang, and Z. Peng, “Optimal demodulation-band selection for envelope-based diagnostics: A comparative study of traditional and novel tools,” *Mech. Syst. Signal Process.*, 2019, doi: 10.1016/j.ymssp.2019.106303.

[38] D. Dyer and R. M. Stewart, “Detection of rolling element bearing damage by statistical vibration analysis,” *J. Mech. Des. Trans. ASME*, 1978, doi: 10.1115/1.3453905.

[39] R. F. Dwyer, “Detection of non-gaussian signals by frequency domain kurtosis estimation.,” 1983, doi: 10.1109/icassp.1983.1172264.

[40] C. Ottonello and S. Pagnan, “Modified frequency domain kurtosis for signal

processing," *Electron. Lett.*, 1994, doi: 10.1049/el:19940777.

[41] J. Antoni, "The spectral kurtosis: A useful tool for characterising non-stationary signals," *Mech. Syst. Signal Process.*, 2006, doi: 10.1016/j.ymssp.2004.09.001.

[42] J. Antoni and R. B. Randall, "The spectral kurtosis: Application to the vibratory surveillance and diagnostics of rotating machines," *Mech. Syst. Signal Process.*, 2006, doi: 10.1016/j.ymssp.2004.09.002.

[43] J. Antoni, "Fast computation of the kurtogram for the detection of transient faults," *Mech. Syst. Signal Process.*, 2007, doi: 10.1016/j.ymssp.2005.12.002.

[44] T. Barszcz and A. Jabłoński, "A novel method for the optimal band selection for vibration signal demodulation and comparison with the Kurtogram," *Mech. Syst. Signal Process.*, 2011, doi: 10.1016/j.ymssp.2010.05.018.

[45] W. A. Smith, R. B. Randall, X. de C. du Mée, and P. Peng, "Use of cyclostationary properties to diagnose planet bearing faults in variable speed conditions," *10th DST Gr. Int. Conf. Heal. usage Monit. Syst. 17th Aust. Aerosp. Congr.*, 2017.

[46] P. Borghesani, P. Pennacchi, and S. Chatterton, "The relationship between kurtosis- and envelope-based indexes for the diagnostic of rolling element bearings," *Mech. Syst. Signal Process.*, 2014, doi: 10.1016/j.ymssp.2013.10.007.

[47] J. Antoni and P. Borghesani, "A statistical methodology for the design of

condition indicators," *Mech. Syst. Signal Process.,* 2019, doi: 10.1016/j.ymssp.2018.05.012.

[48] X. Zhang, J. Kang, L. Xiao, J. Zhao, and H. Teng, "A new improved Kurtogram and its application to bearing fault diagnosis," *Shock Vib.*, 2015, doi: 10.1155/2015/385412.

[49] G. L. McDonald and Q. Zhao, "Multipoint optimal minimum entropy deconvolution and convolution fix: Application to vibration fault detection," *Mech. Syst. Signal Process.,* 2017, doi: 10.1016/j.ymssp.2016.05.036.

[50] J. Antoni, "The infogram: Entropic evidence of the signature of repetitive transients," *Mech. Syst. Signal Process.,* 2016, doi: 10.1016/j.ymssp.2015.04.034.

[51] A. Moshrefzadeh and A. Fasana, "The Autogram: An effective approach for selecting the optimal demodulation band in rolling element bearings diagnosis," *Mech. Syst. Signal Process.,* 2018, doi: 10.1016/j.ymssp.2017.12.009.

[52] T. Drouillard, "A history of acoustic emission," *J. Acoust. Emiss.,* 1996.

[53] S. Gholizadeh, Z. Lemana, and B. T. H. T. Baharudinb, "A review of the application of acoustic emission technique in engineering," *Structural Engineering and Mechanics*. 2015, doi: 10.12989/sem.2015.54.6.1075.

[54] A. C. C. Tan, Y. H. Kim, and V. Kosse, "Condition monitoring of low-speed bearings - A review," 2008, doi: 10.1080/14484846.2008.11464558.

[55] M. M. M. Islam and J. M. Kim, “Time–frequency envelope analysis-based sub-band selection and probabilistic support vector machines for multi-fault diagnosis of low-speed bearings,” *J. Ambient Intell. Humaniz. Comput.*, 2017, doi: 10.1007/s12652-017-0585-2.

[56] H. N. Nguyen, J. Kim, and J. M. Kim, “Optimal sub-band analysis based on the envelope power spectrum for effective fault detection in bearing under variable, low speeds,” *Sensors (Switzerland)*, 2018, doi: 10.3390/s18051389.

[57] D. Quezada and C. Molina Vicuña, “Damage Assessment of Rolling Element Bearing Using Cyclostationary Processing of AE Signals with Electromagnetic Interference,” *Appl. Cond. Monit.*, 2015.

[58] S. J. Kim *et al.*, “Motor-current-based electromagnetic interference de-noising method for rolling element bearing diagnosis using acoustic emission sensors,” *Meas. J. Int. Meas. Confed.*, 2022, doi: 10.1016/j.measurement.2022.110912.

[59] C. M. Vicuña and C. Höweler, “A method for reduction of Acoustic Emission (AE) data with application in machine failure detection and diagnosis,” *Mech. Syst. Signal Process.*, 2017, doi: 10.1016/j.ymssp.2017.04.040.

[60] J. Z. Sikorska and D. Mba, “Ae condition monitoring: Challenges and opportunities,” 2006, doi: 10.1007/978-1-84628-814-2_14.

[61] A. Mauricio *et al.*, “Bearing diagnostics under strong electromagnetic interference based on Integrated Spectral Coherence,” *Mech. Syst. Signal*

Process., 2020, doi: 10.1016/j.ymssp.2020.106673.

[62] *Practical Acoustic Emission Testing*. 2016.

[63] G. L. Skibinski, R. J. Kerkman, and D. Schlegel, “EMI emissions of modern PWM ac drives,” *IEEE Ind. Appl. Mag.*, 1999, doi: 10.1109/2943.798337.

[64] W. A. Smith, Z. Fan, Z. Peng, H. Li, and R. B. Randall, “Optimised Spectral Kurtosis for bearing diagnostics under electromagnetic interference,” *Mech. Syst. Signal Process.*, 2016, doi: 10.1016/j.ymssp.2015.12.034.

[65] J. Sun, “Pulse-width modulation,” in *Advances in Industrial Control*, 2012.

[66] J. Antoni and R. B. Randall, “Unsupervised noise cancellation for vibration signals: Part I - Evaluation of adaptive algorithms,” *Mech. Syst. Signal Process.*, 2004, doi: 10.1016/S0888-3270(03)00012-8.

[67] J. Antoni and R. B. Randall, “Unsupervised noise cancellation for vibration signals: Part II - A novel frequency-domain algorithm,” *Mech. Syst. Signal Process.*, 2004, doi: 10.1016/S0888-3270(03)00013-X.

[68] R. B. Randall and N. Sawalhi, “A new method for separating discrete components from a signal,” 2011.

[69] P. H. Westfall, “Kurtosis as Peakedness, 1905–2014. R.I.P.,” *Am. Stat.*, 2014, doi: 10.1080/00031305.2014.917055.

[70] Y. He, X. Zhang, and M. I. Friswell, “Defect diagnosis for rolling element bearings using acoustic emission,” *J. Vib. Acoust. Trans. ASME*, 2009, doi:

10.1115/1.4000480.

[71] A. V Oppenheim and R. W. Schafer, “Discrete time signal processing 2nd edition,” *Book*. 1998.

[72] K. M. M. Prabhu, *Window functions and their applications in signal processing*. 2018.

[73] K. Detrich, S. Ganeriwala, and N. Sawalhi, “The interference of variable frequency drives (VFDS) on the vibration signature analysis of machine defects,” 2013.

[74] N. E. Huang *et al.*, “The empirical mode decomposition and the Hubert spectrum for nonlinear and non-stationary time series analysis,” *Proc. R. Soc. A Math. Phys. Eng. Sci.*, 1998, doi: 10.1098/rspa.1998.0193.

[75] A. Zeiler, R. Faltermeier, I. R. Keck, A. M. Tomé, C. G. Puntonet, and E. W. Lang, “Empirical mode decomposition - An introduction,” 2010, doi: 10.1109/IJCNN.2010.5596829.

[76] R. A. Wiggins, “Minimum entropy deconvolution,” *Geoexploration*, 1978, doi: 10.1016/0016-7142(78)90005-4.

[77] N. Sawalhi, R. B. Randall, and H. Endo, “The enhancement of fault detection and diagnosis in rolling element bearings using minimum entropy deconvolution combined with spectral kurtosis,” *Mech. Syst. Signal Process.*, 2007, doi: 10.1016/j.ymssp.2006.12.002.

[78] F. Hemmati, W. Orfali, and M. S. Gadala, “Roller bearing acoustic signature extraction by wavelet packet transform, applications in fault detection and size estimation,” *Appl. Acoust.*, 2016, doi: 10.1016/j.apacoust.2015.11.003.

[79] N. G. Nikolaou and I. A. Antoniadis, “Rolling element bearing fault diagnosis using wavelet packets,” *NDT E Int.*, 2002, doi: 10.1016/S0963-8695(01)00044-5.

[80] J. Shiroishi, Y. Li, S. Liang, T. Kurfess, and S. Danyluk, “Bearing condition diagnostics via vibration and acoustic emission measurements,” *Mech. Syst. Signal Process.*, 1997, doi: 10.1006/mssp.1997.0113.

[81] C. Leys, C. Ley, O. Klein, P. Bernard, and L. Licata, “Detecting outliers: Do not use standard deviation around the mean, use absolute deviation around the median,” *J. Exp. Soc. Psychol.*, 2013, doi: 10.1016/j.jesp.2013.03.013.

[82] A. Mauricio, W. A. Smith, R. B. Randall, J. Antoni, and K. Gryllias, “Improved Envelope Spectrum via Feature Optimisation-gram (IESFOgram): A novel tool for rolling element bearing diagnostics under non-stationary operating conditions,” *Mech. Syst. Signal Process.*, 2020, doi: 10.1016/j.ymssp.2020.106891.

국문 초록

음향방출 기반 구름 요소 베어링 진단을 위한 잡음 환경에서의 고장 정보 추출 연구

현대 산업에서 구름 요소 베어링(rolling element bearing)은 회전체를 구성하는 부품 가운데 가장 다양한 시스템에서 활용되며 핵심적인 역할을 하는 기계 부품 중 하나이다. 베어링은 회전체에 가해지는 하중 및 자중을 지지하며, 축의 안정적인 회전을 보조한다. 예기치 못한 베어링의 파손은 물적·인적 피해를 야기시킬 뿐 아니라, 이의 유지 보수를 위한 회전체 시스템의 가동 중단으로 때때로 막대한 경제적인 손실을 초래하기도 한다. 이를 예방하기 위하여 많은 연구자들은 가속도계 혹은 속도계와 같은 진동 기반의 센서를 통하여 베어링의 건전성 상태를 진단하는 연구를 수행해왔다. 최근에는 데이터 처리 기술의 발전과 발맞추어 음향방출(acoustic emission) 센서를 활용하여 보다 정밀하게 베어링을 진단하는 기술들이 활발히 연구되고 있다. 음향방출 센서의 높은 민감도는 베어링의 건전성을 추론 할 수 있는 미세한 고장 신호까지 취득이 가능하며, 이는 기존의 진동 기반의 상태

감시(condition monitoring)에서 다소 어려웠던 조기 고장 진단(early fault detection)이나 높은 강성을 가지는 베어링 시스템의 고장 진단(fault diagnosis)을 가능케 하였다. 하지만 높은 민감도로 인해 음향방출 원신호(raw signal)는 베어링 관련 신호 뿐만 아니라 노이즈를 포함한 다른 무수히 많은 정보들을 함축하고 있기에, 목적하는 베어링의 건전성(health index)을 직접적으로 규명하기 어렵다. 아울러, 음향방출 신호는 높은 샘플링 레이트(sampling rate)로 인하여 통상적으로 매우 큰 데이터 규모를 갖기 때문에, 기존의 진동 기반 신호 처리 방법들을 호환·적용하기에 현실적인 어려움이 있다. 때문에, 음향방출 센서로부터 취득된 원신호에서 목적하는 베어링의 고장 정보를 성공적으로 추출하기 위해서는 적절한 신호처리 방법이 필요하며, 이는 다른 신호에 가려져 있는 베어링 고장 신호를 찾아내는 것과, 베어링의 고장과 관련되지 않는 신호들을 제거하는 두 가지 핵심 기능을 동시에 수행하여야 한다.

따라서, 본 박사 학위 논문에서는 잡음(noise) 환경에서의 회전체 베어링 고장 진단을 위한 음향방출 신호처리 기법 개발에 초점을 맞추고자 한다. 이에 두 가지 핵심 연구를 진행하였으며 주제는 다음과 같다: 1) 베어링의 건전성을 추론하기 위한 고장 관련 주파수 밴드 선정 기법에 관한 연구, 2) 베어링의 고장과 무관한 신호의 제거를 위한 디노이징(de-noising) 기법 연구.

먼저, 첫번째 핵심 연구는 노이즈가 많은 음향방출 데이터를 대상으로 계산 비용에 효율적인 주파수 밴드 선정 알고리즘을 개발하는 것이다. 산업내 실질적인 적용성을 증진시키기 위하여 해당 연구에서는 추가적인 스펙트럼 분석(spectrum analysis) 없이, 시간 도메인의 특성치만을 이용하여 고장을 가려내는 새로운 척도(defect measure)를 제안하였다.

제안된 척도는 베어링의 고장 특성을 기반으로 분할된 신호들의 충격성(impulsiveness)과 반복성(periodicity)을 고려하여 설계되었으며, 임의의 충격 외란(random impulsive disturbance)과 비정상성을 가지는 주기적인 노이즈(non-Gaussian periodic noise)에 모두 강건성을 가짐을 보였다. 또 다른 핵심 연구는 최적 주파수밴드 선정으로도 여전히 필터링 할 수 없는 전기노이즈를, 진단 평면에서 디노이징 하는 연구이다. 본 연구에서는 여러 전기 노이즈 중에서도 높은 비정상성으로 음향방출 신호 분석에 있어서 큰 어려움으로 알려진 전자파간섭(electromagnetic interference)에 초점을 맞추었다. 복잡한 고주파 변조(complex high-frequency modulation)를 가지는 전자파간섭을 제거하기 위하여, 본 연구는 다중 센서(multi-sensor) 기반의 분석법을 수행하였고, 추가 센서로는 모터로 유입되는 전류 신호를 이용하였다. 다중 센서 기반의 디노이징을 위해 경험적 모드 분해(empirical mode decomposition) 기법과 확률 분포 기반의 동적 필터(dynamic filter) 설계를 수행하였다. 이를 통해 전류신호로부터 운행 조건에 따라 변화무쌍한 전자기간섭 노이즈를 유동적으로 선별하고, 목적하는 베어링 고장에 대한 신호적 외란 위험성을 최소화하였다. 결과적으로, 제안된 디노이징 기법은 시스템 작동 조건의 유무와 관계 없이 음향방출 신호의 포락 스펙트럼 내 전자파간섭 성분들을 효과적으로 제거함을 보였다.

주요어: 구름 요소 베어링 (rolling element bearing, REB)

고장 진단 (fault diagnostics)

음향 방출 (acoustic emission, AE)

주파수 밴드 선정 (frequency band selection)

전기 노이즈 제거 (electrical noise elimination)

학번: 2015-20718